Study of High-Ni Positive Electrode Materials for Li-ion Batteries

by

Chenxi Geng

Submitted in partial fulfillment of the requirements
for the degree of Doctor of Philosophy

at

Dalhousie University
Halifax, Nova Scotia
April 2024

To everyone and everything that is important to me,

Table of Contents

List of Tables

List of Figures

Abstract

Replacing the combustion engine by electric vehicles powered by lithium-ion batteries (LIBs) is a crucial part of the current energy revolution. The advantages of LIBs, long cycle life and high energy density, make them ideal for use in both energy storage and electric vehicles (EVs).

Applying a more electrochemically stable coating layer on the surface of positive electrode particles is one way to mitigate the degradation rate of positive electrode materials. In Chapter 3, we introduce a low-cost dry particle fusion instrument built in house. This is an instrument that applies coatings on materials by mechanical force. Suitable coating materials, applied by dry particle fusion at the laboratory scale using this instrument, are effective in improving capacity retention.

Chapter 4 reports the successful coating of Al_2O_3 on a $Ni(OH)_2$ precursor by dry particle fusion followed by heating with $LiOH \cdot H_2O$. This work suggests that coating desired materials on precursors by dry particle fusion is an attractive approach for synthesizing next generation positive electrode materials.

Tungsten has been shown to be an effective dopant to improve capacity retention in $LiNiO_2$, and the mechanisms for this effect were studies in Chapter 5. Tungsten doped $LiNiO_2$ was prepared by both dry particle fusion and coprecipitation, in both cases followed by heating with a lithium source. Tungsten was shown for the first time to exist primarily in the grain boundaries between adjacent primary particles within a secondary particle. The tungsten was incorporated in $Li_xW_yO_z$ amorphous phases which wet the surfaces of the $LiNiO_2$ grains well and act as a "glue" to improve the mechanical strength of the secondary particles, thus improving their resistance to fracture during calendaring or charge-discharge cycling. Similar studies of tantalum as a dopant were carried out in Chapter 6.

It is our hope that this work can provide some helpful information to both industry and academia on how to improve the performance of NMC and NCA materials with high nickel content.

List of Abbreviations and Symbols Used

1PF $Ni(OH)_2$ precursor coated with 1wt% Al_2O_3 by dry particle fusion

1PFL   1PF after it has been heat treated with $LiOH \cdot H_2O$

3LNOF $LiNiO_2$ + 3wt% Al_2O_3 after dry particle fusion

3LNOFH   3LNOFH after heating

ADF   Annular dark-field

ALD   Atomic layer deposition

BF   Bright field

BSE   Backscattered electron

CCEM   Canadian centre for electron microscopy

CSTR   Continuously stirred tank reactor

DMC   Dimethyl carbonate

DP   Diffraction pattern

DPFM   Dry particle fusion machine

EDS   Energy dispersive spectroscopy

EELS   Electron energy loss spectroscopy

EV   Electric vehicles

EXAFS   Extended X-ray absorption fine structure

FEC   Fluoroethylene carbonate

FT   Fourier transform

FWHM   Full width at a half maximum

HA   High-angle

IRC	Irreversible capacities
KH	Kinetic hindrance
LCO	$LiCoO_2$
LDH	Layered double hydroxide
LFP	$LiFePO_4$
LIB	Lithium-ion battery
LNO	$LiNiO_2$
MILLS	Multiple linear least squares
NCA	$LiNi_{1-x-y}Co_xAl_yO_2$
NMC	$LiNi_{1-x-y}Mn_xCo_yO_2$
NMC111	$LiNi_{1/3}Mn_{1/3}Co_{1/3}O_2$
NMC532	$LiNi_{0.5}Mn_{0.3}Co_{0.2}O_2$
NMC622	$LiNi_{0.6}Mn_{0.2}Co_{0.2}O_2$
NMC811	$LiNi_{0.8}Mn_{0.1}Co_{0.1}O_2$
NMP	N-methyl-2-pyrrolidone
PP	Pristine precursor
PPL	Pristine precursor lithiated
PSD	Particle size distribution
PVDF	Polyvinylidene difluoride
sccm	Standard cubic centimeter per minute
SE	Secondary electron
SEM	Scanning electron microscope

SOC	State of charge
STEM	Scanning transmission electron microscope
TM	Transition metal
XAFS	X-ray absorption fine structure
XANES	X-ray absorption near-edge spectroscopy
XRD	X-ray diffraction

Acknowledgements

First of all, I would like to thank Dr. Jeff Dahn for giving me the opportunity to conduct my PhD studies in his group and for his guidance and support on my PhD studies. It is a great honor for me and I learned a lot here. Jeff is so knowledgeable, and students can get very helpful suggestions from him; and he is very productive, and we are lucky to have the chance to see how he gets the group operated.

Furthermore, I would like to thank many friends and colleagues, Divya Rathore, Animesh Dutta, Dr. Ning Zhang, Ines Hamam, Dr. Nutthaphon Phattharasupakun, Dr. Nafiseh Zaker, Dylan Heino and many other colleagues for their generous help with my experiments. People here are working together, sharing knowledge with each other and helping each other with both their study and life.

I also would like to thank Dr. Kevin Plucknett and Dr. Azadeh Kermanshahi-pour for being my committee and thank them for providing many valuable suggestions.

I would like to thank my family for their unconditional love, although I quite frequently got annoyed and fought with you guys, but thanks for the care and love that you gave me and treating me like a little princess.

In the end, I would like to thank myself - you have been much maturer for the past 5 years. I think I gradually understood the fact that no one is perfect. Accept whatever others can or cannot do, and also accept whatever you can or cannot do. Everyone has their own limitations.

Chapter 1 Introduction

Fossil fuels have been the main power source to meet the energy demands in modern society for a long time. However, the climate change and the danger of fossil fuel depletion require the transition from fossil fuels to renewable energies, such as solar, wind and tidal energy. In addition, lithium-ion batteries, the dominant type of secondary batteries used in electric vehicles, greatly improve vehicle energy efficiency compared to the traditional gasoline engine helping to promote the switch to the EVs.[1,2]

Lithium transition metal oxides ($LiMO_2$) are commonly used positive electrode materials in commercialized LIBs. The metals used commonly include Nickel (Ni), Cobalt (Co), Manganese (Mn), and Aluminum (Al), etc.[1–6] Nickel normally makes up more than half of the molar percentage of the metals. Common commercialized $LiMO_2$ materials include $LiNi_{1-x-y}Mn_xCo_yO_2$ (NMC), e. g. $LiNi_{0.8}Mn_{0.1}Co_{0.1}O_2$ (NMC811), $LiNi_{0.6}Mn_{0.2}Co_{0.2}O_2$ (NMC622), $LiNi_{0.5}Mn_{0.3}Co_{0.2}O_2$ (NMC532), $LiNi_{1/3}Mn_{1/3}Co_{1/3}O_2$ (NMC111), and $LiNi_{1-x-y}Co_xAl_yO_2$ (NCA), e. g. $LiNi_{0.8}Co_{0.15}Al_{0.05}O_2$.[1,4,7] The higher the Ni content in $LiMO_2$, the higher the specific capacity it can deliver. However, higher Ni content comes with a more rapid capacity fade rate and more serious safety concerns. Noh et al. reported that the capacity retention and thermal stability became worse as the Ni content in $LiNi_xMn_yCo_zO_2$ increased shown in Figure 1.1. [7]
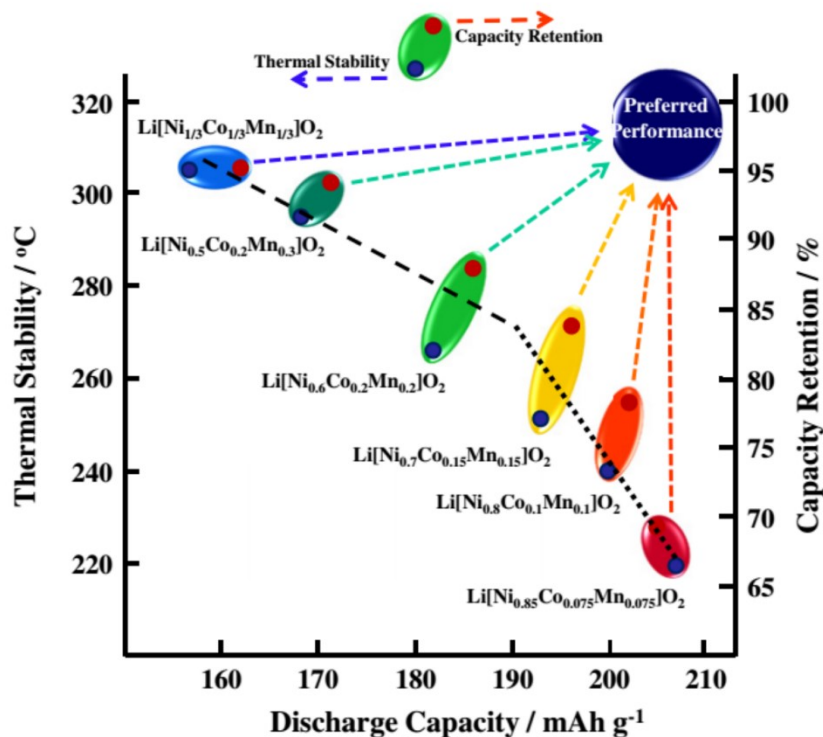
Figure 1.1 Relationship between discharge capacity, thermal stability and capacity retention of Li/Li[$Ni_xCo_yMn_z$]O_2 (x= 1/3, 0.5, 0.6, 0.7, 0.8 and 0.85). Reprinted with permission from Journal of Power Sources.[7] Copyright 2016 Elsevier.

Therefore, improving the capacity retention and thermal stability of high Ni materials is important and has gained a lot attention from researchers in both industry and academia. The addition of high valence elements like tungsten (W) and tantalum (Ta) has been reported to be particularly effective in improving the charge-discharge capacity retention of Ni-rich materials.[8–17] Although promoted by literature reports, it seemed questionable that the W and Ta atoms are located in the TM (transition metal) sites as substituents, and therefore a close examination of these materials was necessary. Before the work in this

thesis, the underlying mechanism for the action of W and Ta was unclear. The work in this thesis and that of several collaborators, now published in several refereed journal publications[15,16,18] elucidated the role of these elements. This thesis will explain the contribution of the author in understanding the role of these elements.

In addition, the parasitic reactions that occur at the interface between active material particle surfaces, primarily in the charged state, and the electrolyte is one of the degradation mechanisms for lithium metal oxides. Applying a coating on electrode particle surfaces is one method to hinder parasitic reactions. Atomic layer deposition (ALD) and wet chemistry are two approaches to apply coatings on particle surfaces.[19–21] But ALD is relatively an expensive technique with somewhat limited choices for coating materials and wet chemistry could possibly damage Ni-based positive electrode materials.[22] A new method called dry particle fusion has been developed which produces coatings of one material on particles of another by mechanical force.[23–25] This method captured our interest.

This thesis is focused on developing a new coating method, dry particle fusion, as well as understanding and improving high-Ni positive electrode materials for lithium-ion batteries. Chapter 1 gives a brief introduction on lithium-ion cells, and a review on positive electrode materials. Chapter 2 elaborates the experimental methods and theories used throughout works included in this thesis. Chapter 3 introduces a coating method, dry particle fusion, as well as a detailed demonstration of the instrument that was built in

house to apply the coatings. The operation and performance of the machine was studied. Following the introduction of the dry particle fusion method, Chapter 4 demonstrates successful dry particle fusion coatings of alumina on $Ni(OH)_2$ with great coating quality and electrochemical performance. Chapter 5 gives a detailed study on the location of tungsten in $LiNiO_2$ and proposes the mechanism of action of the tungsten element in $LiNiO_2$ positive electrode materials. Chapter 6 further studies the mechanism of action of tantalum in $LiNiO_2$ and compares the performance between the W-added and Ta-added samples in terms of Li/Ni mixing ratios, extended X-ray absorption fine structure (EXAFS), and charge-discharge cycling performance. Chapter 7 summarizes the thesis and provides suggestions for the future work.

1.1 Lithium-Ion Batteries

A lithium-ion battery is an assembly of many lithium-ion cells. Figure 1.2 shows the schematic of the working principle of a lithium-ion cell. A lithium-ion cell consists of a positive electrode (cathode), a negative electrode (anode), a separator and electrolyte in between the cathode and anode. The most common choices of cathode and anode materials are lithium transition metal oxides ($LiMO_2$) and graphite, both with layered structures. During discharge, lithium ions are extracted from the anode, transferred to the cathode surface through the electrolyte and then inserted into the cathode structure while electric current flows through the external circuit; while during the charge process, lithium ions and electrons flow in opposite direction.
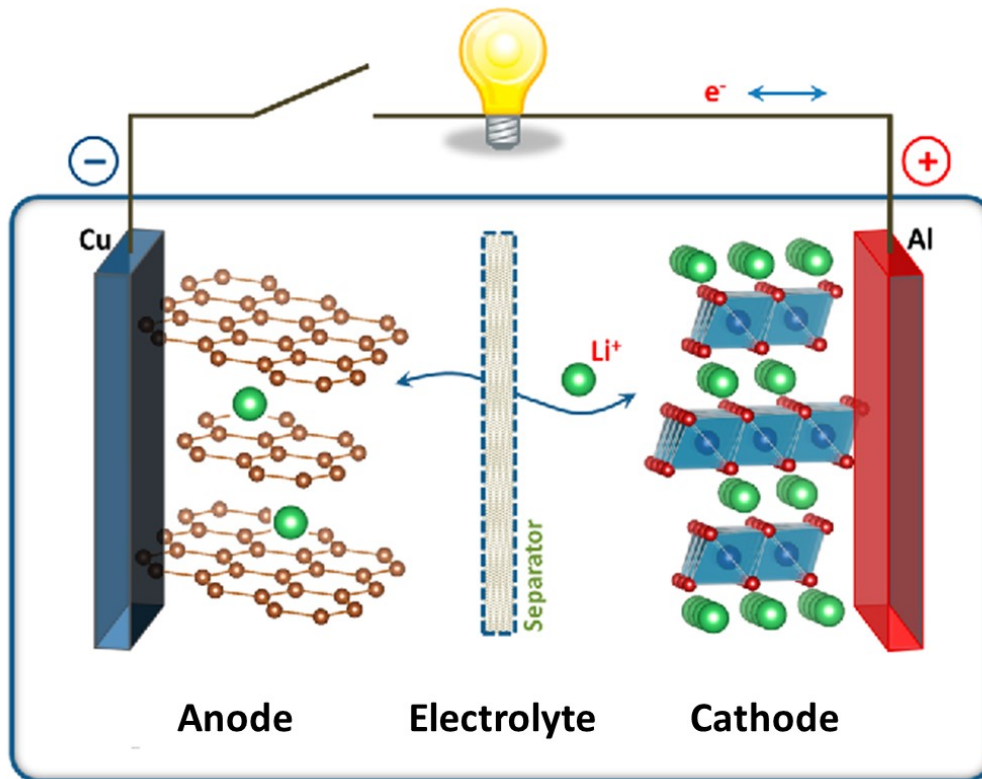
Figure 1.2 Schematic of working principle of a lithium-ion cell. Reprinted with permission from J. B. Goodenough and K. S. Park, J Am Chem Soc, **135**, 1167–1176 (2013).[26] Copyright 2013 American Chemical Society.

1.2 Positive Electrode Materials

1.2.1 LiCoO$_2$

The invention of LiCoO$_2$ (LCO) comes from the fundamental studies of electronic conductivity in 2D layers. In 1970, Jean Rouxel and Robert Schoellhorn were exploring the chemistry of Li intercalation and extraction into layered transition-metal sulfides and selenides[26]. TiS$_2$ has a 2D layered structure and Li can insert and disinsert in-between TiS$_2$ layers reversibly. Brian Steele first suggested TiS$_2$ could offer to be a cathode for

Li-ion batteries[27], and Whittingham built a TiS_2/Li rechargeable cell with a voltage of 2.2 V later in 1976[28]. However, the TiS_2/Li rechargeable cell was abandoned due to safety issues, which is a common problem when lithium metal is used directly as the anode instead of an intercalation type anode.[26,29]

A Li-O bond is stronger than a Li-S bond, so Goodenough decided to explore the reversible Li extraction from a layered $LiMO_2$ in order to increase the voltage of lithium batteries. He first reported a reversible removal of Li from $LiCoO_2$[30,31]. Gravimetric capacity defines the amount of electronic charge that can be extracted from a unit weight of electrode materials, given in mAh g^{-1}. $LiCoO_2$ has a molecular weight of 97.87 g mol^{-1}. Each mole of $LiCoO_2$ can provide 1 mole of Li^+ ions and 1 mole of electrons. The chemical equation for the extraction of Li^+ from $LiCoO_2$ is shown below:

$$Li_xCoO_2 <-> Li_{x-y}CoO_2 + y\ Li^+ + y\ e^-$$

where x can range between 0 and 1 and x-y ≥ 0.

Therefore, the theoretical capacity of $LiCoO_2$, when x and y are both 1, is:

$$Theoretical\ capacity = \frac{nF}{MW} = \frac{1mol \times 26800mAh\ mol^{-1}}{97.87\ g\ mol^{-1}} = 273.8\ mAh\ g^{-1}$$

The theoretical capacity of LCO is 273.8 mAh g^{-1} upon full delithiation. Nowadays, LCO full cells operate to 4.45 V, corresponding to a potential of about 4.53V versus Li/Li^+, and offers an initial practical specific capacity of greater than 200 mAh g^{-1}.[3,32–34]

Figure 1.3 shows the charge and discharge curves for LCO.[32]
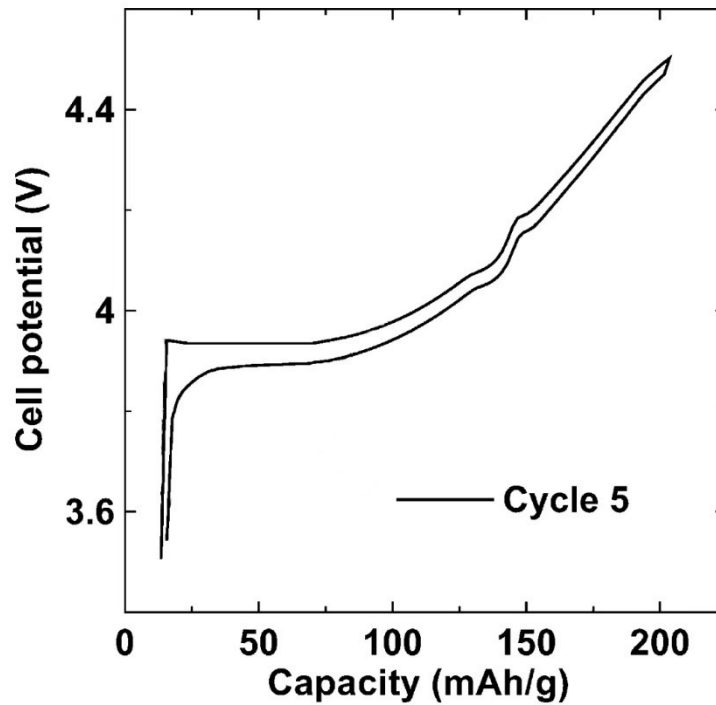
Figure 1.3 Charge–discharge curves of a Li/LiCoO$_2$ cell for cycles 5. Reproduced with

permission.[32] Copyright 2004, Elsevier.

1.2.2 LiNiO$_2$

LiNiO$_2$ (LNO) has a theoretical capacity of 274.5 mAh g^{-1}, and its initial practical

capacity is approximately 240 mAh g^{-1} cycling between 3-4.3 V at a charge/discharge

current of ~10 mA g^{-1}.[15,35,36] In addition, it is isostructural to, but cheaper than, LCO.

However, LNO has problems of rapid degradation during cycling due to its structural

instability and safety issues at high state of charge (SOC).[37,38]

Figure 1.4 shows the energy level of electronic orbitals of Ni^{2+}/Ni^{3+}, Ni^{3+}/Ni^{4+}, Co^{3+}/Co^{4+} and Mn^{3+}/Mn^{4+} couples, assuming the atoms are all in the same solid layered oxide sample. The t_{2g} level of Ni^{3+}/Ni^{4+} is higher than that of Co^{3+}/Co^{4+}, which means that the redox potential of Ni^{3+}/Ni^{4+} is lower than that of Co^{3+}/Co^{4+}. Figure 1.5 shows the charge and discharge curves for LNO. The average voltage is around 3.9 V, lower than the average voltage of 4.0 V of LCO in Figure 1.3.
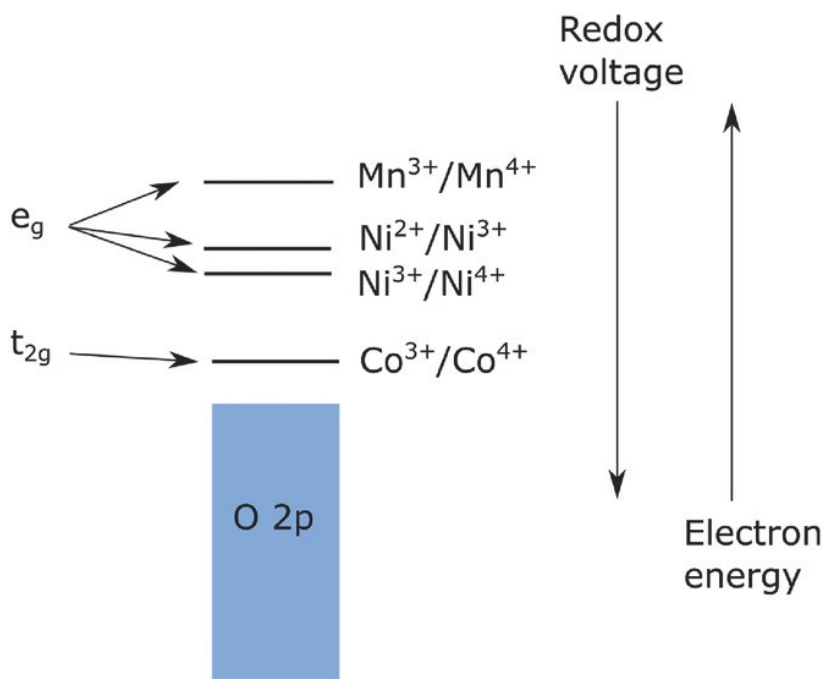
Figure 1.4 Qualitative positions of energy levels in layered Ni–Mn–Co oxide alloys. Reprinted with permission from Advanced Energy Materials.[1] Copyright (2017) John Wiley and Sons.
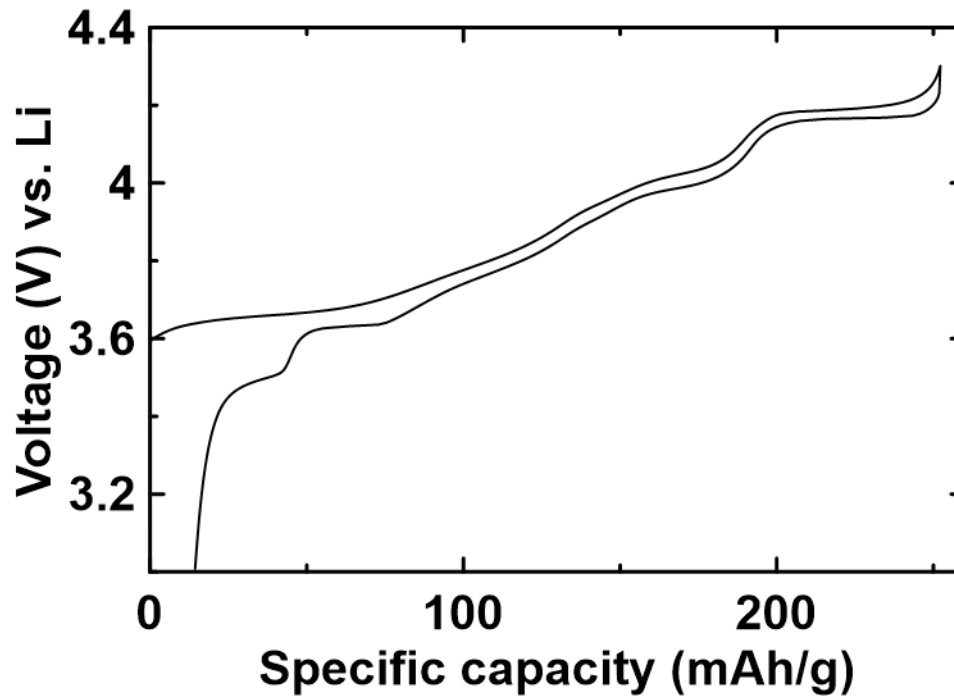
Figure 1.5 Charge and discharge profile of a Li/LiNiO$_2$ cell that was synthesized by the author at Dalhousie. The voltage vs. specific capacity curve was collected at room temperature at a current of 10 mA g^{-1}.

1.2.3 Crystal Structure of LiCoO$_2$ and LiNiO$_2$

In a crystal, atoms, or ions are arranged in a repeated way. The repeating unit is called the unit cell. A unit cell of minimum volume is called a primitive unit cell. Close packing is one of the common ways to arrange atoms or ions repeatedly in a crystal. Atoms are stacked layer by layer. Figure 1.6a shows the atom arrangement in the first layer. In a cubic close packed structure, there are three positions that atoms can occupy, marked as "A", "B", and "C". Atoms occupy "A" position in the first layer, occupy

either "B" or "C" position in the next layer and then occupy the last position in the third layer as shown in Figure 1.6b and c. Afterwards, layers of atoms stack in the same sequence as the first three layers repeatedly (ABCABCABC... or ACBACBACB...). Figure 1.6d and e show a cubic close packing of four layers viewed along the c and a axis respectively.
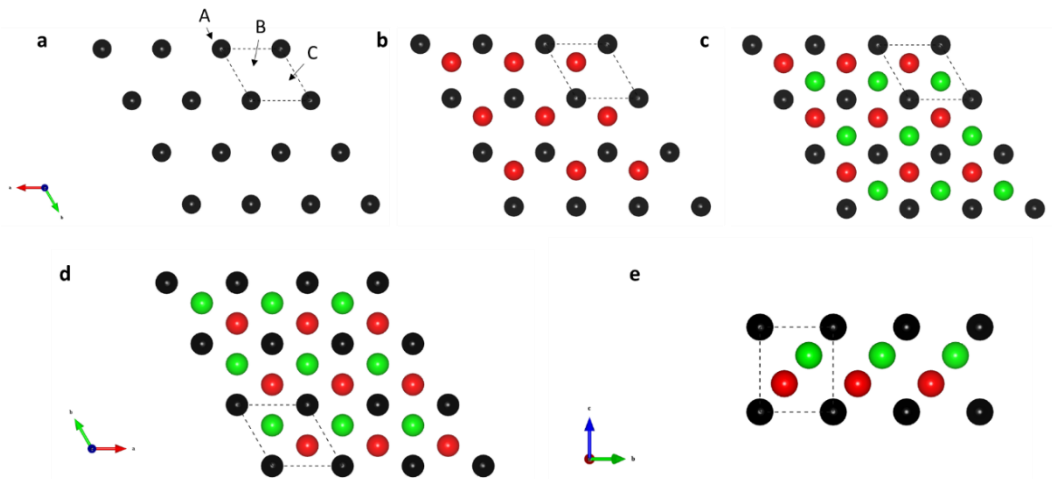
Figure 1.6 Atoms arrangement for (a) first, (b) second, and (c) third layer viewing from top of the hexagonal close packing structure along c axis; Views along (e) c axis and (f) a axis of four layers.

The structures of layered oxide materials are also based on close packed structures of atoms that are stacked at either A, B or C positions layer by layer. Figure 1.7 shows the stacking sequence of different elements in LNO and three different positions are marked as "A", "B", and "C" at the bottom of Figure 1.7a. The stacking sequence of elements is LiONiOLiONiOLiONiO, and their positions are ABCABCABCABC from bottom to top

in a unit cell. If we mark the positions of Li atoms by Greek letters, O atoms by capital letters and Ni atoms by small letters, their positions are αBcAβCaBγAbC instead. The top view of the LNO crystal structure in Figure 1.7b also clearly shows that all the atoms only occupy either A, B or C positions. Oxygen atoms are connected to Ni atoms by Ni-O bonds in Figure 1.7a, and they form an octahedron around each Ni atom connecting to its closest neighbors (6 O atoms) surrounding it. NiO_6 octahedra neighbors share edges with each other forming NiO_2 slabs, and Li atoms are inserted in between the NiO_2 slabs. If we connect Li-O bonds, we can observe that Li and O also form LiO_6 octahedra. We say that Li stays at octahedral positions between NiO_2 slabs. In addition, there are 3 layers of Li atoms for each LNO unit cell, therefore, we commonly call this structure O3 as abbreviation. The $LiNiO_2$ crystal structure belongs to the space group R-3m (No. 166), where Li sits at the 3a site (0,0,0), Ni sits at the 3b site (0, 0, 0.5) and O sits at the 3c site (0, 0, 0.24) and (0, 0, -0.24). $LiCoO_2$ has the same structure as $LiNiO_2$ with the same atom packing sequence. Therefore, LCO also belongs to O3 structure. The stacking sequence of elements is LiOCoOLiOCoOLiOCoO, and their positions are also αBcAβCaBγAbC. The $LiCoO_2$ crystal structure also belongs to the space group R-3m (No. 166), where Li sits at the 3a site (0,0,0), Co sits at the 3b site (0, 0, 0.5) and O sits at the 3c site (0, 0, 0.25) and (0, 0, -0.25).
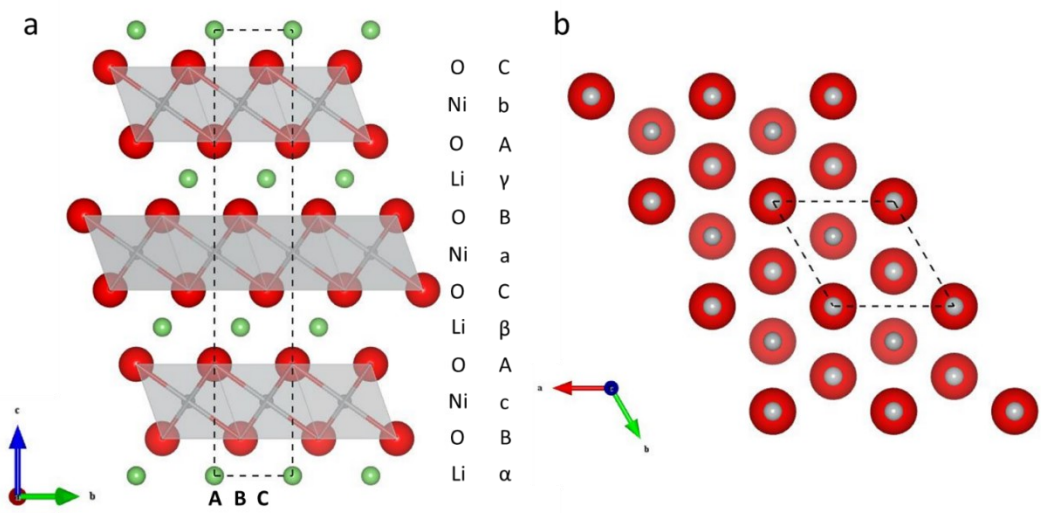
Figure 1.7 Structure of LiNiO$_2$ view along (a) a axis and (b) c axis. Three different

positions are marked as "A", "B", and "C" at the bottom of the figure. Green, red, and

gray represent Li, oxygen, and Ni atoms respectively.

1.2.4 X-ray Diffraction Pattern of LiNiO$_2$

Each crystalline material has its own X-ray diffraction pattern, like everyone has their

unique fingerprint. Figure 1.8 shows the XRD pattern of LiNiO$_2$ calculated by the

software, Rietica.[39] Each peak represents a specific plane, which is labelled in the graph.

Equation 1-1 below shows the calculation of the relative intensity of XRD peaks:

$$I = |F|^2 p\left(\frac{1 + cos^2 2\theta}{sin^2\theta cos\theta}\right)$$

Equation 1-1

Where F is structure factor, p is multiplicity factor, θ is Bragg angle, and the term

$\frac{1+cos^2 2\theta}{sin^2\theta cos\theta}$ is called the Lorentz-polarization factor. Please see chapter 2 for details of

XRD theory and relative intensity calculation theory.
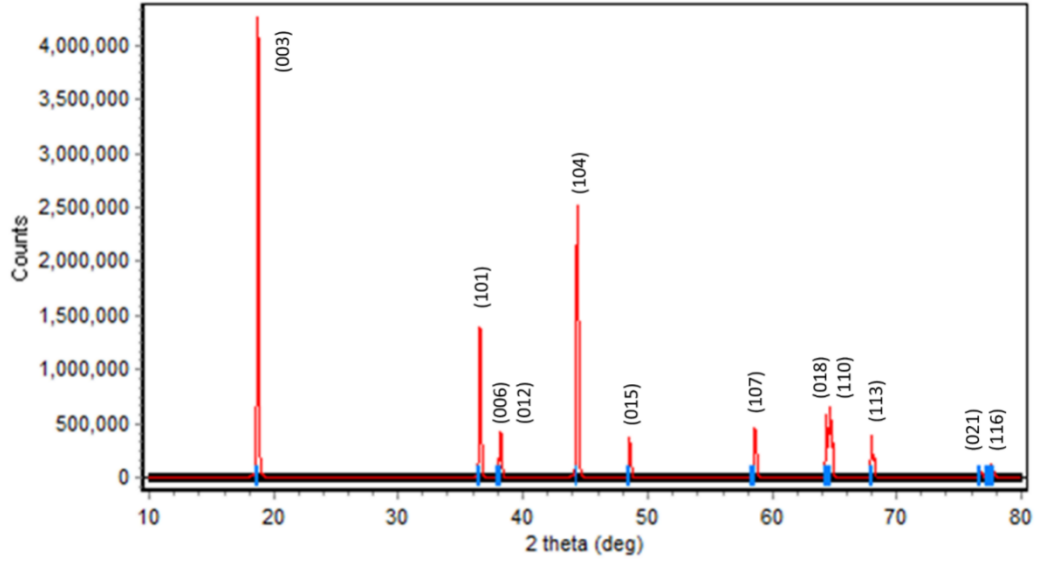
Equation 1.8 XRD pattern of LiNiO$_2$ calculated by the software, Rietica.[39]

The structure factor is shown below in Equation 1-2:

$$F_{hkl} = \sum_{1}^{N} f_n e^{2\pi i(hu_n + kv_n + lw_n)}$$

Equation 1-2

where summation extends over all atoms of the unit cell. hkl are the Miller indices for lattice planes, (u_n, k_n, w_n) are the fractional atomic coordinates of individual atom n, and f_n is the atomic scattering factor of atom n.

LNO has a space group of R-3m, where Li atoms occupy 3a sites ((0,0,0)), Ni atoms occupy 3b sites ((0,0,0.5)) and O atoms occupy 6c sites ((0,0,0.24) and (0,0,-0.24)). The calculation of the structure factor of LNO is shown below:

$$F_{hkl} = [e^{2\pi i(h\times 0 + k\times 0 + l\times 0)} + e^{2\pi i\left(h\times\left(\frac{2}{3}\right)+k\times\left(\frac{1}{3}\right)+l\times\left(\frac{1}{3}\right)\right)} + e^{2\pi i\left(h\times\left(\frac{1}{3}\right)+k\times\left(\frac{2}{3}\right)+l\times\left(\frac{2}{3}\right)\right)}] \times$$

13

$$[f_{Li}e^{2\pi i(h\times 0+k\times 0+l\times 0)} + f_{Ni}e^{2\pi i\left(h\times 0+k\times 0+l\times\left(\frac{1}{2}\right)\right)} + f_O e^{2\pi i(h\times 0+k\times 0+l\times 0.24)}$$

$$+ f_O e^{2\pi i(h\times 0+k\times 0+l\times(-0.24))}]$$

$$= [1 + e^{2\pi i\left(h\times\left(\frac{2}{3}\right)+k\times\left(\frac{1}{3}\right)+l\times\left(\frac{1}{3}\right)\right)} + e^{2\pi i\left(h\times\left(\frac{1}{3}\right)+k\times\left(\frac{2}{3}\right)+l\times\left(\frac{2}{3}\right)\right)}]$$

$$\times [f_{Li} + f_{Ni}\cos(\pi l) + 2f_O\cos(0.48\pi l)]$$

<div align="right">Equation 1-3</div>

where f_{Li}, f_{Ni} and f_O are atomic scattering factor of Li, Ni and O respectively, which change with the value of $\sin\theta/\lambda$. The value of the atomic scattering factor can be found in reference[40]. The first bracket in Equation 1-3 corresponds to a R-centered hexagonal lattice translation operation, and it is a common term in all the calculations where the space group belongs to a R-centered hexagonal lattice.

The second bracket turns out to be only real. The imaginary term in the first bracket in Equation 1-3:

$$= i \times [\sin\left(2\pi\left(\boldsymbol{h}\times\left(\frac{2}{3}\right) + \boldsymbol{k}\times\left(\frac{1}{3}\right) + \boldsymbol{l}\times\left(\frac{1}{3}\right)\right)\right)$$

$$+ \sin\left(2\pi\left(\boldsymbol{h}\times\left(\frac{1}{3}\right) + \boldsymbol{k}\times\left(\frac{2}{3}\right) + \boldsymbol{l}\times\left(\frac{2}{3}\right)\right)\right)]$$

The sum of two terms marked by **bold font** in the two sinusoidal functions equals to h+k+l:

$$h\times\left(\frac{2}{3}\right) + k\times\left(\frac{1}{3}\right) + l\times\left(\frac{1}{3}\right) + h\times\left(\frac{1}{3}\right) + k\times\left(\frac{2}{3}\right) + l\times\left(\frac{2}{3}\right) = h+k+l$$

If we make variable a $= h\times\left(\frac{2}{3}\right) + k\times\left(\frac{1}{3}\right) + l\times\left(\frac{1}{3}\right)$, and N $= h+k+l$ (h, k and l are all integers), the imaginary term further becomes,

$$= i \times [\sin(2\pi \times a) + \sin(2\pi(N - a))]$$

$$= i \times [\sin(2\pi a) + \sin(2\pi N) \cos(2\pi a) - \cos(2\pi N) \sin(2\pi a)] = 0$$

The imaginary terms cancel each other and become zero.

The real term in the first big bracket in Equation 1-3:

$$= 1 + \cos\left(2\pi\left(h \times \left(\frac{2}{3}\right) + k \times \left(\frac{1}{3}\right) + l \times \left(\frac{1}{3}\right)\right)\right)$$

$$+ \cos\left(2\pi\left(h \times \left(\frac{1}{3}\right) + k \times \left(\frac{2}{3}\right) + l \times \left(\frac{2}{3}\right)\right)\right)$$

$$= 1 + \cos(2\pi a) + \cos(2\pi(N - a))$$

$$= 1 + \cos(2\pi a) + \cos(2\pi N) \cos(2\pi a) + \sin(2\pi N) \sin(2\pi a)$$

$$= 1 + 2\cos(2\pi a)$$

Therefore, when systematic extinction happens,

$$= 1 + 2\cos(2\pi a) = 0$$

$$\cos(2\pi a) = -\frac{1}{2}$$

$$2\pi a = \frac{2}{3}\pi \pm 2n\pi \ or \ \frac{4}{3}\pi \pm 2n\pi \ (n \ is \ any \ integer)$$

$$a = h \times \left(\frac{2}{3}\right) + k \times \left(\frac{1}{3}\right) + l \times \left(\frac{1}{3}\right) = \frac{1}{3} \pm n \ or \ \frac{2}{3} \pm n \ (n \ is \ any \ integer)$$

$$2h + k + l = 1 \pm 3n \ or \ 2 \pm 3n \ (n \ is \ any \ integer)$$

Or in other words, reflections will happen, only when

$$2h + k + l \neq 1 \pm 3n \ or \ 2 \pm 3n \ (n \ is \ any \ integer)$$

$$Or, \ 2h + k + l = 3n \ (n \ is \ any \ integer)$$

Equation 1-4

The above derivation applies to all R-centered hexagonal space groups. These space groups have reflections only when $2h + k + l = 3n$ $(n\ is\ any\ integer)$. Space groups include No. 146, 148, 155, 160, 161, 166, 167.

Therefore,

$$F_{hkl} = [1 + 2\cos\left(2\pi\left(\frac{2}{3}h + \frac{1}{3}k + \frac{1}{3}l\right)\right)] \times [f_{Li} + f_{Ni}\cos(\pi l) + 2f_O\cos(0.48\pi l)]$$

$$=(1 + 2 \times 1) \times [f_{Li} + f_{Ni}\cos(\pi l) + 2f_O\cos(0.48\pi l)]$$

$$= 3[f_{Li} + f_{Ni}\cos(\pi l) + 2f_O\cos(0.48\pi l)]$$

Equation 1-5

To calculate the diffraction angle, we need to know the distance between adjacent planes in the set (hkl), and for hexagonal crystal lattice, it can be calculated using Equation 1-6 below

$$\frac{1}{d^2} = \frac{4}{3}\left(\frac{h^2 + hk + k^2}{a^2}\right) + \frac{l^2}{c^2}$$

Equation 1-6

Since we know the Miller index (hkl) of each plane, and lattice parameter a is normally around 2.88 Å, c is around 14.2 Å, we can calculate the plane spacing, d, for each set of planes (hkl).

Furthermore, Bragg's law allows us to calculate the diffraction angle,

$$\lambda = 2d * sin\theta$$

Equation 1-7

16

Where we normally use copper as X-ray source, and the wavelength of copper $K_{\alpha 1}$ is 1.5406 Å.

Table 1.1 shows a simple calculation of the relative intensities of XRD peaks of LNO by the author using a spreadsheet. The intensities were normalized so that the strongest peak (003) was set to 100. The normalized intensities of the peaks match the calculation results by software Rietica shown in Figure 1.8.

Table 1.1 Calculation of the relative intensities of XRD peaks.

hkl	θ (degree)	F_{hkl}	$|F_{hkl}|^2$	Multiplicity	Lorentz-polarization factor	$I_{calculation}$	$I_{normalized}$
003	9.4	-75.7	5730	2	72.59	831877	100
101	18.3	-54.4	2960	6	17.62	312990	37.62
006	19.0	37.5	1407	2	16.18	45539	5.47
012	19.1	35.6	1266	6	15.97	121370	14.59
104	22.2	89.3	7983	6	11.46	548707	65.96
015	24.3	-42.2	1778	6	9.34	99613	11.97
107	29.3	-55.3	3055	6	6.09	111556	13.41
018	32.2	70.2	4928	6	4.94	146175	17.57
110	32.3	72.7	5292	6	4.89	155348	18.67
113	34.0	-46.1	2127	12	4.40	112297	13.50
021	38.3	-38.6	1488	6	3.49	31186	3.75
116	38.8	31.4	984	12	3.42	40443	4.86

1.2.5 Cation Mixing in LiNiO₂

It is hard to synthesize stoichiometric $LiNiO_2$. In fact, Ni^{2+} ions tend to occupy octahedral sites in the Li layer due to the small difference in ionic radii between Li^+ (0.76

Å) and Ni^{2+} (0.69 Å). Therefore, the true formula of lithium nickel oxide is $(Li_{1-x}Ni_x)NiO_2$ ($0<x<1$), instead of $LiNiO_2$. This is called cation mixing or Li/Ni mixing in LNO.[41–44]

A fraction of x of Ni occupies sites in the Li layer. It means that the 3a site is not composed of pure Li, and $Li_{1-x}Ni_x$ occupies the 3a site instead. Accordingly, Equation 1-5 becomes:

$$|F_{hkl}|^2 = 3^2 \times (xf_{Ni}(1-x)f_{Li} + f_{Ni}\cos(\pi l) + 2f_O\cos(0.48\pi l))^2$$

<div align="right">Equation 1-8</div>

Figure 1.9 shows the calculated XRD patterns of LNO with different cation mixing fraction x from 0 to 0.2 using the software, Rietica. The intensity of the (003), (101), (015), (107) and (113) peaks decrease with increasing amount of cation mixing. The intensity of the (006), (012), (104), (018) and (110) peaks increase with increasing amount of cation mixing but only slightly compared to (003) peak. The (003) peak has the largest intensity with the most distinct decrease in peak intensity, and the (104) peak has the largest intensity among the increased peaks. Therefore, researchers often use intensity ratio of (003)/(104) to indicate the amount of cation mixing. A decreasing intensity ratio of (003)/(104) indicates a higher order of cation mixing.
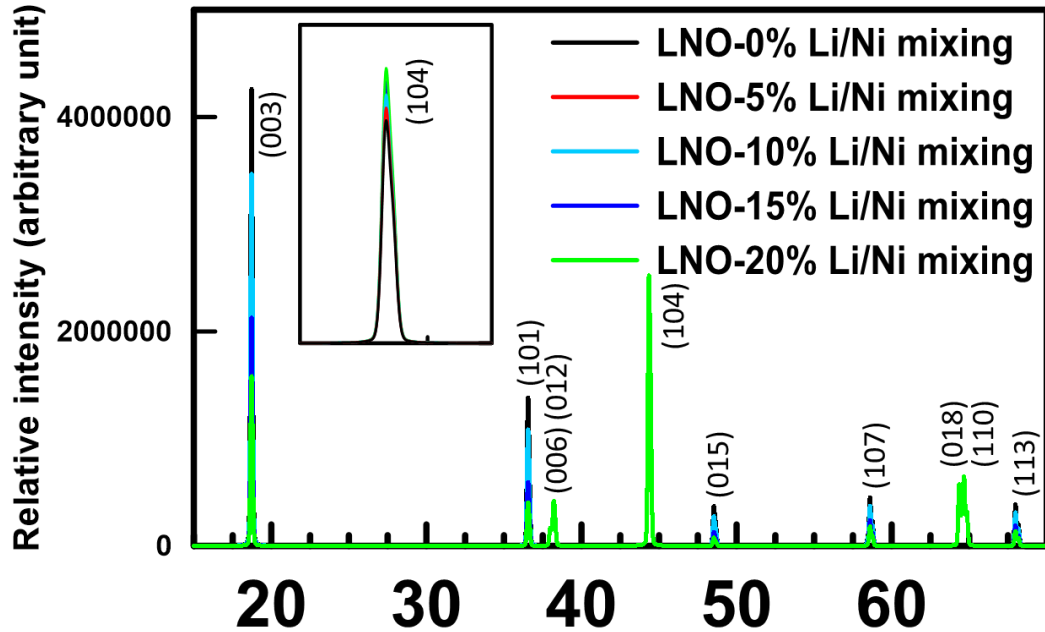
Figure 1.9 XRD patterns of LNO with different cation mixing ratios calculated by the software, Rietica.

Table 1.2 lists the atomic scattering factors for Li and Ni sites after including the cation mixing, the normalized (003) and (104) peak intensities and the (003)/(104) intensity ratios for different amount of cation mixing of LNO calculated by the author using a spreadsheet,. The (003) and (104) peaks were normalized so that the strongest peak, (003) peak with 0 cation mixing was set to 100. The normalized intensity is summarized in the rows of $I_{normalization}$ for (003) and (104) peaks, and the results match the calculation results by the software, Rietica, shown in Figure 1.9. To be more concise, the change in peak intensity comes from the change in the structure factor in Equation 1-8, F_{hkl} increases slightly with an increasing amount of cation mixing x, if l in (hkl) is an even number.

Otherwise, F_{hkl} becomes smaller with an increasing amount of cation mixing, x, if l is an odd number.

Table 1.2 Summary of the atomic scattering factors for Li and Ni sites after including the cation mixing, the normalized (003) and (104) peak intensities and the (003)/(104) intensity ratios for different amount of cation mixing.

Li/Ni mixing		0	0.05	0.1	0.15	0.2
003	$f_{Li1-xNix}$ (Li site: 3a)	2.2	3.3	4.4	5.6	6.7
	f_{Ni} (Ni site:3b)	24.8	24.8	24.8	24.8	24.8
	$I_{normalization}$	100	91.24	82.88	74.93	67.38
104	$f_{Li1-xNix}$ (Li site: 3a)	1.7	2.5	3.4	4.3	5.1
	f_{Ni} (Ni site:3b)	19.1	19.1	19.1	19.1	19.1
	$I_{normalization}$	65.96	69.88	73.91	78.05	82.31
Intensity ratio 003/104		1.516	1.306	1.121	0.960	0.819

1.3 Addition of Elements

LNO is one of the earliest types of layered transition metal cathodes. LNO gives a large specific capacity, however, LNO undergoes relatively rapid degradation and has

relatively poor capacity retention.[44–47] Doping, where the added atom substitutes for a TM atom or a Li atom in the LNO structure, is an important strategy to mitigate degradation of LNO during cycling and improve capacity retention. Common doping elements include Aluminum (Al), Magnesium (Mg), and Manganese (Mn).[1,5] $LiNi_{1-x-y}Mn_xCo_yO_2$ (NMC) and $LiNi_{1-x-y}Co_xAl_yO_2$ (NCA) derived from LNO and LCO with the aforementioned dopants, were developed in the past two decades. LCO, LNO, NMC, NCA and Ni-rich positive electrode materials all have the same O3-type structure. Popular commercial types of NMC and NCA are $LiNi_{0.5}Mn_{0.3}Co_{0.2}O_2$ (NMC532). $LiNi_{0.6}Mn_{0.2}Co_{0.2}O_2$ (NMC622), $LiNi_{0.8}Mn_{0.1}Co_{0.1}O_2$ (NMC811) and $LiNi_{0.85}Co_{0.1}Al_{0.05}O_2$. Researchers found that layered oxide materials with increasing Ni content can deliver more capacity. However, the structural stability gets worse with increasing amounts of Ni.[48–50] Nowadays, researchers have been focusing on Ni-rich positive electrode materials and aim to remove Co from layered type cathode materials due to the higher price of Co, to increase Ni content to increase the capacity of the material and to improve its structure stability during cycling.[49]

Some high valence atoms caught researchers' attention, where the addition of the atoms can clearly improve the cycling stability of the layered metal oxides, but it is not clear if the added atoms substitute for Ni atoms in the structure or are just incorporated in a second phase. The addition of tungsten (W) has been reported to be particularly effective in improving the cycling stability of Ni-rich and Li-rich materials.[11,12,51–54] Tantalum (Ta)

has also been reported to enhance the capacity retention effectively.[8,9,55] Sun et al. have studied 1 mol % of elements with different oxidation states, Ti^{4+}, Ta^{5+} and Mo^{6+}, in $LiNi_{0.91}Co_{0.09}O_2$.[56] Choi et al. showed that $LiNi_{0.885}Co_{0.100}Al_{0.015}O_2$ doped with 0.3 mol% Zr and 1.5 mol% B had full cell capacity retention of 95% after 1000 cycles between 3.0 V and 4.2 V at 1C.[57] Lv et al. showed surface modification with Si can improve the cycling retention of NMC cathode.[58]   Chapter 4 and Chapter 5 will discuss the mechanism of action of high valent elements, W and Ta, in LNO.

1.4 Coating

Improving capacity retention of the Li-ion cells during charge-discharge cycling and storage is an important goal for researchers. One of the material degradation mechanisms for layered oxide cathode materials are the parasitic reactions that occur at the interface between active material particle surfaces, primarily in the charged state, and the electrolyte. [59–61]

Applying a coating on the electrode particle surfaces is one method to hinder parasitic reactions.[1] Normally a more electrochemically stable layer is coated on the surface of the positive electrode material, which slows the rate of reactions between the positive electrode material and the electrolyte, thus improving capacity retention.[62,63] Atomic layer deposition (ALD) and wet chemistry are two approaches to apply coatings on particle surfaces. ALD can make effective thin coatings which are only a few atomic

layers thick. ALD is presently a relatively expensive technique which often requires toxic precursors. Wet chemistry involves coating particles in aqueous or non-aqueous solutions which can be expensive at the industrial scale. Using aqueous solutions could possibly damage Ni-based positive electrode materials due to ion-exchange between Li^+ from the positive electrode materials and H^+ from solution.[22] Non-aqueous solvents have been used effectively with coating materials like aluminum and niobium ethoxides.[64] However, solvent recovery systems add cost to the process so this coating method also has its drawbacks.

Dry particle fusion or mechanofusion can produce coatings of one material on particles of another by mechanical force.[23–25,65–68] Coatings can be applied with no solvents or vacuum processes required. This method captured our interest. To our best knowledge, the very early mechanofusion work dates back to 1987, when Yokoyama et al. reported an angmill mechanofusion system with a description of the mechanofusion principle.[69] Later, Alonso et al. reported a more detailed schematic diagram of a mechanofusion system and the mechanism of the mechanofusion coating process.[65] Dry particle fusion or mechanofusion has been used for many years to prepare core particles that are coated with another material.[23,24,65–70] Recently, the research group of M. Obrovac has been using mechanofusion to prepare engineered particles of advanced materials for Li-ion batteries by coating Al_2O_3 on $LiNi_{0.6}Mn_{0.2}Co_{0.2}O_2$ and embedding Si alloy particles into graphite layers.[23,24,70] These materials showed superior charge-discharge cycling

performance in all cases. The uniformity of the coating layers on the surface of the core materials and the uniformity of the Si distribution within graphite drew our attention. We designed and built a lab-scale dry particle fusion machine in our lab, which will be described in detail in Chapter 3.

Chapter 2 Experimental Techniques

2.1 Material Synthesis

2.1.1 Dry Particle Fusion

Dry particle fusion is a technique to apply coatings on spherical powders solely by mechanical force.[36] We built a lab-scale dry particle fusion instrument at Dalhousie and Chapter 3 will give a detailed description of this dry particle fusion instrument.

Most of the positive electrode materials in this thesis were made by first applying coatings (nano-Al_2O_3, nano-WO_3, nano-Ta_2O_5) on $Ni(OH)_2$ precursors followed by a lithiation step. The detailed parameters to apply coating by the dry particle fusion instrument will be stated in each chapter separately.

2.1.2 Coprecipitation

Coprecipitation is a common way to synthesize metal hydroxide precursors and W can be introduced to the material during this process.[52,71–73] Precipitation occurs when the concentration of a material exceeds its solubility. Metal hydroxides ($M(OH)_2$) like $Ni(OH)_2$, $Co(OH)_2$ and $Mn(OH)_2$ have low solubility in aqueous solution, therefore they coprecipitate in an aqueous solution containing Ni^{2+}, Co^{2+}, Mn^{2+} and OH^- ions.

Figure 2.1A shows a schematic diagram of a coprecipitation process. The solution of metal salts, most commonly sulfate or nitrate, is gradually pumped into a continuously stirred tank reactor (CSTR). Meanwhile, sodium hydroxide and ammonium hydroxide

are also slowly pumped into the CSTR, and metal hydroxides gradually and simultaneously precipitate resulting in a hydroxide precursor with uniformly-mixed metal ions. Ammonia acts as a chelating agent. The metal ions added will first coordinate to ammonia, and the metal-ammonia complex slowly releases metal ions, forming dense and spherical $M(OH)_2$ precursor.[71] The reaction mechanism is as follows:

$$M^{2+} + nNH_3 \rightarrow [M(NH_3)_n]^{2+}$$

$$[M(NH_3)_n]^{2+} + 2OH^- \rightarrow M(OH)_2 + nNH_3$$
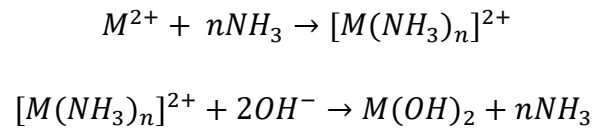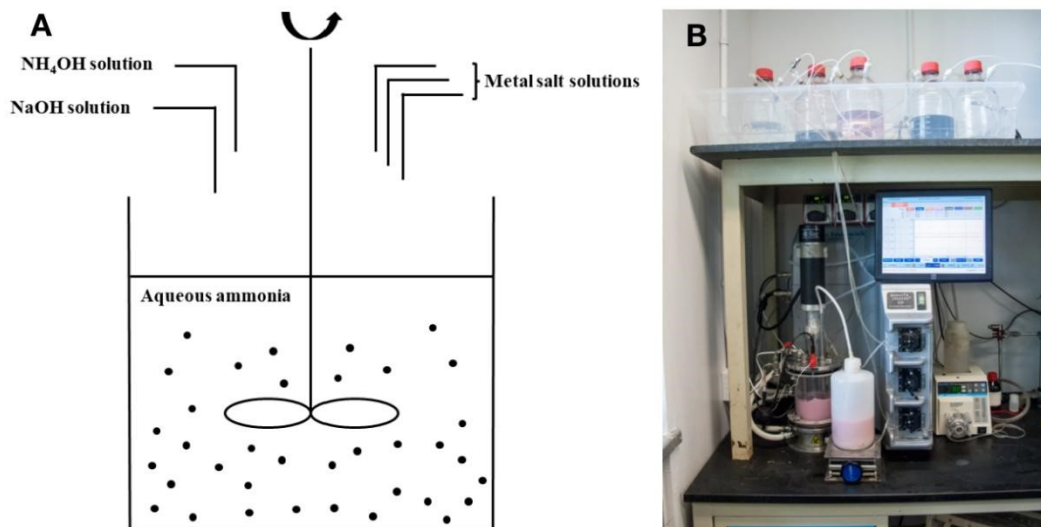
Figure 2.1 (A) Schematic drawing of the coprecipitation method; (B) Photo of an

operating CSTR co-precipitation system at Dalhousie.

In order to see if the location of W in LNO would be influenced by the way that W was added in Chapter 5, the precursor $(Ni(OH)_2)_{0.98} \cdot (NiWO_4)_{0.01}$, which has a W/(Ni+W) molar ratio of 0.01, was made by coprecipitation in a continuously stirred tank reactor (CSTR) (Brunswick Scientific/Eppendorf BioFlo 310) shown in Figure 2.1B. $NiWO_4$ has low solubility in aqueous solution, therefore, when $NaWO_4$, $NiSO_4$ and NaOH aqueous solutions are pumped into the reactor simultaneously, Ni^{2+} meet both WO_4^{2-} and OH^- ions, and $NiWO_4$ will precipitate simultaneously with $Ni(OH)_2$. 400 mL of 2.0 M $NiSO_4$ and 100 mL of 0.0808 M $NaWO_4$ were prepared separately. A 10.0 M NaOH (aq) solution was used as the source of base for the reaction, while 1 L of 1.0 M NH_3 (aq) solution was added into the tank reactor before coprecipitation for metal ion coordination with ammonia to facilitate spherical and dense particle growth during the reaction[71].

Reagents were added using digital peristaltic pumps (Masterflex L/S 07524). NaOH (aq) solution addition was automatically controlled by the pH controller and added as required by a peristaltic pump on the reactor. The vessel was maintained at a temperature of 60 °C and the contents of the reactor were stirred by an overhead stirrer at 1000 rpm. Nitrogen was bubbled at a rate of 60 sccm (standard cubic centimeter per minute) into the reactor throughout the reaction to create an inert reaction atmosphere. The reaction proceeded with the addition of 5.0 M NH_3 (aq) at 0.14 mL/min, 400 mL $NiSO_4$ at 0.333 mL/min and 100 mL $NaWO_4$ at 0.0833 mL/min (corresponding to a reaction time of 20 hours). After 20 h of reaction time, the hydroxide precursor was rinsed with 4.0 L of water, and then dried at 120 °C overnight.

The experimental conditions of the co-precipitation affect the properties of synthesized precursors. Van Bommel et al. have shown that ammonia works as a chelating agent, which increases the solubility of metal hydroxides and promotes the growth of spherical dense particles by a dissolution-recrystallization process.[71] The pH value was also shown to strongly influence the particle size and tap density of the synthesized materials. The concentrations of Ni^{2+}-NH_3 change differently with pH value, therefore, $Ni(OH)_2$ requires an optimal pH value (or an optimal pH range) to obtain the desired dense spherical particles. For Ni-rich precursors, the pH range is typically 10-11. The use of deaerated DI water and N_2 gas flow is to protect divalent metal cations from getting oxidized during coprecipitation especially when Mn^{2+} ions are pumped into the

solution.[74] Reaction time also has influence on precursor quality. Insufficient reaction time leads to small and irregular shaped particles. The reaction time was typically set to 12-24 hours.

2.1.3 Lithiation

The precursors were mixed thoroughly with a stoichiometric equivalent of $LiOH \cdot H_2O$ (purity > 99.8%, FMC Corporation) by hand milling using a mortar and a pestle. Samples with a desired lithium/transition metal molar ratio (Li/TM ratio = 1.02) were prepared. All metals other than Li are classified as transition metals in this thesis, even though Al is not a transition metal. The mass of precursor in each batch was 3.0 g. A pre-heating step at 480°C for 3 hours was performed in a tube furnace under oxygen flow. A heating rate of 10 °C/min was used to increase the temperature to the set point. After the preheating step the powder was taken out and ground to improve homogeneity. The powder was then put into a tube furnace and heated to 480°C for 2 hours for the first step and then to different temperatures (700°C, 730°C, 750°C, 800°C, 850°C, and 900°C) for different samples for another 20 hours under oxygen flow for the second step. The exact second step lithiation temperatures for different samples will be mentioned in the experimental method section in the following chapters. A heating rate of 10 °C/min was again used to increase the temperature to the various set points. The impact of 10 °C/min ramp rate should be explored in future. After the heating steps were finished, the synthesized powders were ground by hand to thoroughly break particle agglomerates.

Then they were stored in an argon-filled glovebox until required.

2.2 Material Characterization

2.2.1 X-ray Diffraction

X-ray diffraction is a method used to study the structural properties of materials. Diffraction of X-rays from solids is caused by the constructive interference of X-rays scattered elastically by electrons of atoms of the materials.[40]

2.2.1.1 XRD Data Collection
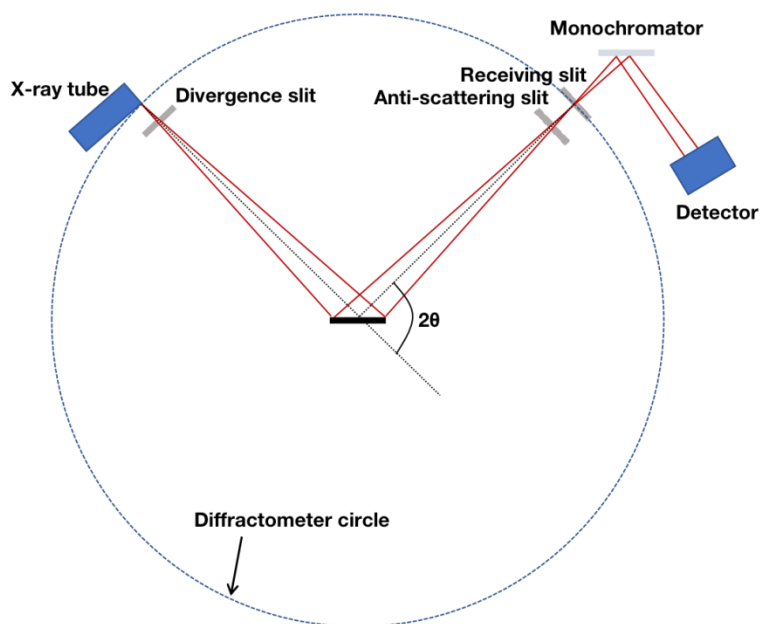
Figure 2.2 Schematic diagram of a diffractometer.

In this thesis, X-ray diffraction was carried out using a Bruker D8 diffractometer equipped with a Cu-target X-ray source and a diffracted beam monochromator. Figure 2.2 shows a schematic diagram of a diffractometer. The X-ray beams generated by the

X-ray tube first pass through the divergence slit, which removes the X-rays inclined to the plane of the diffractometer circle, and then reach the sample and get scattered. The scattered beams pass an anti-scattering slit, which screens beams scattered by air, and a receiving slit, which improves the resolution. Then the beams go through a monochromator (not shown in the figure) to filter out Cu K_β and fluorescence radiation before striking the detector. Measurements were conducted with a step size of 0.02° and a data collection time of 3-second per step. The scattering angle (2θ) range was 15 – 70°. A 1 mm divergence slit, 1 mm anti-scattering slit and 0.2 mm receiving slit were used for the measurements. Diffraction patterns were refined using "Rietica"

2.2.1.2 Unit Cell and Miller Indices

A crystal may be defined as a solid composed of atoms, ions or molecules arranged in a pattern periodic in three dimensions.[40] The periodic repeating unit is called a unit cell. Figure 2.3 shows a schematic diagram of a crystal with a repeating unit cell highlighted in bold having atoms only at the corners of the unit cell. In a real crystal system, multiple atoms normally exist within the unit cell, for example, as shown in Figure 1.7.
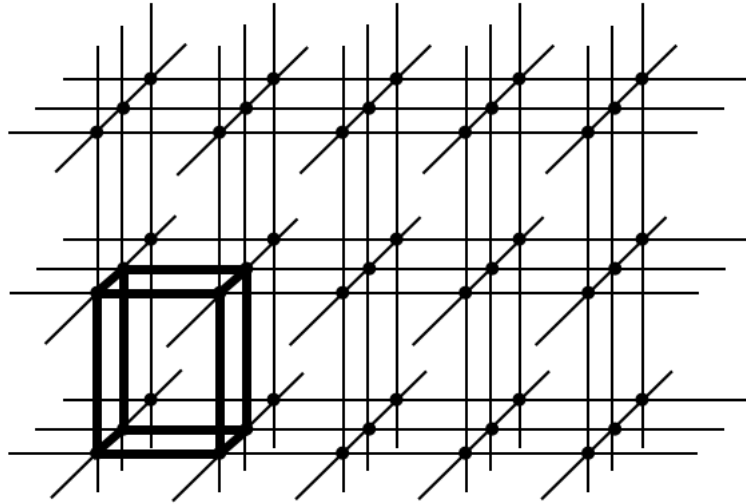
Figure 2.3 Schematic diagram of a crystal with a periodic unit cell highlighted in bold.
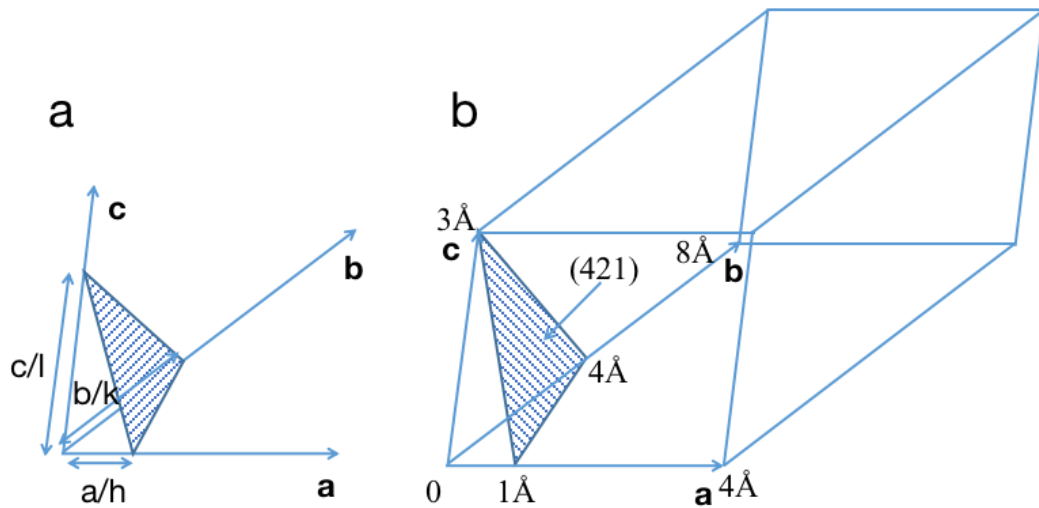
Figure 2.4 Plane designation by Miller indices.

The orientation of planes in a lattice can be represented symbolically.[40] The edges of a

unit cell are defined by vectors **a**, **b** and **c** with lengths of a, b and c as shown in Figure

2.4b, and the directions of vectors **a**, **b** and **c** are the crystallographic axes. In the general

case, the given plane will be tilted with respect to the crystallographic axes, and the plane makes intercepts of a/h, b/k, c/l with the axes as shown in Figure 2.4a, corresponding to fractional intercepts of 1/h, 1/k, 1/l respectively. We use the reciprocals of the fractional intercepts (hkl), called the Miller indices, as a symbolism to indicate the planes. Determining the Miller indices of the plane shown in Figure 2.4b is shown below.[40]

Axial lengths	4Å	8Å	3Å
Intercept lengths	1Å	4Å	3Å
Fractional intercepts	1/4	1/2	1
Miller indices	4	2	1

2.2.1.3 Bragg's Law

Figure 2.5 shows the principle of X-ray diffraction. The parallel red beams represent the incident X-ray beams, and the parallel blue beams represent the diffracted X-ray beams. When the diffracted beams from different layers are constructive, the diffracted beams reinforce each other and can be detected by a diffractometer. This requires the path difference between the two neighboring layers (AB + BC) to be equal to a whole number n of the wavelength, λ, as shown in Equation 2-1[40] below

$$n\lambda = AB + BC = d\sin\theta + d\sin\theta = 2d\sin\theta$$

$$n\lambda = 2d\sin\theta$$

Equation 2-1

Where d is the spacing between the two neighboring layers, θ is the angle between incident/scattered beam and crystal layer, and n is called the order of diffraction, for example, first-order diffraction happens when n=1 and second-order diffraction happens when n=2, etc. We can rearrange Equation 2-1, and it turns out to be convenient as we can consider all the diffraction as first-order and the spacing between the neighboring layers is 1/n of the real spacing d as described in Equation 2-2. For example, the diffraction of (006) peak for $LiNiO_2$ is a first-order diffraction between (006) neighboring planes whose spacing is ½ of the spacing between neighboring (003) planes, and it is also a second-order diffraction between (003) neighboring planes.

$$\lambda=2(d/n)\sin\theta$$

Equation 2-2
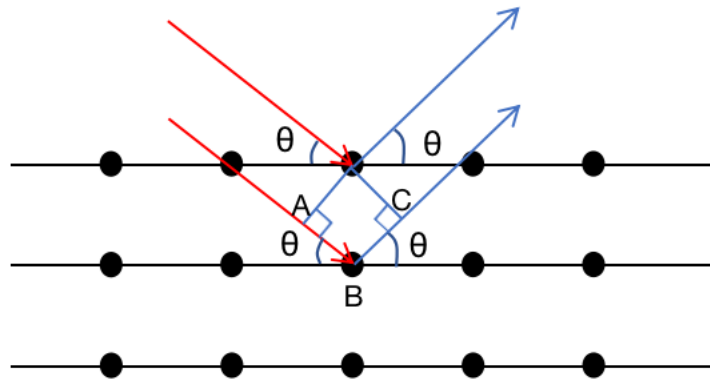
Figure 2.5 Diffraction of X-rays by a crystal

2.2.1.4 Calculation of the Intensity of XRD Peaks

2.2.1.4.1 Scattering by an Electron

The Thomson equation[40] describes the scattering of X-ray by an electron.

$$I = I_o \frac{K}{r^2} \left(\frac{1 + \cos^2 2\theta}{2}\right)$$

Equation 2-3

Where I_o is the intensity of the incident X-ray beam, K is a constant ($K=7.94\times10^{-30}$ m^2), r is the distance the scattered beam has travelled from the electron, and θ is the Bragg angle.

2.2.1.4.2 Scattering by an Atom

As shown in Figure 2.6, the amplitude of the wave scattered by an atom of atomic number Z is Z times the amplitude of the wave scattered by a single electron within the atom if the scattered wave travels in the forward direction ($\theta=0°$), as the waves traveling in the forward direction are exactly in phase with each other. However, the fact that the electrons within an atom are located differently in space introduces difference in phase of X-rays scattered by different electrons within an atom if the scattering angle 2θ is greater than $0°$. The amplitude of the wave scattered by an atom ($\theta > 0°$) is then less than Z times the amplitude of a wave scattered by an electron, and it decreases with increasing sin θ and decreasing wavelength λ.[40]

Figure 2.6 X-ray scattering by an atom.

The ratio of the amplitude of the wave scattered by an atom to the amplitude of the wave scattered by an electron is named the atomic scattering factor, f.[40]

$$f = \frac{\text{the amplitude of the wave scattered by an atom}}{\text{the amplitude of the wave scattered by an electron}}$$

Therefore, f is less than Z times the amplitude of a wave scattered by an electron when θ is greater than $0°$. In fact, f decreases with increasing $\sin \theta$ and decreasing wavelength λ and varies for different atoms. Figure 2.7 shows the value of the atomic scattering factor f for copper versus $\sin \theta/\lambda$. Readers can find the value of the atomic scattering factor for various atoms in the Appendix: Atomic Scattering Factors in reference[40].
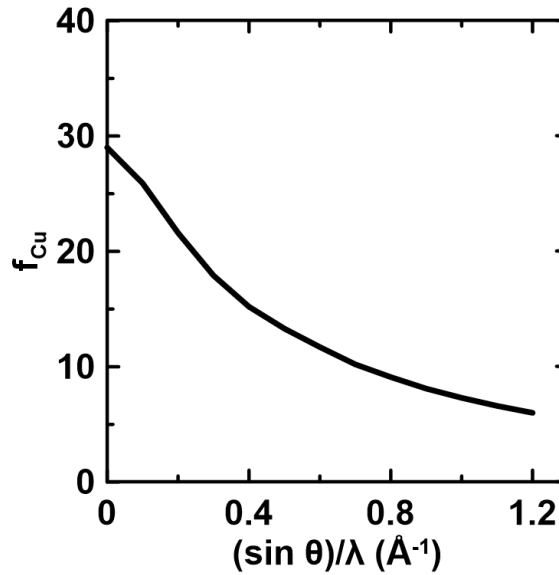
Figure 2.7 The atomic scattering factor of copper.

2.2.1.4.3 Scattering by a Unit Cell

Like the scattering by an atom, the arrangement of atoms within a unit cell can cause phase differences except in the forward direction. The phase difference caused by each atom within a unit cell is

$$\emptyset = 2\pi(hu + kv + lw)$$

Equation 2-4

where hkl are the Miller indices of the diffraction plane, and (u, v, w) are the fractional coordinates of the atom.[40]

Therefore, the scattered wave by a single atom with a fractional coordinate can be expressed in the exponential form

$$Ae^{i\emptyset} = fe^{i2\pi(hu+kv+lw)}$$

Equation 2-5

where f is the atomic scattering factor for the corresponding atom at the Bragg angle θ.

Getting the scattered waves by a unit cell requires the addition of the scattered waves by each atom within the unit cell,

$$F_{hkl} = \sum_{1}^{N} f_n e^{i2\pi(hu+kv+lw)}$$

Equation 2-6

where the summation extends over all N atoms of the unit cell.[40] The summation, F_{hkl}, is called the structure factor, and expresses both the amplitude and phase of the resultant wave. The absolute value, $|F_{hkl}|$, gives the amplitude of the resultant wave in terms of the amplitude of the wave scattered by a single electron.[40]

$$|F_{hkl}| = \frac{\text{amplitude of the wave scattered by all the atoms of a unit cell}}{\text{amplitude of the wave scattered by one electron}}$$

2.2.1.4.4 Multiplicity Factor

For a powder specimen, consider the powders have cubic structure. Some powders are oriented so that the 001 plane is parallel to the specimen surface, and 001 diffraction can occur. Some are oriented so that 010 diffraction can occur. Remember that the 001 and 010 planes have the same spacing, so the diffraction happens at the same angle. Furthermore, for a cubic lattice, the 001, 010, 100, 00$\bar{1}$, 0$\bar{1}$0, 00$\bar{1}$ planes all have the same spacing, so 6 planes contribute to the diffraction at Bragg angle for 001 diffraction. The quantity p, the multiplicity factor, is then used to describe the number of planes contributing to the same diffraction. The multiplicity factor for the same hkl varies with

different crystal systems. Values of the multiplicity factor as a function of hkl and crystal system are given in "Appendix: Data for Calculation of the Multiplicity Factor" in reference[40].

2.2.1.4.5 Lorentz-Polarization Factor

A Lorentz factor considers the impact of trigonometrical factors on the intensity of diffraction peak as described below,

$$\text{Lorentz factor} = \frac{1}{4\sin^2\theta\cos\theta}$$

<div align="right">Equation 2-7</div>

This in turn is combined with the polarization factor ($1+\cos^2 2\theta$) from Equation 2-3 derived from scattering by an electron to give the combined Lorentz-polarization factor, with a constant factor $\frac{1}{4}$ removed, and plotted as a function of θ in Figure 2.8.[40]

$$\text{Lorentz} - \text{polarization factor} = \frac{1 + \cos^2 2\theta}{\sin^2\theta\cos\theta}$$

<div align="right">Equation 2-8</div>
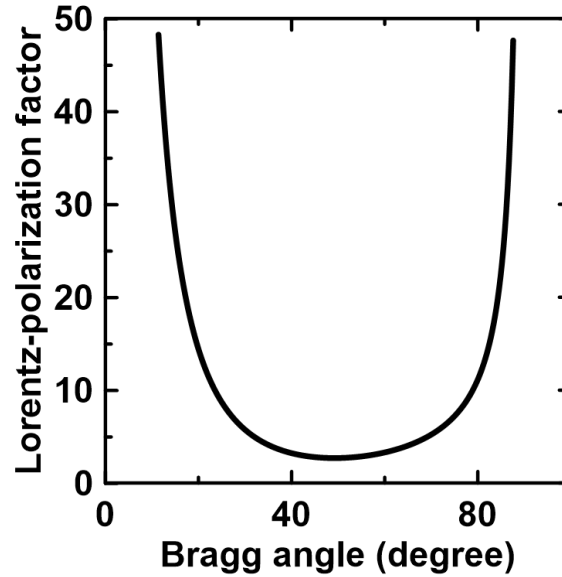
Figure 2.8 Lorentz-polarization factor.

2.2.1.4.6 Temperature Factor

So far a crystal has been considered as a collection of atoms located at fixed points in the lattice. Actually, the atoms undergo thermal vibration about their mean positions even at the absolute zero of temperature, and the amplitude of this vibration increases as the temperature increases. Thus, the reinforcement of waves scattered at the Bragg angle is not as perfect as it is for a crystal with fixed atoms. If u is the average displacement of an atom from its mean position, reinforcement becomes more imperfect as the ratio u/d increases (d is the spacing between the two neighbouring diffracting planes). Therefore, intensity drops more at higher temperature where u is larger or higher Bragg angle where d is smaller. In intensity calculations this effect is included by introducing the temperature factor e^{-2M}, which is a number by which the calculated intensity is to be multiplied to allow for thermal vibration of the atoms.

41

To summarize, all the factors discussed above add to the final intensity of X-ray diffraction peaks

$$I = p \times Lorentz - polarization\ factor \times |F_{hkl}|^2$$

$$= p(\frac{1 + \cos^2 2\theta}{\sin^2 \theta \cos \theta})|F_{hkl}|^2 e^{-2M}$$

Equation 2-9

In our work, we assume the thermal vibration of atoms for high temperature ceramic materials, i. e. Ni-based layered oxide, is negligible to cause any distinct intensity drop at room temperature, therefore, we set temperature factor e^{-2M} to 1 to remove the impact of thermal vibration on intensity. Therefore, Equation 2-10 below can be used to calculate the intensity of X-ray diffraction peaks for Ni-based layered oxide

$$I = p(\frac{1 + \cos^2 2\theta}{\sin^2 \theta \cos \theta})|F_{hkl}|^2$$

Equation 2-10

In summary, the Bragg's law described in Section 2.2.1.3 determines the angle of each peak for each plane, and the intensity of each peak can be calculated from Equation 2-10 explained in Section 2.2.1.4.

2.2.2 Scanning Electron Microscopy and Energy Dispersive X-ray Spectroscopy

A scanning electron microscope is used for obtaining the topographical information of samples at a level down to ~10 nm. A scanning electron microscope directs a sharp electron beam at the sample and collects the radiation products (secondary electrons,

backscattered electrons and X-rays) to obtain the sample topography and composition[75,76]. Figure 2.9 shows a schematic diagram of a scanning electron microscope.[75] The electrons are emitted by the electron gun, accelerated by the anode, focused by the magnetic lens, and finally hit the sample surface. The detector collects the radiation products as the focused beam scans across the sample surface directed by the scan coil. The combination of the intensity of signals with the location of signals forms an image to show the sample topography.[75,76]

When an electron beam hits the sample, both elastic scattering and inelastic scattering can occur. Scattering leads to the deviation of the electron traveling direction away from the incident direction. Some electrons go through single or multiple scattering events and the direction is deflected more than 90° and escape from the sample surface later. These electrons are called backscattered electrons (BSEs).[75,76] Some electrons deflected less than 90° after multiple scattering events lose all the kinetic energy and are absorbed in the sample later. The heavier atoms with higher atomic number can lead to stronger deflections due to a stronger columbic interaction and result in a higher backscattered electron yield, therefore, in backscattered electron mode, the brighter area indicates heavier atoms at this location and gives compositional information of the sample.
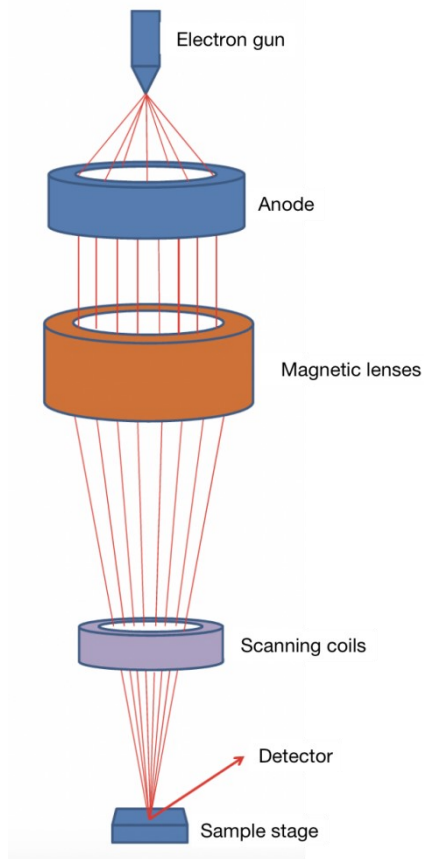
Figure 2.9 Schematic diagram of a scanning electron microscope. It composes an electron gun, anode, magnetic lenses, scanning coils, sample stage, and the electron beam directed toward the detector. Adapted from reference[75].

In addition to elastic scattering, some electrons can go through inelastic scattering in such a way that the electron strikes an electron in the atom, loses its kinetic energy, and knocks the electron out from its orbit. The electron knocked out is called a secondary electron (SE), which can have energies of less than 50 eV. Secondary electrons come mostly from the sample surface, thus can provide better surface information.[75,76]

If the secondary electrons are knocked out from an inner shell, an electron from the outer shell can fill the empty inner shell and X-rays with different specific energy from different element atoms will be generated.[76] Therefore, one can get quantitative compositional information by examining the intensities of X-rays with various energies. This technique is named energy dispersive spectroscopy (EDS).[76]

A Hitachi S-4700 SEM was used to observe the morphology and elemental distribution of the above-mentioned samples using secondary electron mode with an accelerating voltage of 15 kV and an emission current of 15 μA. Samples were mounted on carbon tape before measuring. Cross-sectioning was performed by an ion beam cross-section polisher (JEOL IB09010CP) with Ar^+ ions. Energy dispersive spectroscopy (EDS) mapping was carried out using either a JEOL JSM-7000F SEM at the Canadian Centre for Electron Microscopy (CCEM) or the same Hitachi S-4700 SEM.

2.2.3 Scanning Transmission Electron Microscopy and Electron Energy Loss Microscopy

A scanning transmission electron microscope (STEM) works similar to a scanning electron microscope (SEM). The image is obtained by collecting the electron intensity as a function of beam location as the incident electron beam focuses to a fine spot on a sufficiently thin sample and scans across the sample.[77] The incident electrons have a high kinetic energy of 100-300 keV, therefore, the incident electrons of a STEM have a shorter wavelength, down to 0.1 nm, than the electron wavelength of a SEM, leading to better resolution. A scanning transmission electron microscope collects the electrons transmitted through the sample instead of the backscattered electrons (BSEs) or secondary electrons (SEs) emitted from the surface of the sample in SEM.[77]

As shown in Figure 2.10, when an incident electron beam hits the sample, some incident electrons just transmit through the sample without encountering any electrons or nuclei and exit the sample without scattering.[77] Some incident electrons get scattered by either a nucleus or an electron. When an incident electron is scattered by a nucleus, an elastic scattering happens, where the direction of the electron deflects without losing its kinetic energy. A portion of the elastically scattered electrons are coherent and form a diffraction pattern (DP). The other scattered electrons (both elastically and inelastically scattered electrons) are incoherent. A sample image can be collected by plotting the intensity of the transmitted electrons as a function of beam location.[77] One can choose

either diffraction mode or image mode to form diffraction pattern or to form a STEM image.[77]
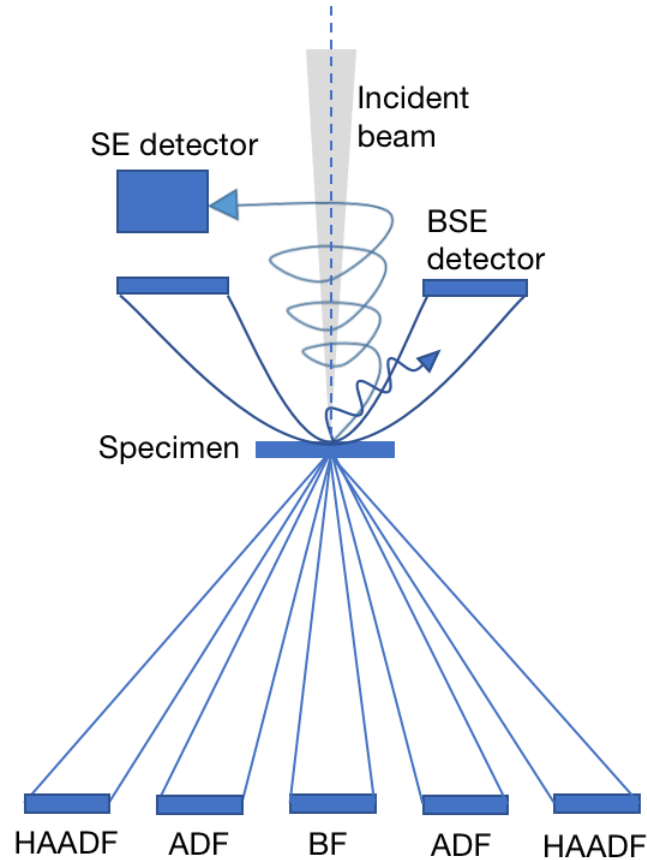
Figure 2.10 The various electron detectors in a STEM.

One of the main differences between the bright field and dark field mode is which electron populations are used to construct the STEM image. Bright field (BF) image is the most common image generated with a STEM. In the bright field image, the unscattered (transmitted) electron beam is collected by the detector, and the scattered electrons are blocked.[77] A bright field detector just below the incident beam covering a

small angle of 0-10 mrad approximately collects the unscattered (transmitted) electrons. Since the unscattered beam is collected, areas with materials will appear dark as shown in Figure 2.11A. On the other hand, in dark field mode, the unscattered electron beam is excluded from the detector, and the scattered electrons are detected instead. Hence, the areas where there is no electron scattering will be black, while the areas with materials can scatter electrons and will appear bright as shown in Figure 2.11B.[77,78] Heavier atoms scatter electrons more intensely than lighter atoms. Therefore, in bright field mode, the regions with heavier atoms are darker, while in dark field mode these regions are brighter. An annular dark field detector, which surrounds the BF detector with an angle of 10-50 mrad and then all the scattered electrons in that range fall onto that detector, can collect an STEM image. We call this process annular dark-field (ADF) imaging.[77] In addition, we can also use another annular detector that sits around the ADF and picks up the electrons scattered out to even higher angles forming so-called high-angle (HA) ADF images in which incoherently elastic scattered electrons are maximized and coherently elastic scattered electrons barely exist.[77]
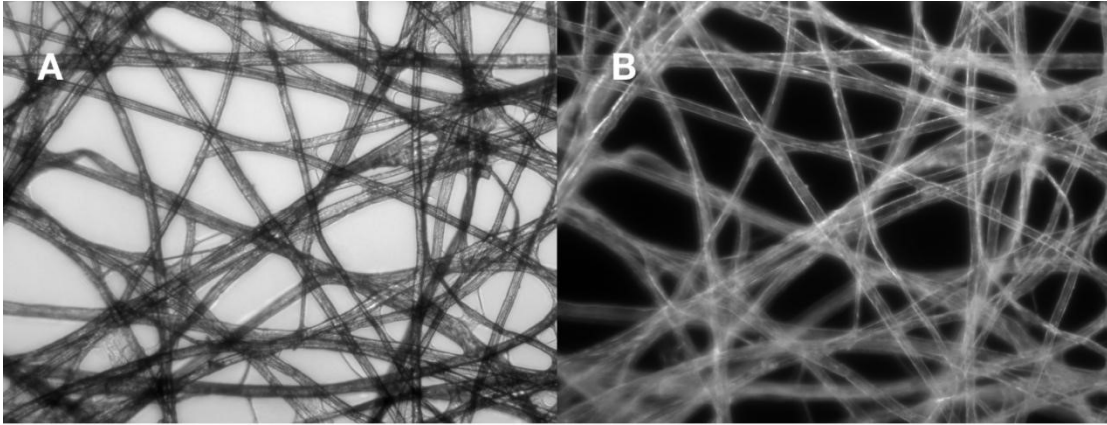
Figure 2.11 TEM image of a tissue paper sample in bright field mode (left) and dark field

mode (right).[78] Image author: Zephyris (Richard Wheeler, Wikipedia), used under

Creative Commons Attribution-Share Alike 4.0 International license.

The electron beam can lose energy during the interaction with the specimen undergoing

inelastic scattering. Similar to the generation of characteristic X-rays, the energy loss of

the incident electrons, such as due to inner shell ionization, is also a characteristic feature

for each atom. Electron energy loss spectroscopy (EELS) is the use of the change in

kinetic energy of electrons that pass through a thin sample to give structural and chemical

information. EELS instrumentation is typically incorporated into a transmission electron

microscope (TEM) or a scanning TEM (STEM).[77]

EELS Electron energy loss spectroscopy (with Gatan Quantum Imaging Filter) was used

in a scanning transmission electron microscope (STEM) (double-aberration corrected FEI

Titan 80-300) to map the distribution of elements in the samples. The STEM convergence

semi-angle as well as the EELS collection angle were 19.1 mrad, and 55 mrad, respectively. To enhance the signals while reducing beam irradiation effects, the microscope was operated at 200 keV and a direct electron detector (Gatan K2 Summit®) was used. Signals were extracted using a simple power law or multiple least-square fitting of reference spectra. Thin samples for EELS and STEM were prepared with a plasma focused ion beam (Thermofisher Helios G4 PFIB). A two-step process of thin coating of C and W was used to improve the uniformity of the thin areas. It was confirmed, from reference samples that did not contain W, that this two-step process did not generate any residue W on the lamella. The W maps are therefore representative of the W processing steps during the synthesis of the samples. All the STEM-EELS results were obtained by Nafiseh Zaker at Canadian Center for Electron Microscopy.

2.2.4 X-ray Absorption Fine Structure

When directing an X-ray beam to a sample, core-level electrons can absorb X-ray photons if the photon energy is greater than the core-level electron binding energy (such as K, L levels, etc.) so that an electron can escape from the atom as shown in Figure 2.12.[79] Therefore, one can study the chemical and physical state of the atom in a sample by observing how X-rays are absorbed by an atom at energies near and above the core-level binding energies of that atom.

The X-ray absorption fine structure (XAFS) spectrum is typically divided into two regimes: X-ray absorption near-edge spectroscopy (XANES) – typically within 30 eV of the main absorption edge and extended X-ray absorption fine-structure spectroscopy (EXAFS).[79] XANES is strongly sensitive to formal oxidation state and coordination chemistry (e.g., octahedral, tetrahedral coordination) of the absorbing atom, while the EXAFS is used to determine the distances, coordination number, and species of the neighbors of the absorbing atom. Figure 2.13 displays an example of XAFS at the platinum L3 edge for platinum foil, showing the near-edge (XANES) region and the extended fine structure (EXAFS).[80]
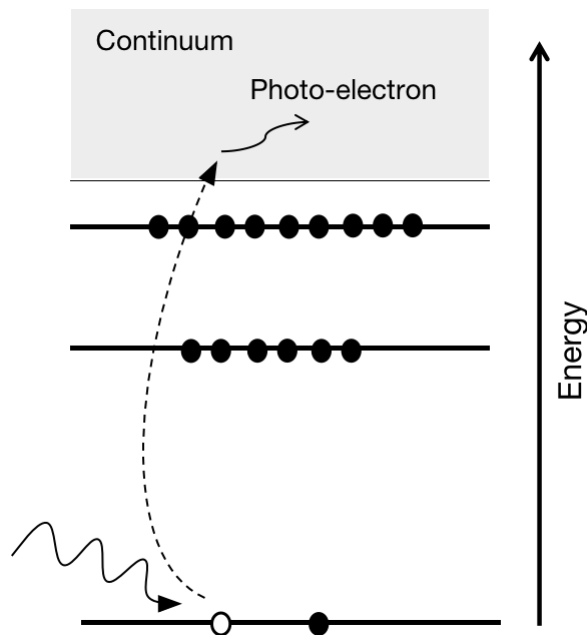
Figure 2.12 The photoelectric effect, in which an X-ray is absorbed and a core-level electron is promoted out of the atom.
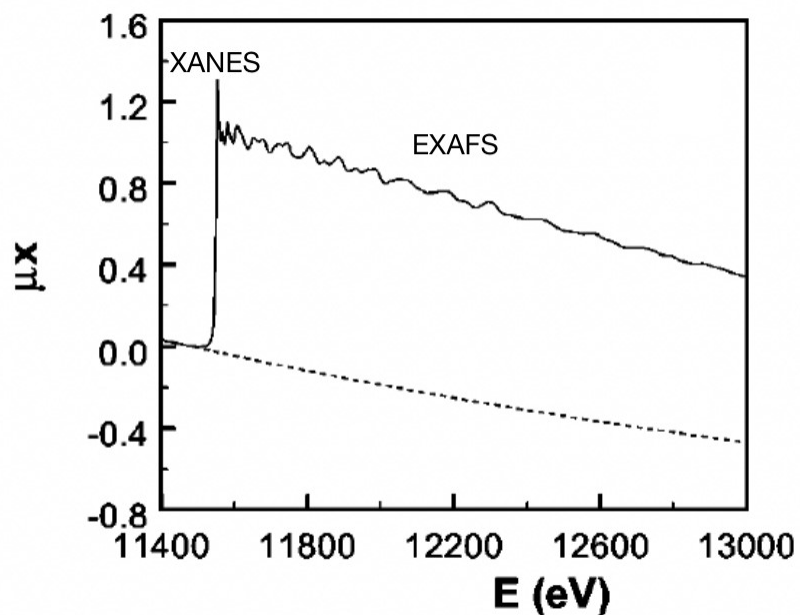
Figure 2.13 XAFS μ(E) at platinum L3 edge for platinum foil. The measured XAFS

spectrum is shown with the XANES and EXAFS regions identified. Reprinted with

permission from D. C. Koningsberger, B. L. Mojet, G. E. Van Dorssen, D. E. Ramaker,

Top Catal **2000**, *10*, 143.[80] Copyright 2000 Springer.

Figure 2.14A shows how an XAFS spectrum is carried out.   An incident beam of

monochromatic X-rays of intensity I_0 passes through a sample of thickness t, and the

transmitted beam has intensity I. The absorption coefficient μ is given by the Beer-

Lambert law[79] in Equation 2-10

$$I = I_0 e^{-\mu t}$$

Equation 2-10

Where μ is the absorption coefficient, I_0 is the X-ray intensity incident on a sample, t is

the sample thickness, and I is the intensity transmitted through the sample. As shown in Figure 2.13, the absorption coefficient versus X-ray energy is plotted in a XAFS Pt L edge spectrum.
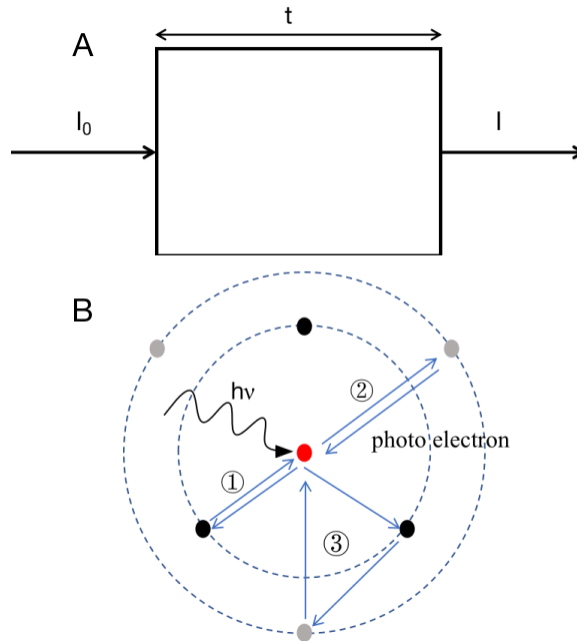
Figure 2.14 Illustration of an X-ray absorption measurement (A) and photo-electron scattering inside of the material (B).

For EXAFS, we are interested in the oscillations well above the absorption edge, and define the EXAFS fine-structure function $\chi(E)$ to describe the oscillations, as

$$\mu(E) = \mu_0(E)[1 + \chi(E)]$$

Equation 2-11

where $\mu(E)$ is the measured absorption coefficient, $\mu_0(E)$ is a smooth background function representing the absorption of an isolated atom.[79]

The oscillations come from the fact that the photo-electron escaping from the absorbing atom after absorbing a photon can be scattered back to the absorbing atom by the neighbor atoms and can further contribute to the absorption of X-ray photons.[79,80] Therefore, the EXAFS $\chi(E)$ is proportional to the amplitude of the scattered photo-electron at the absorbing atom.

We can describe the amplitude of the scattered photo-electron at the absorbing atom by a neighboring atom using the wave function of the scattered photo-electron shown in Equation 2-12[79] (the explanation of this wave function is beyond the scope of this thesis),

$$\chi(k) = \frac{f(k)}{kR^2} \sin[2kR + \delta(k)]$$

Equation 2-12

where $f(k)$ and $\delta(k)$ are the atomic scattering factor and phase shift of the atoms neighboring the absorbing atom，R is the distance to the neighboring atom. k is the wave number of the photo-electron. As we see above, EXAFS is best understood in terms of the wave behavior of the photo-electron created in the absorption process. Because of this, it is common to convert the X-ray energy to k, the wave number of the photo-electron, which has dimensions of 1/distance and is defined as

$$k = [\frac{2m(E - E_0)}{\hbar}]^{\frac{1}{2}}$$

Equation 2-13

where E_0 is the absorption edge energy, m is the electron mass and $\hbar$ is Planck's constant.[79]

Equation 2-12 only describes the amplitude of the scattered photo-electron at the

absorbing atom by one neighboring atom, however, one absorbing atom is surrounded by

a few coordination shells of atoms in a real system at approximately the same distance

from the central atom[79,80] and the number of atoms in each shell is called coordination

number. Figure 2.14B shows a simple schematic diagram of photo electron scattering

inside the material. The absorbing atom is marked in red, and the core-level electron can

escape the absorbing atom after absorbing the incident X-ray photon. Different

coordination shells are marked by blue dashed circles, and the coordination numbers are

both 3 in this diagram. As mentioned above, the photo electrons can be scattered back to

the absorbing atom by the atoms in different coordination shells, and the scattering paths

in Figure 2.14B are marked by ① and ②. Sometimes, a photo electron will be scattered

more than one time before going back to the absorbing atom (③), however, in the

derivation of the EXAFS equation multiple scattering paths are neglected as they only

contribute a few percent to the total scattering of neighboring atoms.[80] Therefore, the

measured XAFS will simply be a sum of the contributions from each coordination shell

of neighbor atoms,

$$\chi(k) = \sum_j \frac{N_j f_j(k) e^{-2k^2 \sigma_j^2}}{k R_j^2} \sin[2kR_j + \delta_j(k)]$$

Equation 2-14

where j represents the individual coordination shell of identical atoms. N_j is the

coordination number of neighbor atoms in each coordination shell j. Other variables have

been explained previously. Though somewhat complicated, the EXAFS equation allows us to fit the measured $\chi(E)$ data to get N, R, and σ^2 knowing the scattering amplitude f(k) and phase-shift $\delta(k)$.[79]

Figure 2.15 shows the process to get EXAFS $\chi(E)$ data by first removing the pre-edge background (dashed line shown in Figure 2.13), followed by removing the post-edge background marked in a dashed line in Figure 2.15a to get the isolated the EXAFS $\chi(E)$ data shown in Figure 2.15b.[80]

As explained above, the EXAFS $\chi(E)$ is the sum of amplitudes of scattered photo-electrons from different coordination shells (sinusoidal waves), therefore, one can extract the magnitude and the scattering distance R for each wave from different scattering route by applying Fourier transform (FT) to the EXAFS $\chi(E)$ data (The explanation of a Fourier transform is beyond the scope of this thesis).[79] Let's take the Ni K-edge FT-EXAFS curve for LNO in Figure 6.3 as an example. There are 4 peaks indicating 4 photo-electron sinusoidal waves scattered from 4 coordination shells contributing to the oscillation of the X-ray absorption curve and one can read the scattering distance R from the x axis. Therefore, the FT-EAXFS data is regarded as the fingerprint for materials with different structure, since different atomic arrangements result in different FT-EXAFS patterns.
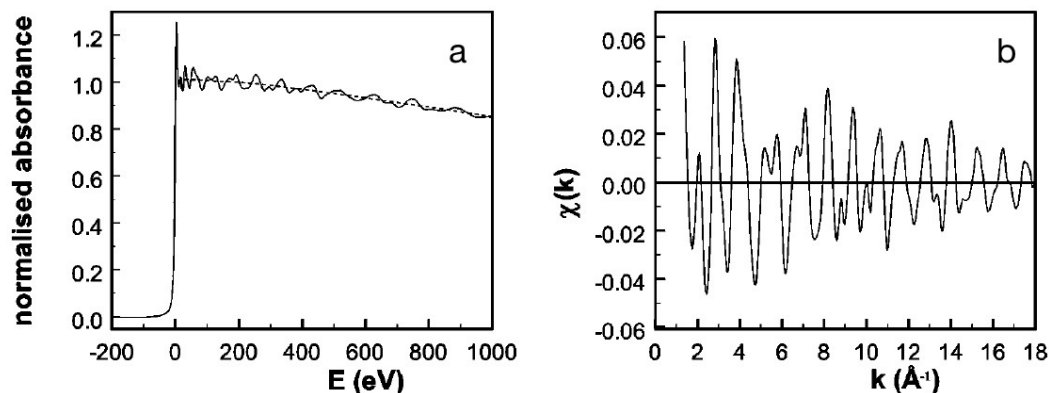
Figure 2.15 XAFS spectrum at the platinum L3 edge for platinum foil after removing the

pre-edge background (dashed line shown in Figure 2.12) (a), post-edge background

marked in a dashed line is to be removed to isolate the EXAFS $\chi(E)$ (b). Reprinted with

permission from D. C. Koningsberger, B. L. Mojet, G. E. Van Dorssen, D. E. Ramaker,

Top Catal **2000**, *10*, 143.[80] Copyright 2000 Springer.

EXAFS Extended X-ray Absorption Fine Structure Spectroscopy data was collected for

the W L3-, Ta L3- and Ni K-absorption edges on the IDEAS beamline at the Canadian

Light Source. The beamline consists of a bending magnet source with a Ge(220) double-

crystal monochromator. All data was collected in fluorescence mode, with the sample

oriented 45 degrees to the beam axis. Fluorescence data was collected using a Hitachi

Vortex ME4 silicone drift detector with FalconX electronics. All the EXAFS results

were obtained by Nafiseh Zaker at the Canadian Light Source.

2.2.5 Particle Size Distribution Analysis

Particle size distribution (PSD) analysis was carried out using laser scattering. When a beam of light is directed on a group of dispersed particles, large particles scatter light at small angles and small particles scatter light at large angles relative to the laser beam. The sizes of the particles are then calculated according to the angular scattering intensity data, using the Mie theory of light scattering.

A Partica LA-950V2 laser scattering particle size distribution analyzer (Horiba, Japan) was used to measure the particle size distribution before and after dry particle fusion. Powders were added to deionized water and sonicated for 4 minutes before particle size distribution measurements were made.

2.3 Electrochemical Measurement

2.3.1 Half Coin Cell Construction

Lithiated powders were mixed with Super-S carbon black (Timcal) and polyvinylidene difluoride (PVDF, Kynar 301F, Arkema) in a weight ratio of 92:4:4, and a suitable amount of N-methyl-2-pyrrolidone (NMP, 99.5%, Sigma-Aldrich) was added to make slurry. The slurry was coated on aluminum foil with a 150 μm notch bar with an active loading level of 10-12 mg cm^{-2} and then dried in a 120°C oven for 3 hours. The slurry was then calendared at a pressure of 2000 atm and punched into electrodes with a diameter of 12.75 mm. Electrodes were dried under vacuum for 16 hours before making coin cells. Figure 2.16 shows a schematic of a standard half coin cell. For half coin cell,

a Li foil is used as the negative electrode, and two layers of separators (Celgard #2300) are placed in between the positive electrode and the negative electrode. An electrolyte of 1.2M LiPF$_6$ (BASF, 99.9%) in FEC (BASF, 99.94%)/DMC (Shenzhen Capchem Technology Co., Ltd.) (1:4 v/v) is used. Coin cells were assembled in an argon glovebox.

Stainless Steel Cap and Gasket

Stainless Steel Spring

Stainless Steel Spacer

Lithium metal negative electrode

Celgard Separator

Celgard Separator

Positive Electrode

Aluminum Coated Can
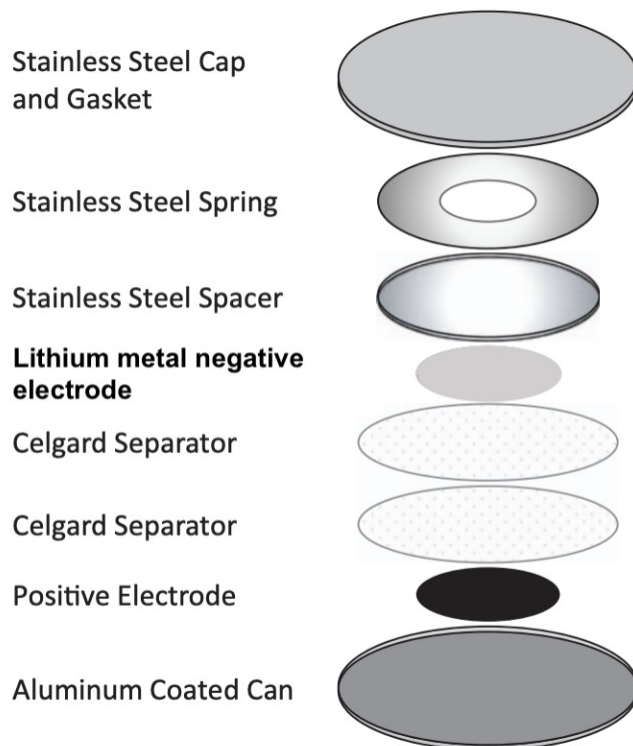
Figure 2.16 Schematic of a typical half coin cell. Adapted from reference [81].

2.3.2 Long Term Cycling Measurement

Long term charge and discharge cycling was used to analyze the synthesized materials. The charge and discharge current were determined by the electrode loading and designated specific current. Coin cells were tested using an E-one Moli Energy Canada battery test system at 30°C. Cells were cycled between 3.0–4.3 V at a specific current of

10 mA/g corresponding to ~C/20 for 2 cycles and then 40 mA/g corresponding to ~C/5

for 50 cycles and finished with a current of 10 mA/g (~C/20) for 2 cycles. Differential

capacity vs. voltage (dQ/dV vs. V) and voltage vs. specific capacity (V vs. Q) analysis

were used to study the electrochemical, structural properties and material degradation of

the positive electrode materials.

Chapter 3 Dry Particle Fusion Coating of Advanced Electrode Material Particles at the Laboratory Scale

Ni-based layered materials such as $LiNi_xCo_yAl_{1-x-y}O_2$ (NCA)，$LiNi_xMn_{1-x-y}Co_yO_2$ (NMC) and $LiNi_xM_{1-x}O_2$ (M = Al, Mn, Mg or Co) are popular positive electrode materials in commercial lithium-ion batteries. Improving capacity retention of Li-ion cells during charge-discharge cycling and storage is an important goal for researchers. One of the material degradation mechanisms is the parasitic reactions that occur at the interface between active material particle surfaces, primarily in the charged state, and the electrolyte.[59–61]

Applying a coating on electrode particle surfaces is one method to hinder parasitic reactions.[25,82–86] Normally a more electrochemically stable layer is coated on the surface of the positive electrode material, which slows the rate of reactions between the positive electrode material and the electrolyte, thus improving capacity retention. Atomic layer deposition (ALD) and wet chemistry are two approaches to apply coatings on particle surfaces.[20] ALD can make effective thin coatings which are only a few atomic layers thick. ALD is a relatively expensive technique with somewhat limited choices for coating materials. Wet chemistry involves coating particles in aqueous or non-aqueous solutions which can be expensive at the industrial scale.[21] Using aqueous solutions could possibly damage Ni-based positive electrode materials due to ion-exchange between Li^+ from the positive electrode materials and H^+ from solution[22] Non-aqueous

solvents have been used effectively with coating materials like aluminum and niobium ethoxides.[64] However, solvent recovery systems add cost to the process so this coating method also has drawbacks.

A new method called dry particle fusion has been developed which produces coatings of one material on particles of another by mechanical force with no solvents or vacuum processes required.[23–25] The dry particle fusion method has been reported to improve the conductivity and capacity retention of cathode materials by applying a coating with better conductivity like graphite[87] or a more electrochemically stable coating like Al_2O_3,[23] Cao et al. showed silicon alloy–graphite composites, in which silicon alloy particles were well dispersed and embedded between graphite layers, results in superior cyclability and rate capability.[70] This method captured our interest. We learned that machines for dry particle fusion coating are available from industrial suppliers, but these machines generally are not suitable for coating lab-scale samples of 10's of grams. Therefore, in this chapter, we designed and built a lab-scale dry particle fusion machine for a total material cost of $6,700 CAD. The principle of this technique, the design and construction of this machine and results of dry particle fusion coating are reported in this chapter.

This chapter is based on an article published in Journal of The Electrochemical Society.[36] [Chenxi Geng et al 2020 J. Electrochem. Soc. 167 110509]. Chenxi Geng contributed to the conceptualization, material synthesis, material characterizations, and electrochemical tests; Simon Trussler built the dry particle fusion instrument; Michel B. Johnson contributed to the testing and maintenance of the dry particle fusion instrument; Nafiseh Zaker, B. Scott, and Gianluigi Botton contributed to the material characterizations. Jeff Dahn contributed to the design of the machine, the design of experiments, the interpretation of results as well as editing the manuscript.

3.1 Description of the Dry Particle Fusion Instrument

Figure 3.1 shows a schematic view of the dry-particle fusion instrument. The heart of the instrument is the rotating bowl and the fixed hammer and scraper. The powder to be coated and the coating material are placed in the bowl. As the bowl rotates, the hammer compresses the powders between itself and the bowl wall, and the scraper then removes the material from the bowl wall for the next pass under the hammer. This process is illustrated in Figure 3.2e. Our instrument is designed with an approximately 10 cm diameter hardened steel bowl as well as a hardened steel hammer and scraper. The 2-horsepower motor provides plenty of torque to allow dry particle fusion to occur. The bowl angular velocity is fully adjustable between zero and 7200 revolutions per minute.
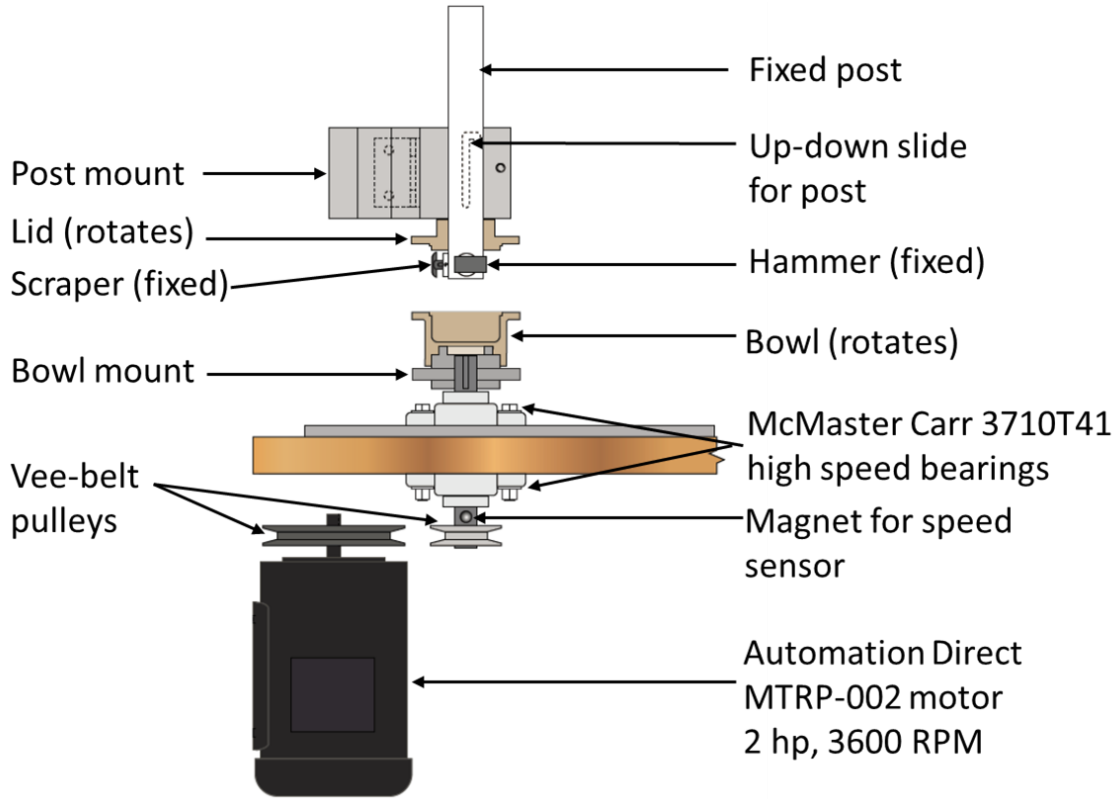
Figure 3.1 Schematic diagram of the dry particle fusion instrument constructed in this chapter. The major components of the instrument are labelled and part numbers are given where applicable.

A thermocouple fed down through the post is embedded within the hammer. Monitoring the hammer temperature versus time allows one to monitor the dry particle fusion process. The gap between the hammer surface and the bowl is adjustable and is normally set to be about 1 mm. If the gap is too large, the hammer temperature remains near room temperature and little dry particle fusion occurs. If the hammer is located properly, the temperature increases to *ca.* 70°C during a typical run.

Figures 3.2a and c show photos of the dry particle fusion instrument and a closeup photograph of the readout displays, respectively. Figure 3.2a shows the instrument with the safety shield closed and Figure 3.2b shows it with the shield opened. The desired angular velocity can be set by the motor control while a programmable timer allows operation for a set time, after which the motor stops. Figure 3.2b shows the bowl, scraper and hammer with the post raised. Figure 3.2d shows a detailed view of the scraper and hammer inside the bowl with the post lowered and the lid raised (for image clarity, the knife and hammer are set back from their operating position). Figure 3.2e shows how the dry particle fusion method applies a coating layer on the surfaces of the larger particles.

The core and coating materials are loaded inside the bowl at the same time. Normally the core particles are much larger compared to the particles of the material to be coated. The bowl spins and centrifugal force moves all the particles to the wall of the bowl. Then the hammer compresses particles between itself and the wall of the bowl causing the coating process to proceed. After passing by the hammer, the scraper removes the particles from the wall. This process repeats thousands of times per minute and particles rubbed against each other over and over again. In the end, the coating material forms a layer on the surface of core particles.[23–25]
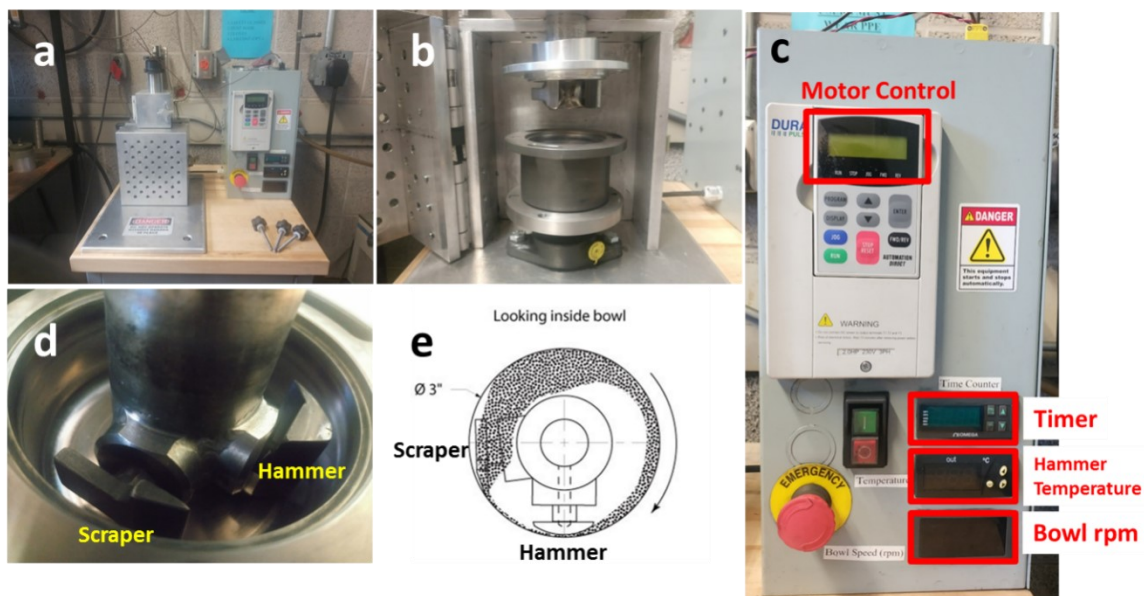
Figure 3.2. Dry-particle fusion machine (DPFM) built at Dalhousie University (a);

DPFM controller and readouts (c); The mechanical action parts: the hammer and scraper

outside (b) and inside (d) the bowl; And the principle of dry particle fusion (e).

3.2 Experimental Methods

Ni(OH)$_2$ (provided by Zoomwe, China) and commercial LiNi$_{0.8}$Co$_{0.15}$Al$_{0.05}$O$_2$ (NCA, from Umicore and Ecopro, Korea) were used as core materials for dry particle fusion. Nano-Al$_2$O$_3$ (< 50 nm, from Sigma-Aldrich) and LiFePO$_4$ (LFP, from Pulead, China), were used as coating materials in this chapter. Reagents used for coin cells included Super-S carbon black (Timcal) and polyvinylidene difluoride (PVDF, Kynar 301F, Arkema), N-methyl-2-pyrrolidone (NMP, Sigma-Aldrich, 99.5%), lithium

hexafluorophosphate (LiPF$_6$, BASF, 99.9%), fluoroethylene carbonate (FEC, BASF, 99.94%) and dimethyl carbonate (DMC, Shenzhen Capchem Technology Co., Ltd.).

Nine groups of dry particle fusion samples were made in this chapter, which are shown in Table 3.1. The hammer temperature was recorded manually during the dry particle fusion process. The gap between the hammer and the bowl was set to about 1.0 mm (0.040" with a feeler gauge).

Table 3.1 Summary of samples made by dry particle fusion in this chapter and the conditions used for each experiment.

		Core material weight (g)	Guest material weight (g)	Spinning speed (rpm)	Duration (min)
1	NCA	N/A	N/A	none	none
2	Ni(OH)$_2$	50	0	2400	60
3	NCA	44	0	4800	15
4	Ni(OH)$_2$ + 2wt% Al$_2$O$_3$	50	1.0	2400	60
5	NCA	50	0	3600	60
6	NCA + 1wt% Al$_2$O$_3$	50	0.5	3600	60
7	NCA + 2wt% Al$_2$O$_3$	50	1.0	3600	60
8	NCA + 4wt% LFP	50	2.0	3600	60
9	NCA + 10wt% LFP	50	5.0	3600	60

The lithiation process was carried out as described in Chapter 2. The second step lithiation temperature for lithiated Ni(OH)$_2$ + 2wt% Al$_2$O$_3$ in this chapter was 700°C.

SEM, EDS, PSD, XRD, Mössbauer Spectroscopy, lithiation process and coin cell long-term cycling were performed as described in Chapter 2. Electrolyte with 1.2 M $LiPF_6$ in FEC:DMC (1:4 v/v) was used for the half coin cell long-term cycling tests as this electrolyte gives better long-term lithium metal cycling.

3.3 Results and Discussion

One concern about the dry particle fusion technique is the possibility of accumulating iron impurities in the samples. Mössbauer spectroscopy was used to examine this possibility. Three samples were studied: Sample 1) fresh NCA from Ecopro; Sample 3) a 44 g sample of NCA from Ecopro was subjected to dry particle fusion for 15 minutes at 4800 rpm; and Sample 1 mixed with 1 wt% iron powder. Figure 3.3 shows the Mössbauer spectra of the three samples and it is very important that the reader notice the differences in y-axis scales between Figure 3.3c and the other two panels. Figure 3.3a for the as-received NCA shows no evidence of any absorption due to iron. Figure 3.3b shows no evidence for iron in the sample subjected to dry particle fusion. Figure 3.3c shows that 1 wt.% iron creates a strong sextet absorption, as expected for iron.[88] Comparing the results in Figure 3.3b and Figure 3.3c, one can conclude that even 0.01wt% of Fe (which would give "peaks" in Figure 3.3b of magnitude 0.005) in the sample after dry particle fusion would be easily detectable. Therefore, one can conclude that the sample after dry particle fusion has less than 0.01 wt.% iron.
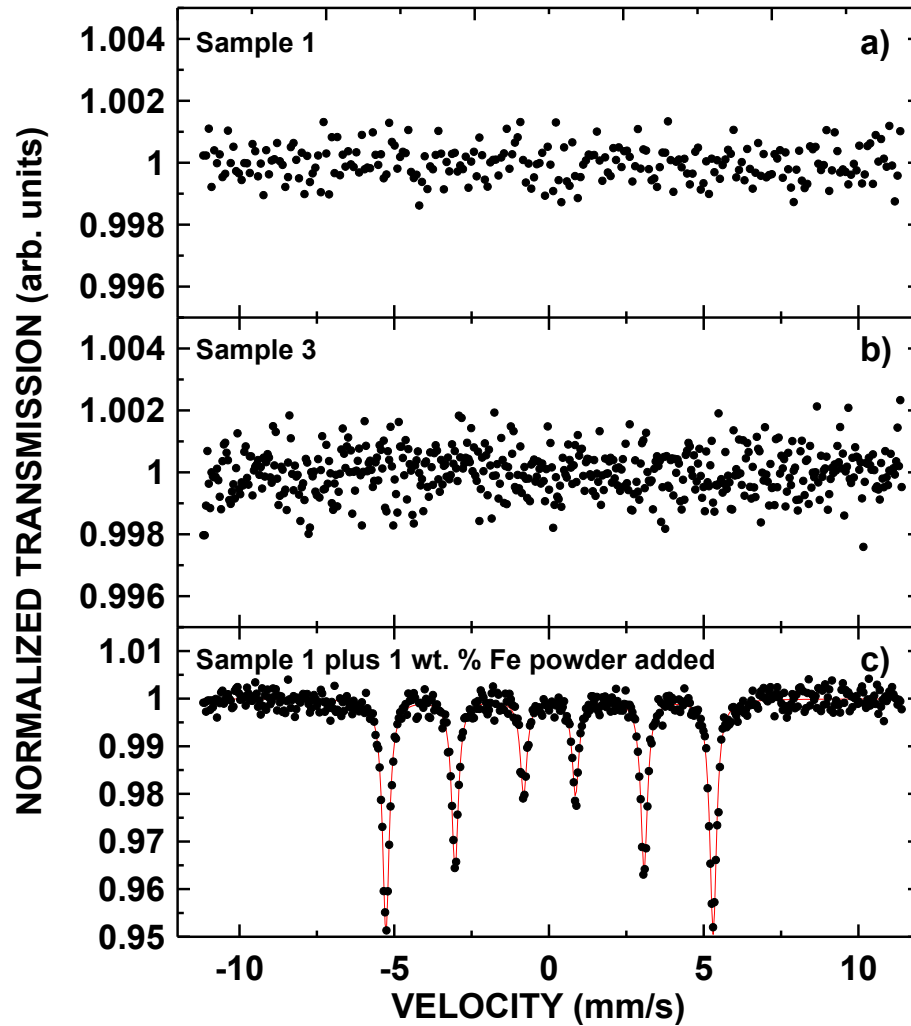
Figure 3.3. Mössbauer spectra of a) Sample 1 (Fresh NCA); b) sample 3 (NCA subjected to dry particle fusion) and c) Sample 1 with 1 wt. % Fe powder added. The y-axis scales of Figure 3.3c is different from the other two panels.

Figure 3.4a shows the hammer temperature versus time during the dry particle fusion of two samples, pure $Ni(OH)_2$ (Sample 2) and $Ni(OH)_2$ with 2wt% Al_2O_3 (Sample 4) at 2400rpm for 60 minutes. Figure 3.4a shows that the hammer temperature stabilized after 40 minutes at a similar temperature for both runs demonstrating the reproducibility of the

process.   Figure 3.4b shows the particle size distribution (PSD) results for fresh $Ni(OH)_2$ as well as $Ni(OH)_2$ (Sample 2) after dry particle fusion and $Ni(OH)_2$ with 2wt% Al_2O_3 (Sample 4) after dry particle fusion.   The particle size distribution before and after dry particle fusion did not change significantly indicating that the process did not break the core particles under the condition of 2400 rpm for 60 minutes.   Figures 3.4c, d and e show SEM images of the fresh $Ni(OH)_2$ at increasing magnifications, respectively. Figure 3.4f, 4g and 4h are images of $Ni(OH)_2$ with 2wt%Al_2O_3 after dry particle fusion (Sample 4) at increasing magnification.   Figure 3.4 shows that particles remained intact after dry particle fusion and the particle surfaces became smoother after the formation of a layer of Al_2O_3.
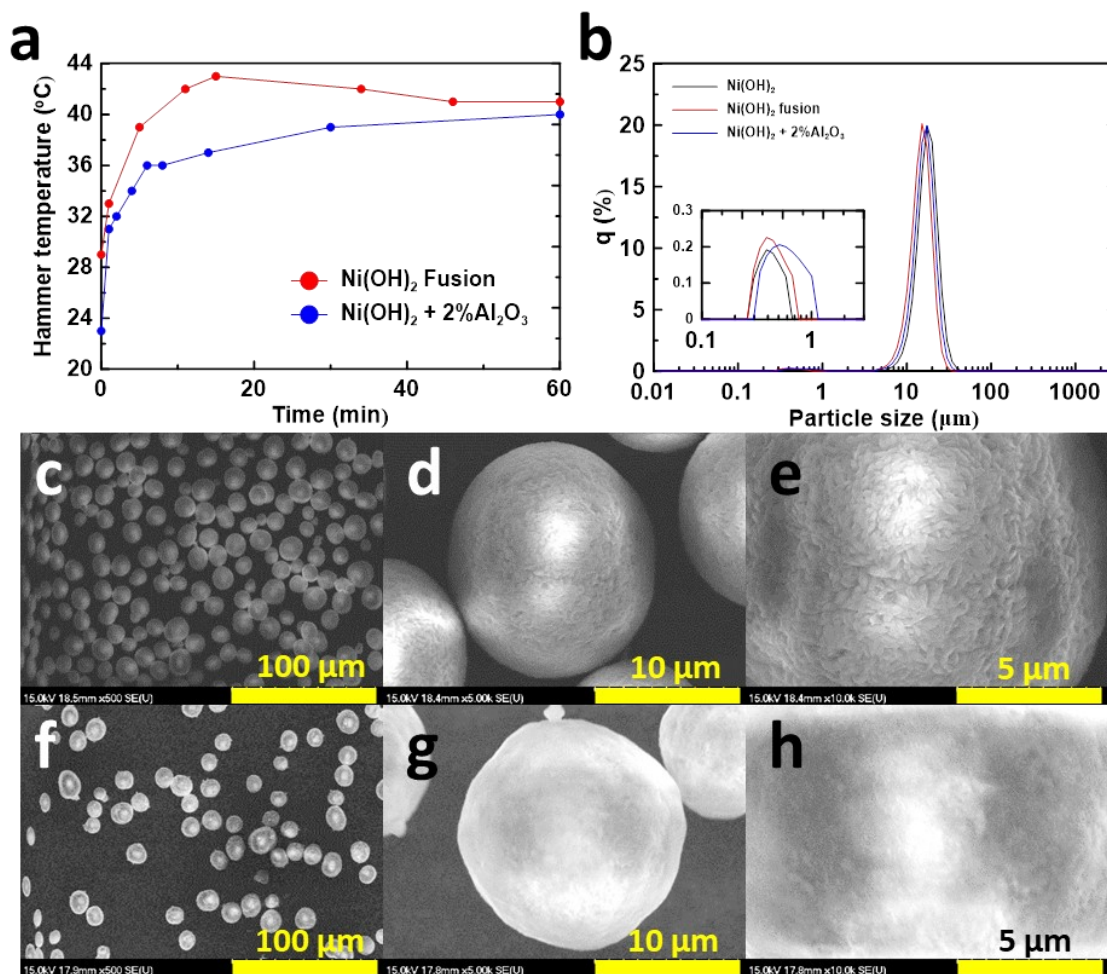
Figure 3.4. Temperature vs. time during dry particle fusion (a) and PSD results (b) of

pure Ni(OH)$_2$ (Sample 2) and Ni(OH)$_2$ with 2wt% Al$_2$O$_3$ (Sample 4) (a); SEM images of

fresh Ni(OH)$_2$ (c, d, e) and Ni(OH)$_2$ with 2wt%Al$_2$O$_3$ (Sample 4) (f, g, h).

Figure 3.5a shows the hammer temperature versus time during dry particle fusion of

samples pure NCA (Sample 5), NCA with 1wt% Al$_2$O$_3$ (Sample 6), NCA with 2wt%

Al$_2$O$_3$ (Sample 7) and NCA with 4wt% LFP (Sample 8). Temperatures stabilized after

around 40 minutes, which again shows the repeatability of dry particle fusion with NCA as the core material. Figure 3.5b shows the particle size distribution results of pure NCA before and after dry particle fusion (Sample 5). There was almost no change showing that NCA was robust enough to go through the process without breaking under conditions of 3600 rpm for 60 minutes. Figures 3.5c, d and e show SEM images of fresh NCA at several magnifications. High magnification images show that the fresh NCA particles had well defined primary particles. Figures 3.5f, g and h are images of pure NCA after dry particle fusion.   Figure 3.5 clearly shows that the surface of NCA particles become very smooth after dry particle fusion in agreement with our $Ni(OH)_2$ work and with reported literature.[24]
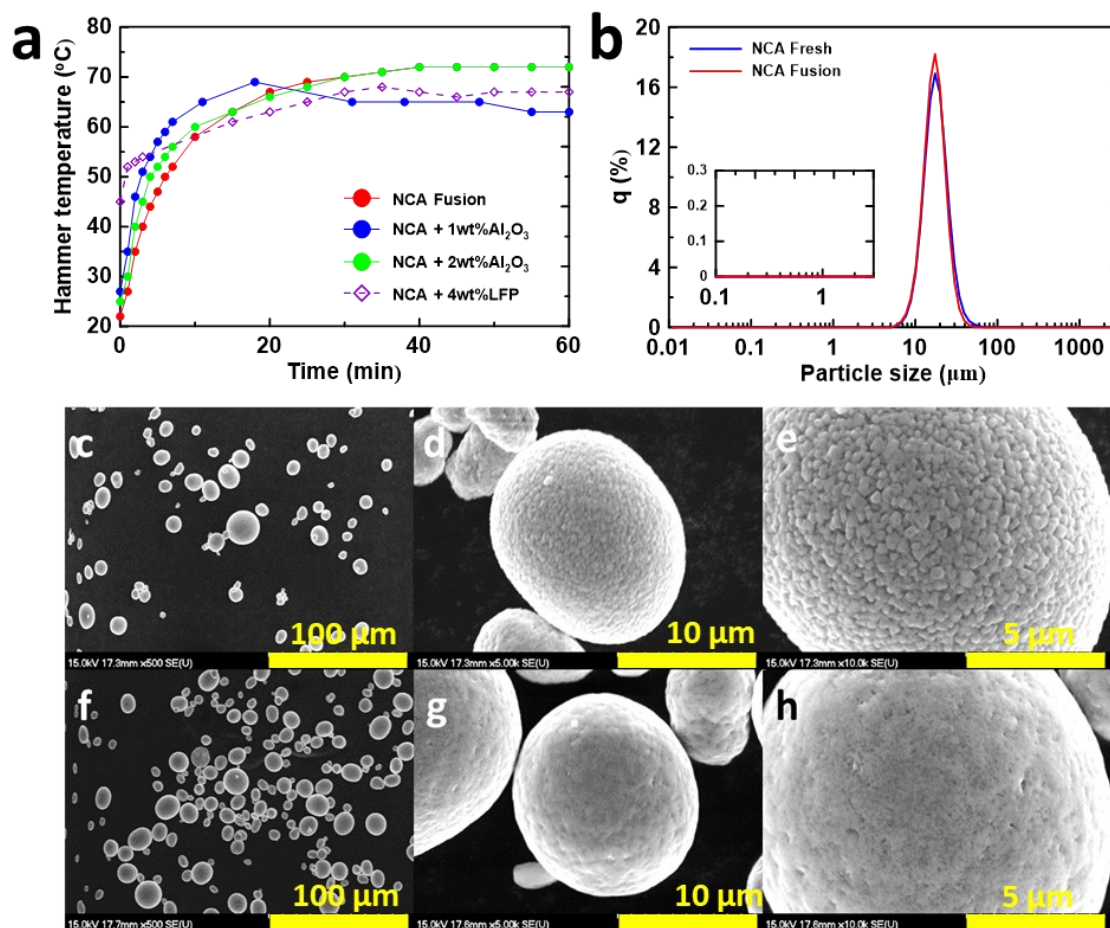
Figure 3.5. Hammer temperature vs. time during dry particle fusion of pure NCA (sample

5), NCA with 1wt%Al$_2$O$_3$ (Sample 6), NCA with 2wt% Al$_2$O$_3$ (Sample 7) and NCA with

4wt%LFP (sample 8) (a); PSD results for NCA before and after dry particle fusion

(Sample 5) (b); SEM images of fresh NCA (c.d.e); SEM images of NCA after dry

particle fusion (f.g.h).

Figures 3.6A and a show EDS mapping results for Al for NCA with 1wt% Al$_2$O$_3$

(Sample 6) indicating that the particle surfaces were covered with a layer having higher

Al content, which proves that Al_2O_3 had been coated on the NCA surface using our dry

particle fusion technique. Figures 3.6B and b show EDS mapping results for NCA with

2wt% Al_2O_3 (Sample 7) indicating there was a more obvious and stronger elemental Al

signal on the surfaces of the NCA particles, compared to the samples coated with only

1wt% Al_2O_3. Figures 3.6C and c show EDS mapping results for P on the NCA with 4wt%

LFP sample (Sample 8). Figures 3.6D and d show EDS mapping results for Fe on the

surface of NCA particles coated with 10wt% LFP (Sample 9). Figures 3.6c, C, d and D

indicate that both samples had an LFP layer evenly and thoroughly coated on NCA

particle surface. Figure 3.6 shows that dry particle fusion is an efficient, environmentally

friendly method to apply coatings on particle surfaces by applying mechanical force as

particles are rotating and in principle it is a method that can be used to apply coatings

with no solvents or high vacuum methods required.
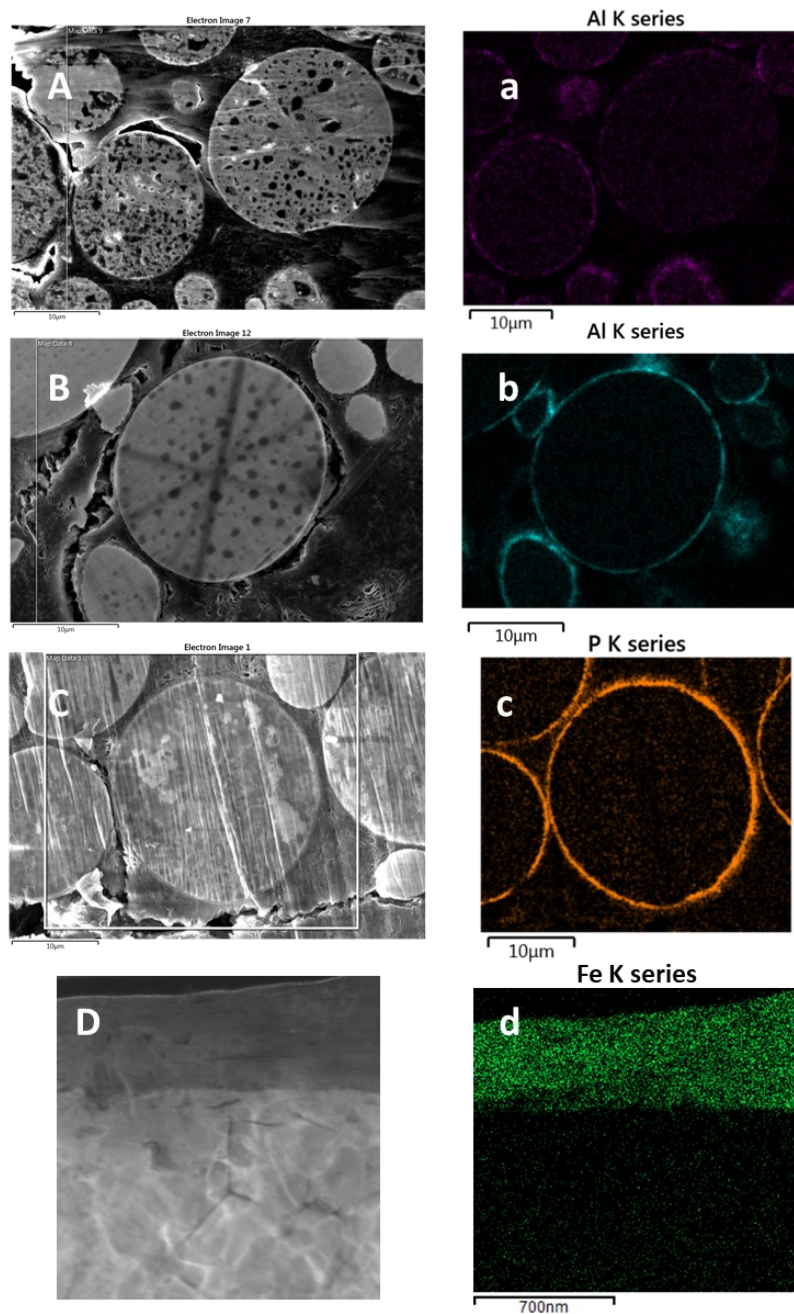
Figure 3.6. SEM micrographs and EDS mapping of Al on NCA coated with 1wt% Al_2O_3

(Sample 6) (A.a), Al on NCA coated with 2wt% Al_2O_3 (sample 7) (B.b), P on NCA

coated with 4wt% LFP (sample 8) (C.c), and Fe on NCA coated with 10wt% LFP

(sample 9) (D.d).

Figure 3.7 shows specific capacity versus cycle number results for coin cells containing LiNiO$_2$ (lithiated Ni(OH)$_2$) and lithiated Ni(OH)$_2$ + 2wt% Al$_2$O$_3$. The first two cycles were collected at a current corresponding to C/20 and followed by 50 cycles at a current corresponding to C/5. Finally, two further cycles at C/20 were collected. The data was collected at 30°C for cells cycled between 3.0 and 4.3 V. The two samples delivered similar specific capacities at C/20 at the beginning, but LiNiO$_2$ delivered less specific capacity at C/5 and degraded rapidly in the following 50 cycles. However, lithiated Ni(OH)$_2$ + 2wt% Al$_2$O$_3$ delivered an impressive specific capacity and showed much improved capacity retention compared to LiNiO$_2$. Figure 3.7 shows that lithiated Ni(OH)$_2$ + 2wt% Al$_2$O$_3$ shows much enhanced behavior, suggesting that dry particle fusion can be used to prepare excellent materials.
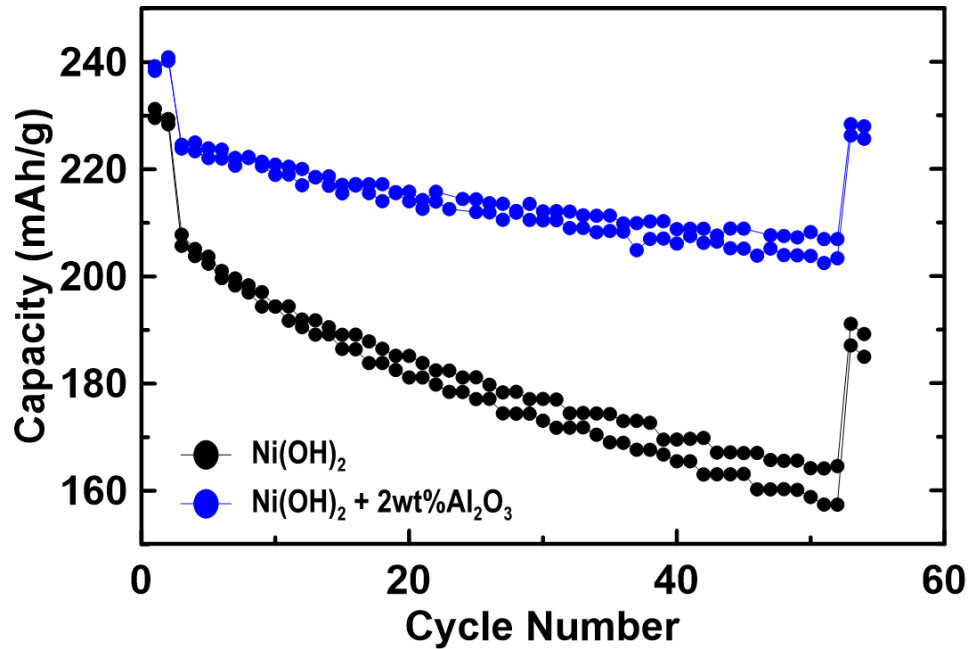
Figure 3.7 Specific capacity as a function of cycle number for $LiNiO_2$ (lithiated $Ni(OH)_2$) and lithiated $Ni(OH)_2$ + 2wt% Al_2O_3. The first two cycles were at C/20, the next 50 at C/5 and the last two at C/20.

3.4 Summary

In this chapter, we reported the construction and operation of an in-house constructed dry particle fusion instrument which was inexpensive to build.   Using Mössbauer spectroscopy it was shown that less than 0.01wt% Fe was introduced into typical samples by the process. Samples prepared by dry particle fusion on cores of $Ni(OH)_2$ and NCA showed virtually identical particle size distributions are the pristine core particles, indicating that the dry particle fusion method did not damage the core particles.   In addition, monitoring the hammer temperature versus time indicated that the dry particle

fusion process was repeatable from run to run. EDS mapping results showed nice coatings of both Al_2O_3 and $LiFePO_4$ on the surfaces of NCA after dry particle fusion. Coin cells testing data showed that lithiated $Ni(OH)_2$ + 2wt% Al_2O_3 (prepared by lithiating $Ni(OH)_2$ coated with 2wt% Al_2O_3 by dry particle fusion) had a better capacity retention than $LiNiO_2$. This suggests that dry particle fusion is an effective method to coat materials to improve their electrochemical performance. Dry particle fusion can be used to apply coatings with no solvents used and no high vacuum methods employed. We encourage others to adopt this simple effective method.

Chapter 4 Impact of Dry Particle Fusion Coating of Alumium Oxide on Ni-based Positive Electrode Materials for Li-ion Batteries

Ni-rich layered positive electrode materials $LiNi_xM_{1-x}O_2$ (M = Al, Mn, Mg or Co) have become a popular research area because Ni-rich layered materials have both high specific capacity and low material cost due to the low price of Ni compared to Co.[12,49,89] Li et al. have reported that Co is not necessary in Ni-rich positive electrode materials since materials with large specific capacity and equivalent or better capacity retention can be prepared by doping with other elements like Al, Mg and Mn in the absence of Co.[49] A paper by Aishova et al.[90] shows that $LiNi_{0.9}Mn_{0.1}O_2$ shows better performance than $LiNi_{0.9}Mn_{0.05}Co_{0.05}O_2$ (see Figure 7 in ref[90]) when tested in coin type half cells, confirming the work of Li et al..[49]

The typical Li transition metal oxide synthesis method used in industry begins with the production of a mixed transition metal hydroxide or carbonate precursor using a co-precipitation step. Then the precursor is heated along with Li_2CO_3 or $LiOH \bullet H_2O$ at temperatures between about 700 and 950°C, depending on composition, to make the oxide. Mixing substituent elements directly with Ni and other metals during the co-precipitation step can ensure a homogeneous distribution of substituent elements inside the precursor particles and subsequently in the oxide particles. But this method has some drawbacks. For Al substitutions, Al^{3+} cannot substitute directly for Ni^{2+}, Mn^{2+}, or Co^{2+} in $M(OH)_2$. Instead, a so-called layered double hydroxide (LDH) phase forms where an

anion like NO_3^-, SO_4^{2-} or CO_3^{2-} is incorporated between the $M(OH)_2$ slabs to balance the charge of two Al^{3+} ions.[91,92] This results in precursor materials which can be two phase and also have lowered tap density due to the incorporated anions. Other elements, like W, are hard to incorporate as a solid solution into $M(OH)_2$ phases via coprecipitation, because the most common formal of oxidation state of W is +6, instead of +2.[93] Insoluble $NiWO_4$[94,95] instead of a solid solution nickel tungsten hydroxide, most likely introduces W into the precursor during the coprecipitation step.

The above-mentioned drawbacks complicate material synthesis. Therefore, an alternative route to add substituent atoms to $LiMO_2$ materials is desired. Solid state synthesis has been reported to introduce substituent elements into Ni-containing positive electrode materials.[96–98] Mixing $Al(OH)_3$ and $Ni(OH)_2$ directly by grinding, then with a Li source and followed by a heating step to synthesize lithium mixed transition metal oxides with Al has been reported[96] but generally materials made in such a process are inferior due to potentially inhomogeneous distribution of Al. One advantage of this method is that it avoids the formation of the LDH (layered double hydroxide) phase, which is undesired in the precursor.[91]

Dry particle fusion or mechanofusion has been used for many years to prepare core particles that are coated with another material.[23,24,66–68,70,99] Recently, the research group of M. Obrovac has been using mechanofusion to prepare engineered particles of advanced materials for Li-ion batteries by coating Al_2O_3 on $LiNi_{0.6}Mn_{0.2}Co_{0.2}O_2$ and

embedding Si alloy particles into graphite layers.[23,24,70] These materials showed superior charge-discharge cycling performance in all cases. The uniformity of the coating layers on the surface of the core materials and the uniformity of the Si distribution within graphite drew our attention. We therefore became interested in synthesizing $LiNi_{1-x}Al_xO_2$ using dry particle fusion as a method to uniformly coat Al_2O_3 on core particles before heat treatment.

In this chapter, we investigated two approaches to synthesize Al-substituted Ni-rich layered material using dry particle fusion. The first method synthesizes the material by coating nano-Al_2O_3 on $Ni(OH)_2$ by dry particle fusion followed by heating with $LiOH•H_2O$. The second method synthesizes the material by coating nano-Al_2O_3 on $LiNiO_2$ followed by heating for 20 hours at elevated temperature to diffuse Al inside the cathode material particles. Particle size distribution (PSD), X-ray diffraction (XRD), scanning electron microscopy (SEM), energy dispersive spectroscopy (EDS) mapping and EDS line scans were performed to observe the properties of synthesized samples. Half-cells were made to check the electrochemical properties of the synthesized materials.

This Chapter is based on a paper published in Chemistry of Materials.[35] [Chenxi Geng et al. Chem. Mater. 2020, 32, 14, 6097–6104]. Reprinted with permission from Chemistry of Materials. Copyright 2020 American Chemical Society. [35] Chenxi Geng contributed to the conceptualization, material synthesis, material characterizations, and electrochemical tests; Aaron Liu contributed to the conceptualization. Jeff Dahn

contributed to the design of experiments, the interpretation of results as well as editing the manuscript.

4.1 Experimental Methods

Reagents used for synthesis of $LiNi_{1-x}Al_xO_2$ include nano-Al_2O_3 (< 50 nm, from Sigma-Aldrich), $Ni(OH)_2$ (15 micron, from Guizhou Zoomwe Zhengyuan Advanced Material Co., Ltd, China), $LiOH·H_2O$ (> 99.8%, FMC corporation). Reagents used for coin cells included Super-S carbon black (Timcal) and polyvinylidene difluoride (PVDF, Kynar 301F, Arkema), N-methyl-2-pyrrolidone (NMP, Sigma-Aldrich, 99.5%), lithium hexafluorophosphate ($LiPF_6$, BASF, 99.9%), fluoroethylene carbonate (FEC, BASF, 99.94%) and dimethyl carbonate (DMC, Shenzhen Capchem Technology Co., Ltd.).

A dry particle fusion instrument, described carefully in Chapter 3 was used for this chapter. Nano-Al_2O_3, $Ni(OH)_2$ and $LiNiO_2$ (LNO, synthesized at Dalhousie University) were used in this chapter. The samples prepared in this chapter, and their abbreviated names, are described in Table 4.1, which lists the parameters used during dry particle fusion. For example, samples PP and PPL stand for Pristine Precursor ($Ni(OH)_2$) and Pristine Precursor Lithiated, respectively. Sample 1PF stands for the $Ni(OH)_2$ precursor coated with 1wt% Al_2O_3 by dry particle fusion. Sample 1PFL stands for sample 1PF after it has been heat treated with $LiOH•H_2O$. 3LNOF stands for $LiNiO_2$ + 3wt% Al_2O_3 after dry particle fusion. Since a heating step was performed on 3LNOF instead of a

lithiation step, 3LNOFH will be used to represent the material after heating. The hammer temperature versus time[36] was recorded manually during dry particle fusion.

Table 4.1. Summary of the samples made by dry particle fusion in this chapter and their subsequent heat treatment.

Description	Precursor	Lithiated material	Core material weight (g)	Al_2O_3 weight (g)	Spinning speed (rpm)	Duration (min.)
Pristine $Ni(OH)_2$	PP	PPL	50.0	0	0	0
$Ni(OH)_2$ after dry particle fusion	PF	PFL	50.0	0	2400	60
$Ni(OH)_2$ + 1wt% Al_2O_3	1PF	1PFL	50.0	0.50	2400	60
$Ni(OH)_2$ + 2wt% Al_2O_3	2PF	2PFL	50.0	1.00	2400	60
$Ni(OH)_2$ + 3wt% Al_2O_3	3PF	3PFL	50.0	1. 50	2400	60
Description	Fusion	Heating	Core material weight (g)	Al_2O_3 weight (g)	Spinning speed (rpm)	Duration (min)
$LiNiO_2$ + 3wt% Al_2O_3	3LNOF	3LNOFH	50.0	1. 50	3600	60

A bowl angular velocity of 3600 rpm was chosen for dry particle fusion coating of $LiNiO_2$ while 2400 rpm was used for the coating of $Ni(OH)_2$. We learned that some $Ni(OH)_2$ core particles were fractured if angular velocities of 3600 or 3000 rpm were used. At 2400 rpm, no fracturing was observed by SEM or by PSA. By contrast, $LiNiO_2$ particles are more robust and could withstand 3600 rpm without fracturing.

The lithiation process was carried out as described in Chapter 2. The second step lithiation temperature for all lithiated samples in this chapter was 700°C. After dry particle fusion, the sample of $LiNiO_2$ coated with 3wt% Al_2O_3 (sample 3LNOF) was ground with additional $LiOH \cdot H_2O$ (with Li/Al = 1.02) to compensate for the additional Al_2O_3 and heated again at 700°C for 20 hours under oxygen flow to diffuse Al inside the cathode material particles to make sample 3LNOFH).

SEM, EDS, PSD, XRD and coin cell long-term cycling were performed as described in Chapter 2. Electrolyte with 1.2 M $LiPF_6$ in FEC:DMC (1:4 v/v) was used for the half coin cell long-term cycling tests as this electrolyte gives better long-term lithium metal cycling.

4.2 Results and Discussion

The abbreviated sample names in Table 4.1 will be used to describe the samples in this section.

Figure 4.1a shows the hammer temperature versus time during dry particle fusion for four samples: $Ni(OH)_2$ (Sample PF) and $Ni(OH)_2$ with 1, 2 and 3wt% Al_2O_3 (Samples 1PF, 2PF and 3PF). Temperatures increased as the bowl and hammer heated to an equilibrium value (near 40°C) due to the friction between the hammer, the particles, and the bowl. The hammer temperature stabilized at about 40°C for all samples, demonstrating the reproducibility of the process. Figure 4.1b shows the particle size distribution results for

pristine $Ni(OH)_2$ (Sample PP) as well as $Ni(OH)_2$ after dry particle fusion (Sample PF) and $Ni(OH)_2$ with 1, 2 and 3wt% Al_2O_3 (Samples 1PF, 2PF and 3PF) after dry particle fusion. The particle size distribution results for samples with or without dry particle fusion did not change significantly, indicating that core particles were not fractured under the condition of 2400 rpm for 60 minutes.

Figure 4.1c shows the hammer temperature versus time for $LiNiO_2$ with 3wt% Al_2O_3 (Sample 3LNOF) during dry particle fusion at a higher angular velocity of 3600 rpm. The hammer temperature vs. time curve followed the same trend as in Figure 4.1a, but it increased to just above 80°C and stabilized, demonstrating the success of the fusion process. The stabilized hammer temperature varies with different materials and with the angular velocity selected for the coating procedure. Figure 4.1d shows the particle size distribution results for fresh LNO and LNO with 3wt%Al_2O_3 (Sample 3LNOF). The particle size distribution did not change, demonstrating that particles were not broken after dry particle fusion under the condition of 3600 rpm for 60 minutes. It is our experience that heated oxides, like $LiNiO_2$, are more robust than hydroxides, like $Ni(OH)_2$, when used as core particles. This is why we selected a higher angular velocity for coating $LiNiO_2$. SEM images of both precursors and lithiated positive electrode materials before and after dry particle fusion have been presented in chapter 3 and show typical morphology of particles.
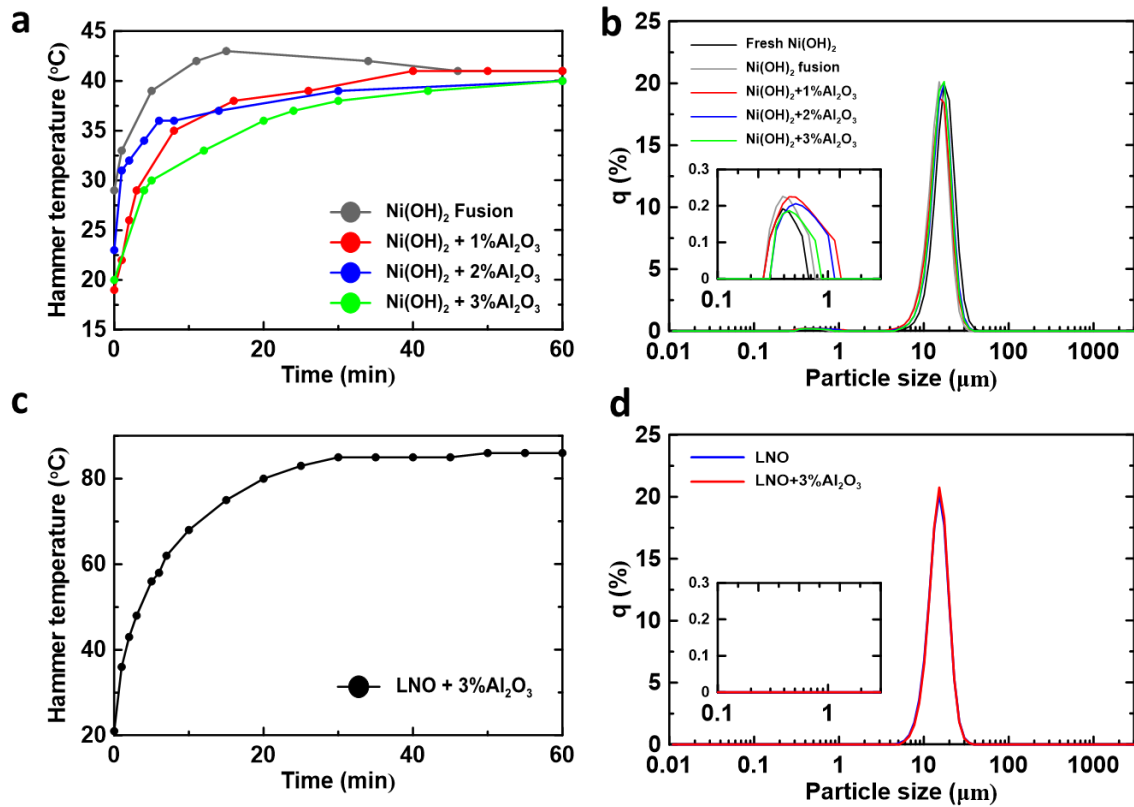
Figure 4.1. Hammer temperature vs. time during dry particle fusion of (a) and PSD results for (c) Ni(OH)$_2$ (Sample PF) and Ni(OH)$_2$ with 1, 2 and 3wt% Al$_2$O$_3$ (Samples 1PF, 2PF and 3PF); Hammer temperature vs. time during dry particle fusion of (b) and PSD results for (d) LiNiO$_2$ and LiNiO$_2$ with 3wt% Al$_2$O$_3$ (Sample 3LNOF).

XRD patterns were collected to study the structure of the corresponding lithiated materials. Rietveld refinements were performed assuming an α-NaFeO$_2$ (space group R$\overline{3}$m) hexagonal layered structure in which Li occupies the 3a site, transition metals and Al occupy the 3b site, and oxygen occupies the 6c site. Figures 4.2a1-e1 show the XRD patterns of lithiated pristine Ni(OH)$_2$ (Sample PPL) as well the other lithiated materials (Sample PFL, 1PFL, 2PFL and-3PFL) after the precursors were reacted with LiOH•H$_2$O at 700°C. Figure 4.2f1 shows the XRD pattern of LiNiO$_2$ with 3wt% Al$_2$O$_3$ after heat treatment at 700°C for 20 hours (Sample 3LNOFH). Figures 4.2 a2-f2 and a3-f3 are expanded views of the (104) Bragg peak between scattering angles of 44° and 45° and the (018) and (110) peaks between scattering angles of 63.5° and 65.5° for the respective materials.

Figures 4.2a-f demonstrate that all samples show a well-developed layered structure without observable impurities. The clear splitting of the (006/102) and (018/110) peaks indicate a well-ordered structure for LiNiO$_2$ (sample PPL). As the Al content increases, the splitting becomes less noticeable, which suggests Al successfully diffused inside the particles. Figures 4.2g-h show the a and c lattice constants as a function of the percent of Al substituent. The red curve shows the data for samples PPL, 1PFL, 2PFL and 3PFL and the black curve shows the data for Al-substituted samples made from Al-containing precursors made directly by co-precipitation reported in the literature.[49] Both the a and c lattice constants follow the same trend as the Al substituted samples made by co-

precipitation, followed by lithiation, also suggesting Al has successfully diffused inside the particles of sample– PPL, 1PFL, 2PFL and 3PFL. Figure 4.2 shows that the 104 and 018/101 peaks broaden as the amount of aluminum incorporated into the samples increases. It is our opinion that this is due to a decrease in crystallite grain size caused by aluminum incorporation. Table 4.2 summarizes the refinement results for the lattice constants, a and c, and the amount of Ni in the Li layer of all the samples.
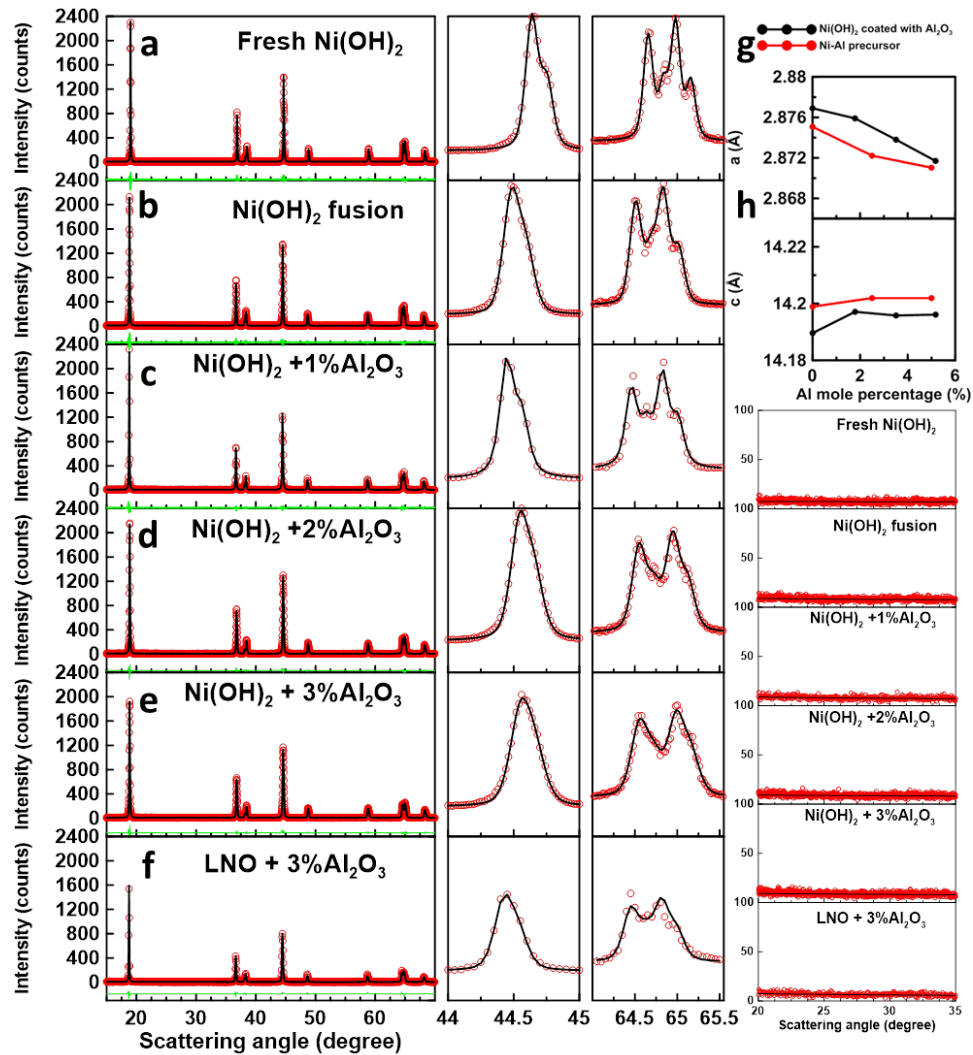
Figure 4.2. XRD patterns, expanded view of the (104) Bragg peak, the (018)/(110) Bragg peaks and impurity regions of XRD patterns sample PPL (a); sample PFL (b); sample 1PFL (c); sample 2PFL (d); sample 3PFL (e); sample 3LNOFH (f); lattice constant a (g) and c (h) as a function of Al mole percentage for lithiated samples PPL, 1PFL, 2PFL and 3PFL as well as Ni-Al precursors made by co-precipitation from ref [49].

89

Table 4.2. Lattice constants, Al to Al+Ni molar ratio and percentage of Ni atoms filling sites in the Li layer of the synthesized samples.

Sample	Description	Al/(Al+Ni) molar ratio	a (Å) ±0.0001 Å	c (Å) ±0.001 Å	Ni in Li layer % ±0.2 %
PPL	Pristine $Ni(OH)_2$ lithiated	0.0	2.8766	14.187	2.1
PFL	$Ni(OH)_2$ subjected to dry particle fusion then lithiated	0.0	2.8769	14.190	2.0
1PFL	$Ni(OH)_2$ + 1wt%Al_2O_3 lithiated	0.0179	2.8759	14.197	1.6
2PFL	$Ni(OH)_2$ + 2wt%Al_2O_3 lithiated	0.0351	2.8738	14.196	1.6
3PFL	$Ni(OH)_2$ + 3wt%Al_2O_3 lithiated	0.0517	2.8716	14.197	1.3
3LNOFH	$LiNiO_2$ + 3wt%Al_2O_3 after dry particle fusion and heating	0.0544	2.8748	14.191	2.8

Figure 4.3a shows the specific discharge capacity vs. cycle number of lithiated pristine Ni(OH)$_2$ (Sample PPL), lithiated Ni(OH)$_2$ after dry particle fusion (Sample PFL), lithiated Ni(OH)$_2$ with 1wt% (Sample 1PFL), 2wt% (Sample 2PFL) and 3wt% Al$_2$O$_3$ (Sample 3PFL). Coin cells were tested between 3.0 - 4.3 V using a current corresponding to C/20 for the first two cycles, followed by 50 cycles using a current corresponding to C/5 and two further cycles were collected at C/20 at the end. All samples delivered similar discharge capacities, within 10 mAh/g, at C/20 at the beginning of testing. The capacity retention improved as the Al content increased for the samples made by dry particle fusion of Al$_2$O$_3$ on Ni(OH)$_2$ followed by heating with LiOH•H$_2$O. Sample 3PFL with 3wt% Al$_2$O$_3$ had both impressive specific discharge capacity and capacity retention.

Figure 4.3b shows the voltage vs. specific capacity (V vs. Q) curve of the above-mentioned materials during the 1st cycle at C/20. Lithiated pristine Ni(OH)$_2$ (sample PPL) had distinct plateaus and steps during charge and discharge, representing phase transitions and single phase regions as reported initially by T. Ohzuku et al.[100] and W. Li et al.[101] and later by H. Li et al.[37].   The V vs. Q curves became smoother with increasing amounts of Al suggesting the suppression of phase transitions.[49] Table 4.3 summarizes the first charge capacity, the first discharge capacity, the irreversible capacity and percentage of Ni atoms filling sites in the Li layer of the synthesized samples. PPL, PFL, 1PFL and 2PFL had similar irreversible capacities (IRCs) of 13.0, 14.0, 11.4 and

14.6 mAh/g respectively, and 3PFL had a slightly larger IRC, 17.3 mAh/g, because less capacity was delivered from the kinetic hindrance region for 3PFL.

Figure 4.3c shows dQ/dV vs. V curves of the samples mentioned in last paragraph during the 1st discharge and 2nd charge at C/20. Four pairs of peaks (i, ii, iii and iv) have been circled, which represent the kinetic hindrance peak in the H1 phase, the H1-M phase transition peaks, the M-H2 phase transition peaks, and the H2-H3 phase transition peaks, respectively.[37,102] The dQ/dV vs. V peaks of lithiated pristine $Ni(OH)_2$ (Sample PPL) and lithiated $Ni(OH)_2$ after dry particle fusion (Sample PFL) were sharp and intense representing clear phase transitions. These peaks became less intense and broader as the Al content in the samples increased from samples 1PFL to 3PFL, indicating that the phase transitions were suppressed[49] and Al had successfully diffused inside the particles.
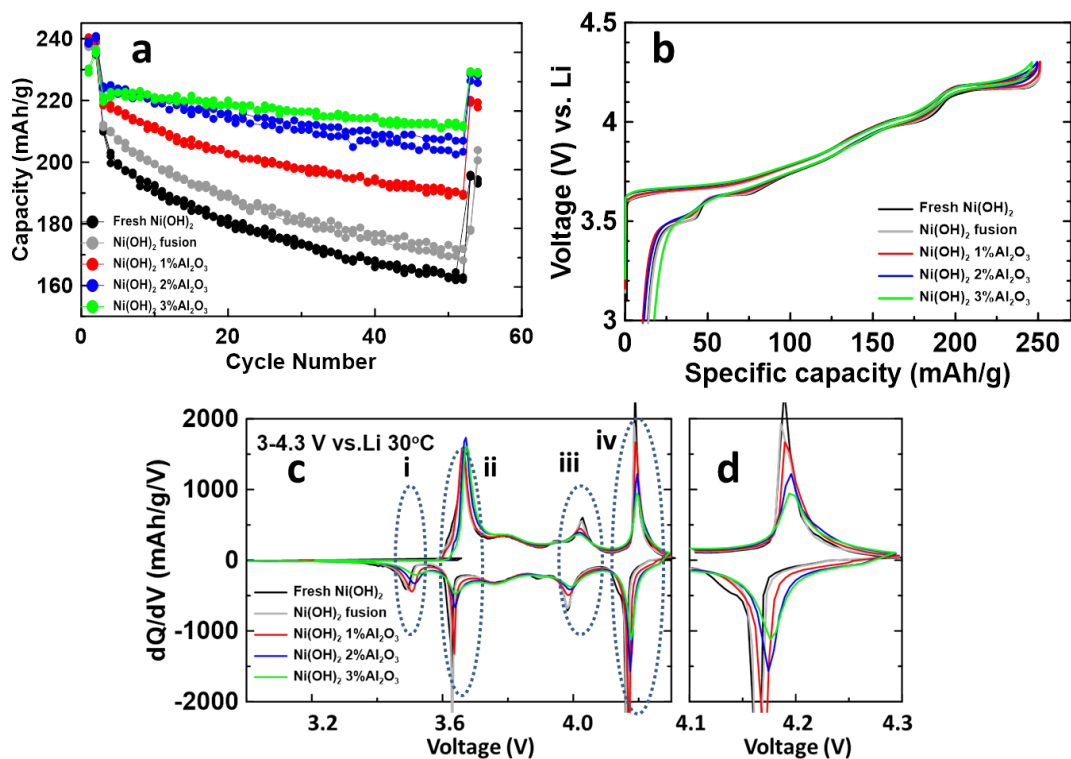
Figure 4.3. Specific capacity as a function of cycle number (a), V vs. Q curves (b), dQ/dV vs. V curves (c) and dQ/dV vs. V curves from 4.1 V to 4.3 V (d) for the 1st discharge and 2nd charge of samples PPL, PFL, 1PFL, 2PFL and 3PFL (see Table 4.1).

Cross-sectional SEM, EDS mapping and EDS line scans were used to determine the Al distribution inside the particles. Figures 4.4a, b and c show SEM images, EDS mapping and Al line scans for sample 3PFL (lithiated $Ni(OH)_2$ with 3wt% Al_2O_3). EDS mapping shows that Al was basically uniformly distributed inside the particles and the line scan also shows the same result. Figures 4.4d, e and f show SEM images, EDS mapping and an EDS line scan of LNO with 3wt%Al_2O_3 after heat treatment (sample 3LNOFH)

93

indicating that Al also had diffused inside the particles. The blue lines in Figures 4.4a

and d are the EDS line scans for Ni. The ratio of Al to Ni signal in Figure 4.4d is smaller

than that in Figure 4.4a, suggesting less Al diffused inside particles of sample 3LNOFH.
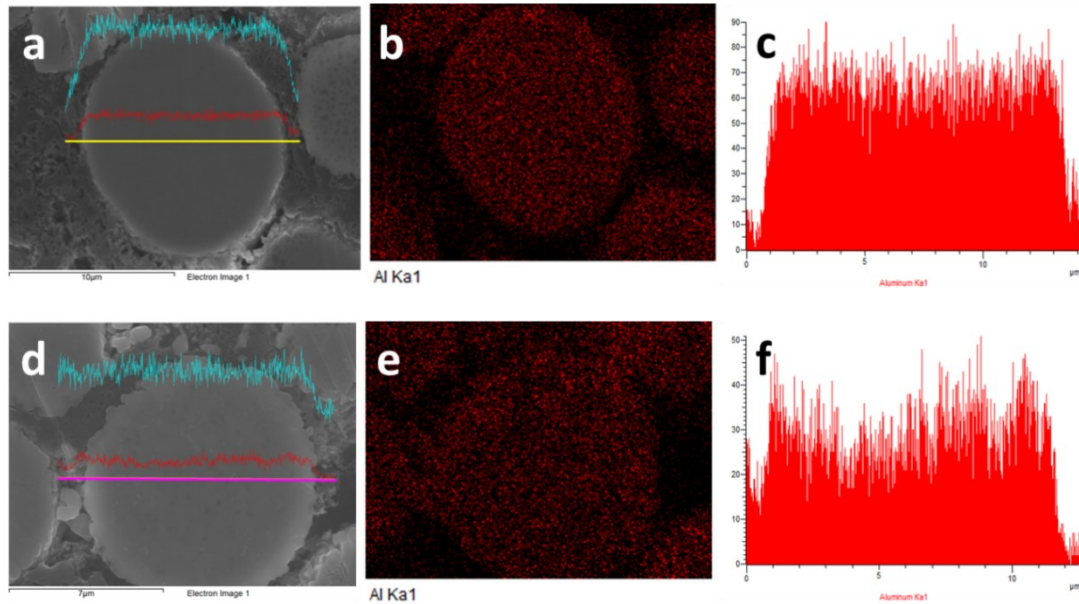
Figure 4.4. SEM, EDS mapping and line scan of Al (red) and Ni (blue) on lithiated

Ni(OH)$_2$ with 3wt%Al$_2$O$_3$ (sample 3PFL) (a, b, c) and LNO with 3wt%Al$_2$O$_3$ after

heating(Sample 3LNOFH) (d, e, f). The blue lines in a and d are the EDS line scan of Ni.

Sample 3PFL (lithiated Ni(OH)$_2$ with 3wt% Al$_2$O$_3$) and sample 3LNOFH (LNO with 3wt%

Al$_2$O$_3$ followed by heat treatment) have similar Al contents of 5.17 and 5.44 mole %

shown in Table 4.2, suggesting that the cycling performance of these two materials

should be comparable. Figure 4.5 shows the specific discharge capacity vs. cycle number

of samples 3PFL and 3LNOFH. Coin cell cycling was collected in the same way as in

Figure 4.3. The initial specific discharge capacity of sample 3LNOFH was lower than both LiNiO$_2$ (sample PPL) and sample 3PFL and the capacity retention was not improved compared to LiNiO$_2$, suggesting that heating LiNiO$_2$ which has been coated by Al$_2$O$_3$ using dry particle fusion is not effective for improving electrochemical performance.

Figure 4.5b shows the voltage vs. specific capacity (V vs. Q) curves of the above-mentioned three materials during the 1st cycle using a current of C/20. Sample 3LNOFH also displayed obvious plateaus during charge and discharge like LiNiO$_2$, possibly because less Al, not enough to hinder phase transitions, had diffused inside the particles. 3LNOFH had a large IRC, 32.2 mAh/g, because almost no capacity was delivered from the kinetic hindrance region. The percentage of Ni atoms filling sites in the Li layer may have an impact on the capacity that can be accessed from the kinetic hindrance region. The more Ni in the Li layer, the harder it is for Li to diffuse when the Li layer is almost full, because the inactive Ni will hinder Li diffusion. The amount of Ni in the Li sites for 3LNOFH and 3PFL are 2.8% and 1.3%, respectively. So, the larger amount of Ni in the Li sites of 3LNOFH would be a possible reason for its smaller discharge capacity, which is mainly due to less capacity delivered from the kinetic hindrance region.

Figures 4.5c, d and e show dQ/dV vs. V curves of sample PPL (LiNiO$_2$), sample 3PFL and sample 3LNOFH during the 2nd cycle (black) and the 54th cycle (red) at C/20. The kinetic hindrance peak near 3.5 V and the H2-H3 phase transition peak of samples PPL and 3LNOFH show decreases in peak intensity, while those of sample 3PFL did not

change in peak intensity or shape, suggesting less degradation of the material. This suggests that coating Al_2O_3 on $Ni(OH)_2$ by dry particle fusion before heating with $LiOH \cdot H_2O$ is an attractive approach for synthesizing high Ni content layered cathode materials with substituted Al. One possible reason for the difference between the performance of 3LNOFH and 3PFL is that the $Ni(OH)_2$ precursor is more porous than $LiNiO_2$. Therefore, during dry particle fusion, it is likely that Al_2O_3 was "pushed" into these pores, resulting in better contact between the alumina and the core particle. Then during heating with $LiOH \cdot H_2O$, one might expect more uniform incorporation of Al throughout the particles.
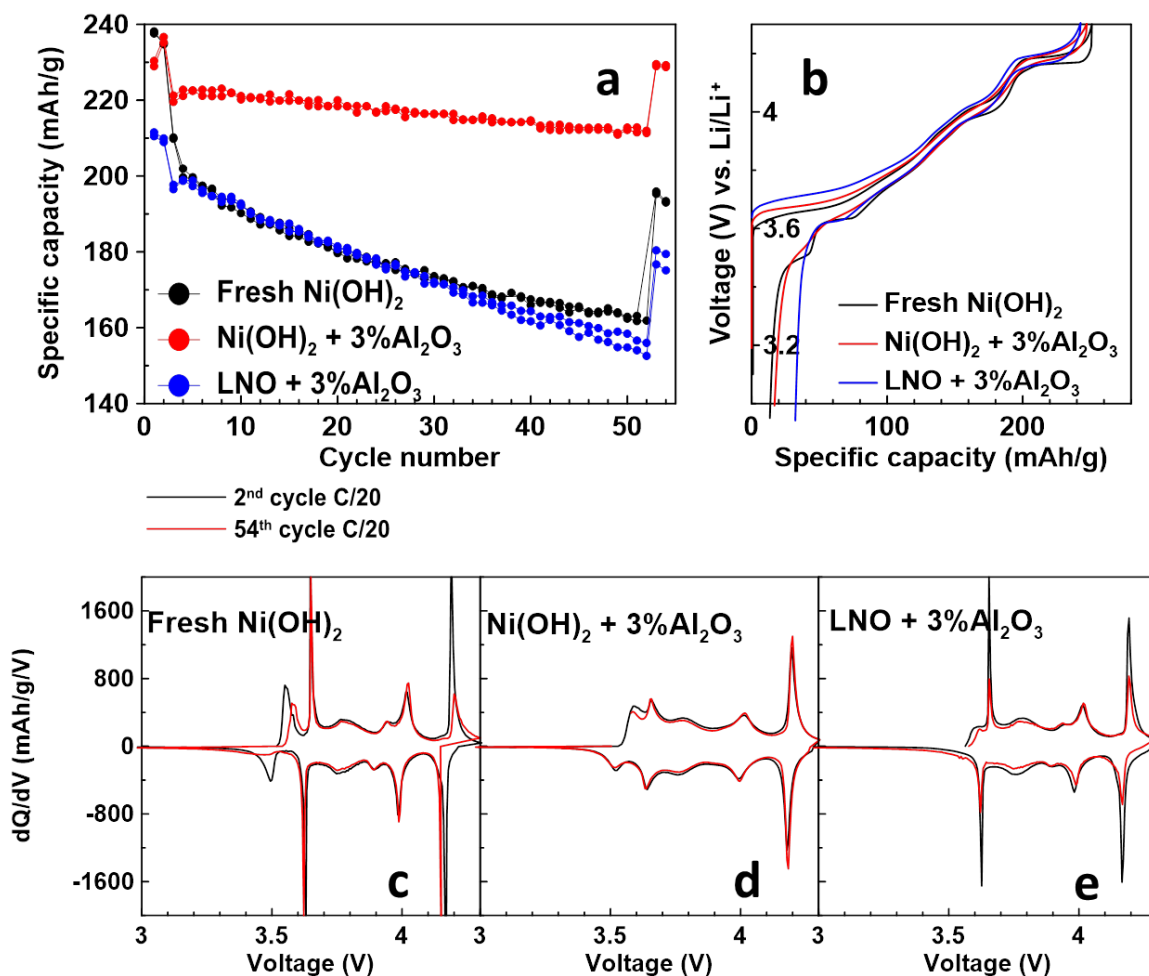
Figure 4.5. Specific capacity as a function of cycle number (a), V vs. Q curves of 1st cycle (b) of lithiated pristine Ni(OH)$_2$ (Sample PPL), lithiated Ni(OH)$_2$ with 3wt% Al$_2$O$_3$ (Sample 3PFL) and LiNiO$_2$ with 3wt% Al$_2$O$_3$ after heating (Sample 3LNOFH); dQ/dV vs. V curves of the 2nd (black) and 54th (red) cycle of sample PPL (c), sample 3PFL (d), and sample 3LNOFH (e).

In order to verify the reproducibility of this approach, two more batches of samples were prepared by coating Ni(OH)$_2$ with Al$_2$O$_3$ (exactly like sample 3PF) followed by heat treatment with LiOH•H$_2$O (exactly like sample 3PFL). These batches are called batch 2

and batch 3, respectively. Figure 4.6 compares the electrochemical performance of the samples from batches 1 (as shown in Figure 4.2, Figure 4.3, Figure 4.4 and Figure 4.5), 2 and 3.

Coin cell cycling was also collected using a same procedure as used for the data of Figure 4.3, and coin cell cycling for batches 2 and 3 was collected for another 50 cycles at C/5 with 2 cycles at C/20 at the end. Figure 4.6a shows the specific discharge capacity vs. cycle number of batches 1, 2 and 3 of $Ni(OH)_2$ coated with 3wt% Al_2O_3 followed by lithiation (all batches made like sample 3PFL). All three batches had specific discharge capacities greater than 210 mAh/g at the beginning as well as impressive capacity retention. The initial specific discharge capacity of batches 2 and 3 were lower than batch 1, while the capacity retention was improved compared to batch 1 and the delivered specific discharge capacities were close to that of batch 1 at the 54th cycle at C/20.

Figure 4.6a shows the voltage vs. specific capacity (V vs. Q) curves of the above mentioned three batches during the 1st cycle using a current of C/20. The discharge curves were similar for the three batches, but batches 2 and 3 delivered less capacity at the 3.5 V and 4.2 V plateaus, explaining smaller specific capacity during the initial cycles for batches 2 and 3 in Figure 4.6a. Batch 2 and Batch 3 had larger IRCs than Batch 1, which is related to low capacity in the kinetic hindrance region.

Figure 4.6c, d and e show dQ/dV vs. V curves of batches 1, 2 and 3 during the 2nd cycle (black) and the 54th cycle (red) at C/20. All three batches showed good stability of the dQ/dV peaks over the 50 cycles. The kinetic hindrance peak, near 3.5 V, showed an increase in peak intensity for batches 2 and 3, while that of batch 1 did not change in peak intensity or shape, which possibly explained the better capacity retention of batches 2 and 3, since more capacity was delivered gradually from the kinetic hindrance region in the cycles after the initial one. Similar behavior was also observed by Liu et al.[103], indicating that the kinetic hindrance region can influence the cycling performance of Ni-rich layered materials. Table 4.3 shows the amount of Ni in the Li sites of Batch 1, Batch 2 and Batch 3 are $1.3 \pm 0.2\%$, $1.2 \pm 0.2\%$, and $1.6 \pm 0.2\%$. Within error, these values are almost the same. Batch 1 had the largest capacity delivered from the kinetic hindrance region, while Batches 2 and 3 had smaller capacity and their capacities delivered from kinetic hindrance region were similar to each other. The kinetic hindrance region is a "touchy" region, and its behavior has not been well explained yet. It is certainly related to the rate of Li diffusion, which requires a more detailed study in the future. Zsoldos et al.[104] and Phattharasupakun et al.[44] have both reported that the lithium diffusivity is highly related to the amount of Ni in Li site in the kinetic hindrance region. More Ni in the Li site hinders the lithium-ion diffusion pathway resulting in less capacity delivered in kinetic hindrance region. Besides, Zsoldos et al. also observed that the synthesis conditions sometimes have a great impact on lithium diffusivity, even though materials

have similar amounts of Ni on the Li site. Therefore, the author speculates that the lower specific capacity delivered for batches 2 and 3 compared to batch 1 is more a result of the variation in synthesis conditions, such as oxygen flow rate, impurities induced during precursors mixing with $LiOH \cdot H_2O$, since all three batches have very similar amounts of Ni in the Li layer.

Overall, all the three batches delivered similar specific discharge capacities and had good capacity retention, which demonstrates the reproducibility of this approach. Obviously, we feel that industrial suppliers could improve upon the reproducibility of samples made by this method.
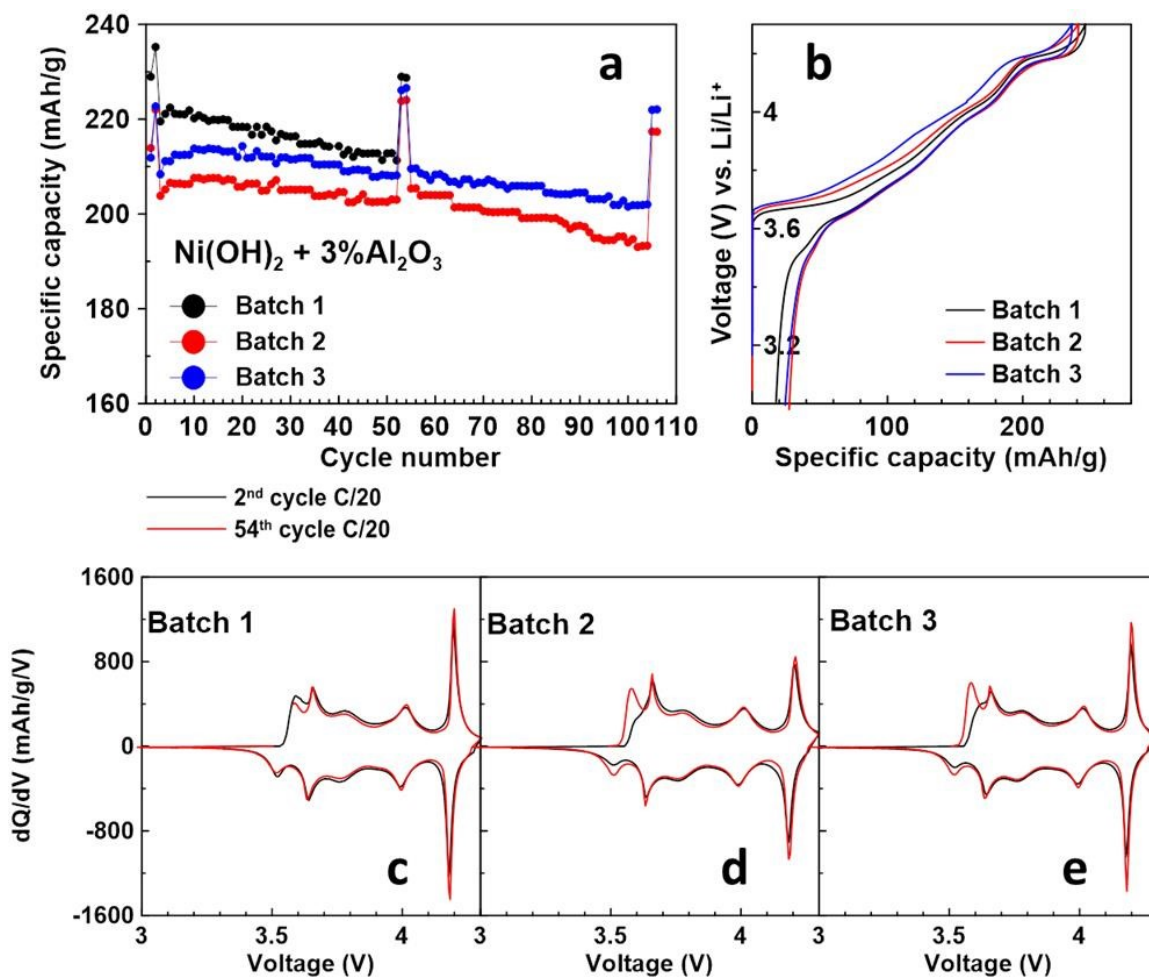
Figure 4.6. Specific capacity as a function of cycle number (a), V vs. Q curves of the 1st cycle (b) of batches 1, 2 and 3 of Ni(OH)$_2$ with coated with 3wt% Al$_2$O$_3$ by dry particle fusion followed by heating with LiOH•H$_2$O (made as Sample 3PFL); dQ/dV vs. V curves of the 2nd cycle (black) and 54th (red) cycle of batch 1 (c), batch 2 (d) and batch 3 (e) of these materials.

Table 4.3. The first charge capacity, the first discharge capacity, the irreversible capacity and percentage of Ni atoms filling sites in the Li layer of the synthesized samples.

Sample	Description	First Charge capacity mAh/g	First Discharge capacity mAh/g	Irrevesible capacity mAh/g	Ni in Li layer % ±0.2 %
PPL	Pristine $Ni(OH)_2$ lithiated	250.8(2)	237.8(3)	13.0(5)	2.1
PFL	$Ni(OH)_2$ subjected to dry particle fusion then lithiated	251.7(5)	237.7(5)	14.0(1)	2.0
1PFL	$Ni(OH)_2$ + 1wt%Al_2O_3 lithiated	250.9(3)	239(1)	11.4(7)	1.6
2PFL	$Ni(OH)_2$ + 2wt%Al_2O_3 lithiated	249.5(1)	238.8(4)	10.6(5)	1.6
3PFL Batch 1	$Ni(OH)_2$ + 3wt%Al_2O_3 lithiated	246.8(5)	229.7(7)	17.1(2)	1.3
3PFL Batch 2	$Ni(OH)_2$ + 3wt%Al_2O_3 lithiated	241.2	213.9	27.3	1.2
3PFL Batch 3	$Ni(OH)_2$ + 3wt%Al_2O_3 lithiated	236.1(2)	210(2)	26.1(2)	1.6
3LNOFH	$LiNiO_2$ + 3wt%Al_2O_3 after dry particle fusion and heating	241.8(9)	209.5(9)	32.2(1)	2.8

To see if the best material, 3PFL in this chapter is still good compared to other layered oxide materials, the data of the specific capacity delivered at the first cycle at a specific current of C/20 vs. the capacity retention after 50 cycles at a specific current of C/5 of 26 sets of coin cells together with the 3PFL coin cell are plotted in Figure 4.7. The 26 sets of coin cell data were collected from the reference[48] reported by Li et al. and the coin cells were made at Dalhousie using layered oxide materials either provided by different industrial vendors or synthesized at Dalhousie. All the cells were cycled at 30 ºC with the same LCV of 3.0 V and different UCVs ranging from 4.1 V to 4.4 V at a current of

C/20 for the first 2 cycles and C/5 for the next 50 cycles. Samples with the same stoichiometry were from different venders. Readers can refer to reference[47] for further details of sample and cycling information. Figure 4.7 shows that the 3PFL marked by red circle had both good specific discharge capacity and capacity retention, demonstrating the good performance of this material.
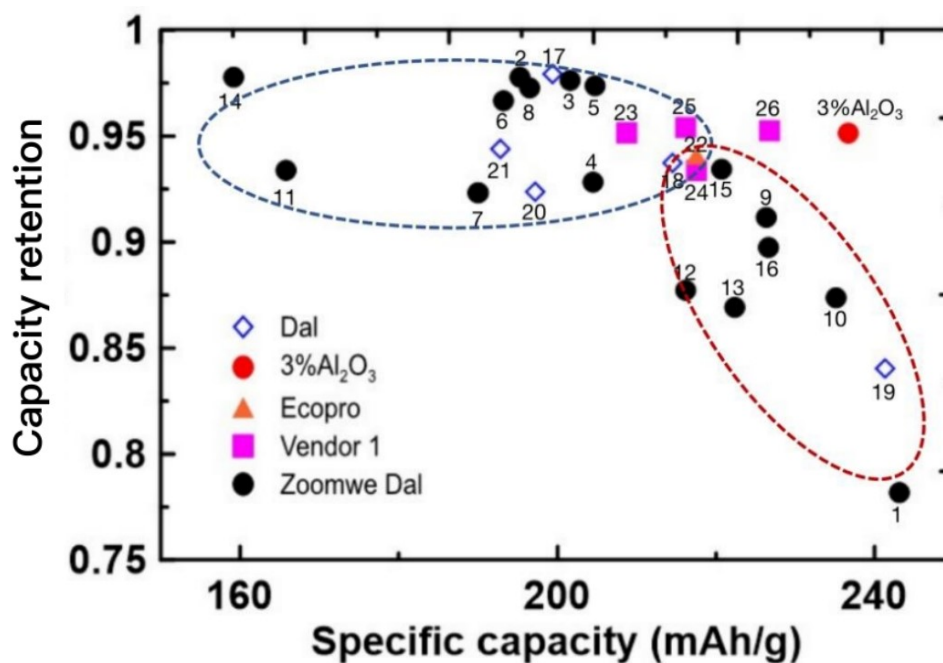
Figure 4.7 Capacity retention after 50 cycles (C/5) as a function of the 1st C/20 discharge capacity for the materials listed in Table 4.4 and the 3PFL (batch 1) sample in this chapter. Adapted with permission from H. Li, A. Liu, N. Zhang, Y. Wang, S. Yin, H. Wu, J. R. Dahn, *Chemistry of Materials* **2019**, *31*, 7574.[47] Copyright 2019, American Chemical Society.

Table 4.4 The stoichiometries of samples plotted in Figure 4.7. The numbers represent the points and the same number was marked next to the corresponding point in Figure 4.7. PC and SC represent polycrystal and single crystal, respectively.

No.	Sample	No.	Sample
1	$LiNiO_2$	2	$LiNi_{0.89}Co_{0.06}Al_{0.03}Mg_{0.02}O_2$
3	$LiNi_{0.92}Co_{0.03}Al_{0.03}Mg_{0.02}O_2$	4	$LiNi_{0.95}Al_{0.03}Mg_{0.02}O_2$
5	$LiNi_{0.89}Co_{0.06}Al_{0.03}Mg_{0.02}O_2$	6	$LiNi_{0.92}Co_{0.03}Al_{0.03}Mg_{0.02}O_2$
7	$LiNi_{0.95}Al_{0.03}Mg_{0.02}O_2$	8	$LiNi_{0.95}Mg_{0.05}O_2$
9	$LiNi_{0.975}Mg_{0.025}O_2$	10	$LiNi_{0.99}Mg_{0.01}O_2$
11	$LiNi_{0.90}Co_{0.05}Al_{0.05}O_2$	12	$LiNi_{0.90}Co_{0.05}Al_{0.05}O_2$
13	$LiNi_{0.90}Co_{0.05}Al_{0.05}O_2$	14	$LiNi_{0.95}Al_{0.05}O_2$
15	$LiNi_{0.95}Al_{0.05}O_2$	16	$LiNi_{0.95}Al_{0.05}O_2$
17	$LiNi_{0.95}Mg_{0.05}O_2$	18	$LiNi_{0.95}Mg_{0.05}O_2$
19	$LiNi_{0.9875}Al_{0.0125}O_2$	20	$LiNi_{0.6}Mn_{0.2}Co_{0.2}O_2$ PC
21	$LiNi_{0.6}Mn_{0.2}Co_{0.2}O_2$ SC	22	$LiNi_{0.80}Co_{0.15}Al_{0.05}O_2$
23	$LiNi_{0.8}Mn_{0.1}Co_{0.1}O_2$ SC	24	$LiNi_{0.8}Mn_{0.1}Co_{0.1}O_2$ SC
25	$LiNi_{0.8}Mn_{0.1}Co_{0.1}O_2$ PC	26	$LiNi_{0.8}Mn_{0.1}Co_{0.1}O_2$ PC

4.3 Summary

Dry particle fusion was used to coat Al_2O_3 on $Ni(OH)_2$ and on $LiNiO_2$. The hammer temperature versus time during dry particle fusion showed the reproducibility of the process. Particle size distribution analysis showed that core particles did not break after the fusion process.

The Al_2O_3 coated $Ni(OH)_2$ samples were heated with $LiOH \cdot H_2O$ in a two-step heating procedure. The Al_2O_3 coated $LiNiO_2$ sample was also heat treated. After heat treatment, cross-sectional SEM and EDS line scans of Al showed that the Al had diffused inside the particles for both materials. X-ray diffraction patterns showed that all the samples displayed a well-developed layered structure. The lattice constant variation vs. at% Al for the samples made from Al_2O_3 coated $Ni(OH)_2$ followed the same trend as materials made from co-precipitated $Ni_{1-x}Al_x(OH)_2$ precursors in reported the literature, consistent with Al diffusing inside the particles.

Coin cell tests showed the samples made from Al_2O_3 coated $Ni(OH)_2$, followed by heat treatment with $LiOH \cdot H_2O$, had improved charge-discharge cycling performance which improved as the Al content increased. The sample with 3 wt. % Al_2O_3 had both excellent capacity retention and specific capacity, while the sample prepared by coating 3wt% Al_2O_3 directly on $LiNiO_2$, followed by heating, had poor capacity retention. Two more batches of Al_2O_3 coated $Ni(OH)_2$, followed by heat treatment with $LiOH \cdot H_2O$, were

made and coin cell testing results verified the reproducibility of this approach. Dry particle fusion coating of Al_2O_3 (and presumably other materials) directly on $Ni(OH)_2$ precursor followed by heat treatment with a lithium source appears to be an excellent way to prepare next generation Co-free positive electrode materials for Li-ion batteries. In this thesis, we further applied coatings of WO_3 and Ta_2O_5 on $Ni(OH)_2$ precursor and heat treated the WO_3- and Ta_2O_5-coated precursors with a lithium source later on to prepare positive electrode materials and investigate the mechanism of action of W and Ta on LNO, which will be shown in Chapter 5 and 6 respectively.

Chapter 5 Mechanism of Action of the Tungsten Dopant in LiNiO₂ Positive Electrode Materials

Ni-rich layered Li transition metal oxides, such as $LiNi_xCo_yAl_{1-x-y}O_2$ (NCA, $x > 0.8$) and $LiNi_xMn_yCo_{(1-x-y)}O_2$ (NMC, $x \geq 0.5$), are the top choices of cathode materials for electric vehicles owing to their superior energy and power densities[1,105–110]. However, the practical capacity of many commercial Ni-rich cathodes is still limited to < 200 mAh/g to guarantee a long cycle life, and the incorporated Co is becoming increasingly problematic in terms of price and sustainability. To overcome these limitations, increasing the fraction of Ni in the materials to increase the capacity and reducing the use of Co is a common strategy. However, materials with a very high Ni content show faster chemo-mechanical degradation such as microcracking of secondary particles during charge discharge cycling[48,49]. Hence, preparing high-Ni cathodes with satisfactory cycling stability remains challenging.

Many researchers have worked very hard to solve this problem. The addition of tungsten (W) has been reported to be particularly effective to improve the cycling stability of Ni-rich and Li-rich materials[11,12,51–54]. However, it was unclear whether the W dopant is in the TM sites as a substituent or stays in a second phase. W^{6+} is the most stable oxidation state of W and is closest in size to Ni^{3+} so one would expect W^{6+} to be the oxidation state of W substituted for Ni in LiNiO₂. However, such a substitution will create numerous defects and structural distortions to balance the charge difference, which is unlikely to be

energetically favorable. Therefore, a close examination of the location of W in LiNiO$_2$ and the corresponding mechanism that is responsible for improving charge-discharge capacity retention was performed in this chapter.

In this chapter, we investigated the mechanism of action of W in LiNiO$_2$ (LNO). LNO with different mole ratios of W:(Ni+W) (0.5, 1, 2 and 4 mol%), which are denoted as W0.5-LNO, W1-LNO, W2-LNO and W4-LNO, were synthesized by coating nano-sized WO$_3$ on Ni(OH)$_2$ by a dry particle fusion method reported in Chapter 3, followed by heating with LiOH·H$_2$O. W-containing Ni(OH)$_2$ precursors were also prepared by co-precipitation and these were subsequently heated with LiOH·H$_2$O. X-ray diffraction (XRD) and electron energy loss spectroscopy (EELS) experiments in a transmission electron microscope were used to examine the structure of the materials synthesized in this chapter and to determine the W distribution inside materials. Electrochemical measurements made with coin cells verified that excellent charge-discharge capacity retention of materials synthesized with 1mol% W.

This Chapter is based on an article published in Advanced Energy Materials.[15] [Chenxi Geng et al Adv. Energy Mater. 12 (2022) 2103067]. Reprinted with permission from Advance Energy Materials. [15] Copyright 2020 John Wiley and Sons. Chenxi Geng contributed to the conceptualization, material synthesis, material characterizations, and electrochemical tests; Divya Rathore, and Ines Hamam contributed to the conceptualization, material synthesis and material characterization; Dylan Heino, Ning

Zhang, Nafiseh Zaker, Gianluigi A. Botton, Roee Omessi, Nutthaphon Phattharasupakun, and Toby Bond contributed to the material characterizations. Jeff Dahn contributed to the design of experiments, the interpretation of results as well as editing the manuscript.

5.1 **Experimental Methods**

A dry particle fusion method described carefully in Chapter 3 was used for this chapter. Briefly, nanometer-sized Tungsten (VI) oxide (WO_3) powder (< 100 nm, from Sigma-Aldrich) was coated on $Ni(OH)_2$ (15 micron diameter, from Zoomwe, China) by dry particle fusion to make $(Ni(OH)_2)_{1-x} \cdot (WO_3)_x$ precursors (x=0, 0.005, 0.01, 0.02 and 0.04). Material loading weight, spinning speed and duration are shown in Table 5.1.

Table 5.1. Summary of the precursors made by dry particle fusion and subsequent heat treatment in this chapter.

Description	$Ni(OH)_2$ weight (g)	WO_3 weight (g)	Spinning speed (rpm)	Duration (min.)
$Ni(OH)_2$	50.0	0	0	0
$(Ni(OH)_2)_{0.995} \cdot (WO_3)_{0.005}$	50.0	0.628	2400	60
$(Ni(OH)_2)_{0.99} \cdot (WO_3)_{0.01}$	50.0	1.263	2400	60
$(Ni(OH)_2)_{0.98} \cdot (WO_3)_{0.02}$	50.0	2.552	2400	60
$(Ni(OH)_2)_{0.96} \cdot (WO_3)_{0.04}$	50.0	5.210	2400	60

The lithiation process was carried out as described in Chapter 2. The second step lithiation temperature for lithiated W-added LNOs with different W mole ratios in this

chapter was 800°C.   In order to get the optimum calcination temperature for W1-LNO,

powders were also heated at 700°C, 750°C, 850°C and 900°C at the second lithiation step.

In order to see if the location of W in LNO would be influenced by the way that W was

added, the precursor $(Ni(OH)_2)_{0.98} \cdot (NiWO_4)_{0.01}$, which has a W/(Ni+W) molar ratio of

0.01, was made by coprecipitation in a continuously stirred tank reactor (CSTR)

(Brunswick Scientific/Eppendorf BioFlo 310) using a method similar to that described by

Van Bommel et al.[71] and in Chapter 2.   The second step lithiation temperature for this

lithiated W1-LNO made by coprecipitation was 800°C.

SEM, XRD, TEM, EELS, MILLS, XANES, EXAFS, lithiation process and coin cell

long-term cycling were performed as described in Chapter 2.   Electrolyte with 1.2 M

$LiPF_6$ in FEC:DMC (1:4 v/v) was used for the half coin cell long-term cycling tests as

this electrolyte gives better long-term lithium metal cycling.

5.2 Results and Discussion

X-ray diffraction patterns were collected from 15º to 70º for the materials heated with

$LiOH \cdot H_2O$ and all the materials demonstrated a well-developed layered structure as

shown in Figure 5.1A.   The peak-height normalized (003) peak broadened with

increasing amounts of W as shown clearly in Figure 5.1B. It is known that the full width

at a half maximum (FWHM) of the XRD peak is inversely proportional to the crystallite

grain size[111,112], so the peak broadening indicates decreasing crystallite grain size with

increasing W content. The (003) peak broadening could also be attributed to the increased micro strain in lattice due to Ni-Li mixing[113]. More importantly, there was an amorphous hump which appears near the (003) peak and which increases in intensity with increasing amounts of W, while an impurity peak appeared at 24º and also became more intense as the W fraction increased (Figure 5.1C). The amorphous hump and impurity peak, which do not originate from the layered structure, raised the question whether the added W atoms were incorporated into the layered structure or stayed outside the grains of primary particles as a secondary phase.
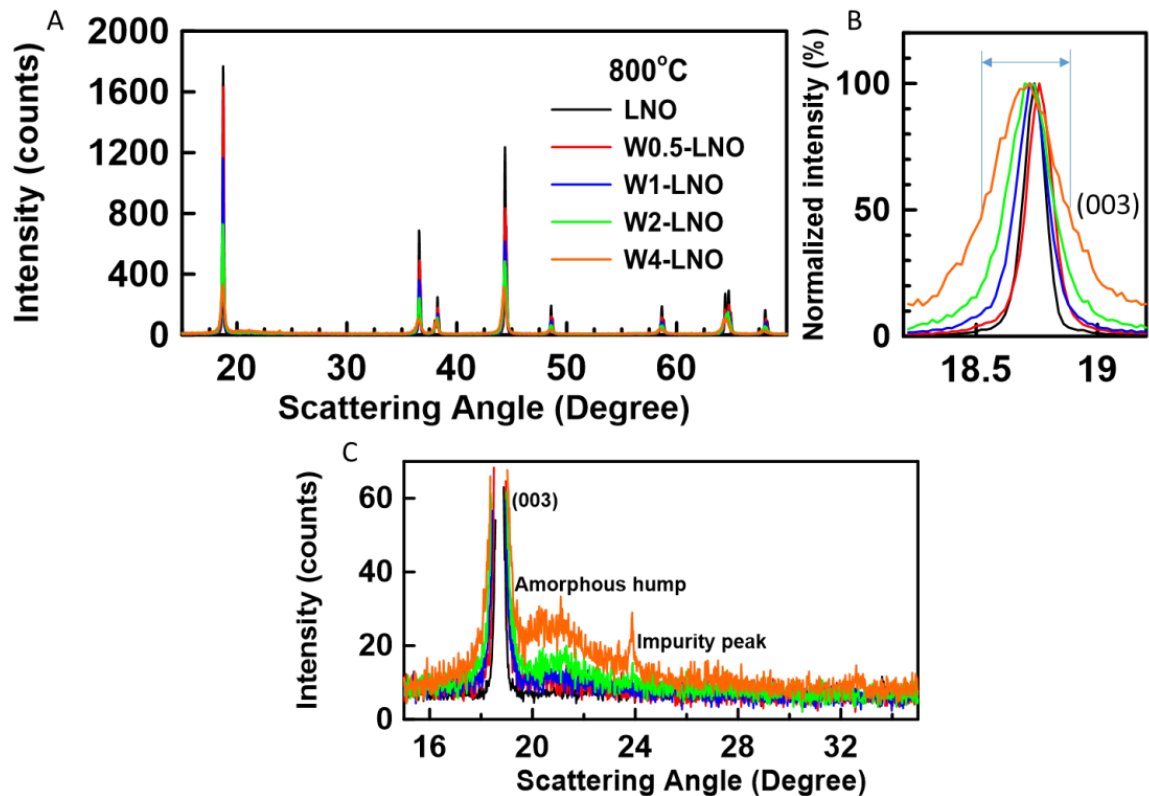
Figure 5.1. (A) XRD patterns of LNO, W0.5-LNO, W1-LNO, W2-LNO and W4-LNO synthesized at 800°C; (B) Broadening of the peak-height normalized (003) peak; (C) Expanded view of the impurity region.

Rietveld refinements were performed assuming an α-NaFeO$_2$ (space group R$\bar{3}$m) hexagonal layered structure in which Li occupies the 3a site, transition metals occupy the 3b site, and oxygen occupies the 6c site. The refinement results are shown in Table 5.2. There is an increase of Ni atoms in the Li layer (%Ni$_{Li}$) with increasing W fraction, from 2.8% in LNO to 8.8% in W4-LNO, while the lattice parameters a and c also increase as the W fraction increases. One might argue that W^{6+} gets doped into the transition metal layer, and therefore more Ni^{3+} was reduced to Ni^{2+} to maintain charge neutrality. Ni^{2+}

112

has a similar ionic radius (r_{Ni2+}=0.69 Å, r_{Ni3+}=0.56 Å) to Li^+ (r_{Li+}=0.76 Å)[114], which facilitates Ni and Li mixing and results in the higher %Ni_{Li} with higher fraction of W[52]. However, our DFT calculation[115] show that it is not preferable for W to be incorporated in the layered phase lattice. Instead, we believe that W is incorporated in $Li_xW_yO_z$ (x/y > 1) phases in the grain boundaries between primary particles, which takes more Li from $LiNiO_2$ making it lithium deficient and thus having a higher %Ni_{Li} and increased lattice constants.

Table 5.2 Rietveld refinement results of LNO, W0.5-LNO, W1-LNO, W2-LNO, W4-LNO and W4-LNO with extra Li added. All samples were heated to 800°C in oxygen.

Heated at 800°C	a (Å) (within ±0.0001 Å)	c (Å) (within ±0.001 Å)	Ni in Li layer % (within ±0.2 %)
LNO	2.8775	14.1901	2.808
W0.5-LNO	2.8781	14.2041	2.626
W1-LNO	2.8783	14.2038	2.412
W2-LNO	2.8804	14.2061	4.255
Heated at 800°C	a (Å) (within ±0.0001 Å)	c (Å) (within ±0.001 Å)	Ni in Li layer % (within ±0.3 %)
W4-LNO	2.8876	14.2175	8.861
W4-LNO extra Li added	2.8796	14.2043	4.310

To further investigate the amorphous hump and impurity peak, we made W4-LNO with extra Li added, which corresponds to Li/(Ni+W) = 1.06 (our normal W4-LNO sample has a Li/(Ni+W) ratio of 1.02). W4-LNO also had a well-developed layered structure as shown in Figure 5.2A. The amorphous hump became less pronounced, and a new phase appeared representing Li_6WO_6 (PDF# 21-0532, Figure 5.2B). The appearance of the Li_6WO_6 phase confirmed that there is a $Li_xW_yO_z$ phase staying outside of layered phase. The Rietveld refinement result is also shown in Table 5.2. The percentage of Ni in the Li layer decreased to 4.3% when a Li:(Ni+W) ratio of 1.06 was used compared to 8.8% when a Li:(Ni+W) ratio of 1.02 was used. This suggests that the Li_6WO_6 phase consumed a large amount of Li resulting in insufficient Li for stoichiometric $LiNiO_2$ and causing lithium deficiency as in $Li_{1-x}Ni_{1+x}O_2$. Then some Ni^{3+} transforms to Ni^{2+} to

maintain electroneutrality, and some of this Ni^{2+} then moves to the Li layer, thus the percentage of Ni in the Li layer increased. When extra Li was added, to compensate for that lost in the $Li_xW_yO_z$ phase, the Li deficiency in $Li_{1-x}Ni_{1+x}O_2$ decreased.
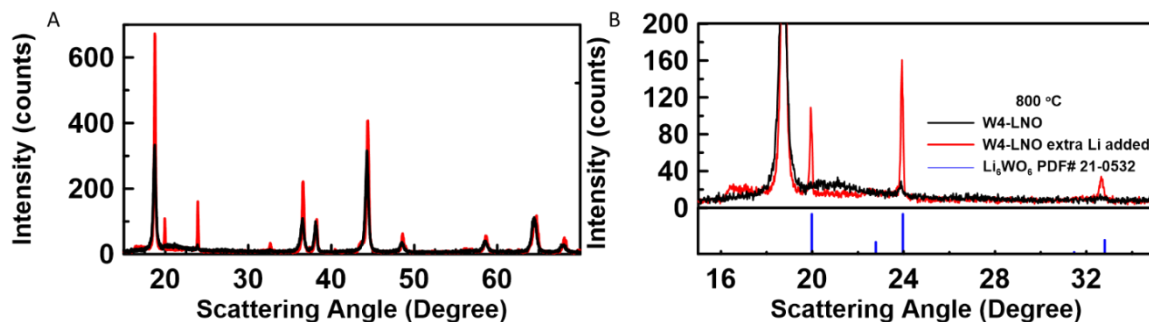
Figure 5.2. (A) XRD patterns of W4-LNO and W4-LNO with extra Li added during synthesis; (B) Expanded view of the impurity region.

Figures 5.3A and B show the W L3-edge X-ray absorption near edge structure (XANES) spectra and Fourier-transformed extended X-ray absorption fine structure (EXAFS) spectra of W1-LNO and a home-made Li_4WO_5 reference. Both the W L3-edge XANES spectra and Fourier-transformed EXAFS spectra of W1-LNO are identical to the spectra of the homemade Li_4WO_5 reference, which implies again that W is possibly incorporated in a $Li_xW_yO_z$ phase. It is important to note that both Ni in LNO and W in Li_4WO_5 and Li_6WO_6 occupy octahedral sites, which also could result in the overlap of XANES and EXAFS spectra of W1-LNO and Li_4WO_5. Therefore, more characterization is required for the study the distribution of W. EELS mapping result will be shown in the following paragraph. The XRD pattern of home-made Li_4WO_5 in Figure 5.3C shows it contains

both Li_4WO_5 and Li_6WO_6. This provides an explanation why the impurity phase in "W4-LNO extra Li added" is Li_6WO_6 (more excess lithium) while the W L3-edge EXAFS spectra of W1-LNO and Li_4WO_5 are identical.   The local structures containing the first and second neighbors of W in Li_4WO_5 (Figure 5.3D) and Li_6WO_6 (Figure 5.3E) are quite similar, which can explain why the W1-LNO and homemade Li_4WO_5 materials have similar W L3 edge peak positions in XANES and in Fourier-transformed EXAFS spectra.
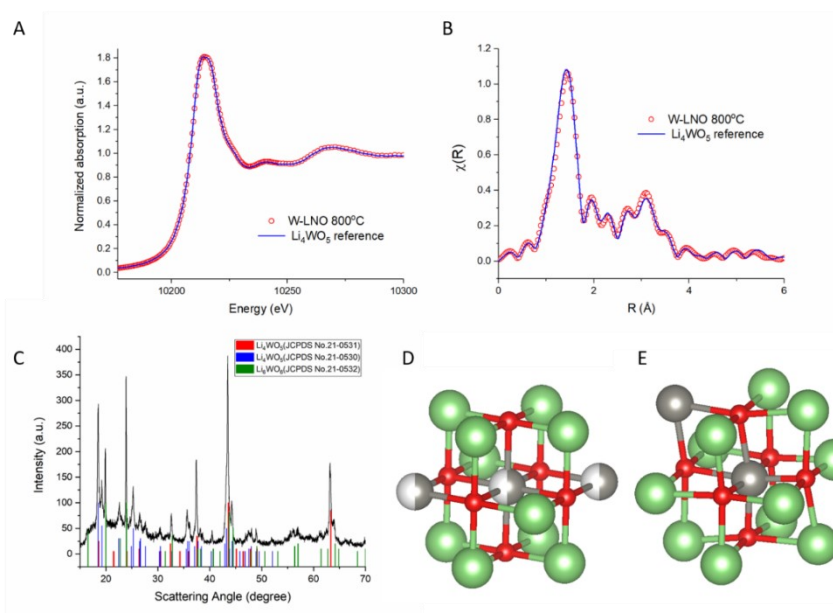
Figure 5.3 (A) W L3-edge X-ray absorption near edge structure (XANES) spectra and (B) Fourier-transformed extended X-ray absorption fine structure (EXAFS) spectra of W1-LNO and a home-made Li_4WO_5 reference. (C) XRD of the home-made Li_4WO_5 reference sample in which both Li_4WO_5 and Li_6WO_6 phases were identified. (D-E) Local structures (first and second neighbors) of W in (D) Li_4WO_5 and (E) Li_6WO_6 phases, respectively.

Figure 5.4 shows the discharge specific capacity versus cycle number for W4-LNO and "W4-LNO extra Li added". Adding extra Li during heat treatment greatly increased the specific capacity of W4-LNO from 133.5 mAh/g to 193.9 mAh/g, further supporting our speculation that the $Li_xW_yO_z$ phase formed and consumes lithium hence causing Li deficiency in $Li_{1-x}Ni_{1+x}O_2$.
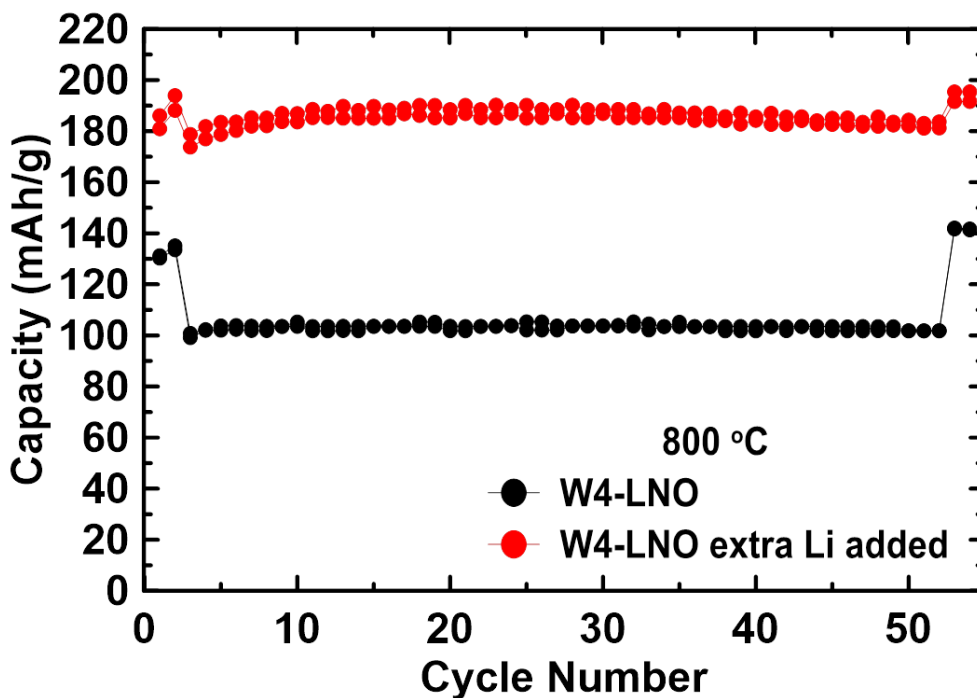
Figure 5.4. Electrochemical cycling performance of W4-LNO and "W4-LNO extra Li added" synthesized at 800°C (2 cycles at C/20, 50 cycles at C/5, and 2 cycles at C/20).

To clearly determine the location of W in the LNO samples, electron energy loss spectroscopy (EELS), performed in a transmission electron microscope (TEM), was carried out on a cross section of the W1-LNO sample. The STEM image of W1-LNO

and the EELS mapping of W in Figure 5.5A show that W is mostly concentrated in the grain boundaries between primary particles and on the surface of the secondary particles instead of being incorporated within the grains. Analyzing O-K edge EELS near-edge structure features, it is found that the oxygen K-edge spectrum in the grain boundaries and on the surface of the secondary particles (Figure 5.6A) does not have a pre-edge while oxygen K-edge spectrum within the grains has a pre-edge feature (Figure 5.6B). Therefore, it is possible to conclude that the chemical environment/coordination of the oxygen atoms within the grains and the grain boundaries is different. Multiple linear least squares (MILLS) fitting maps with the internal references (using spectra at grain boundaries and spectra within the grains) show that oxygen atoms without a pre-edge are present on all grain boundaries while oxygen with a pre-edge are present inside grains. There is strong correlation between the near edge structure of the oxygen spectra at the grain boundaries and the EELS maps of W, which infers that the phases having a different oxygen chemical environment are W phases.

To determine if the W location would be influenced by the way that W was added, EELS was also carried out on W1-LNO in which W was added by coprecipitation at the precursor synthesis stage (the only sample made by coprecipitation in this chapter). In the coprecipitated precursor it is possible that W was uniformly distributed inside the precursor, not only on the surface of the precursor like the WO_3-coated $Ni(OH)_2$ prepared by dry particle fusion. EELS mapping of W in Figure 5.5B shows that W was also

mostly concentrated in the grain boundaries along with the surface and not significantly

distributed into primary particles of W1-LNO where the precursor was made by

coprecipitation. This means that even if W was uniformly incorporated throughout the

coprecipitated precursor, it is expelled into the grain boundaries during heat treatment

with LiOH·H$_2$O.
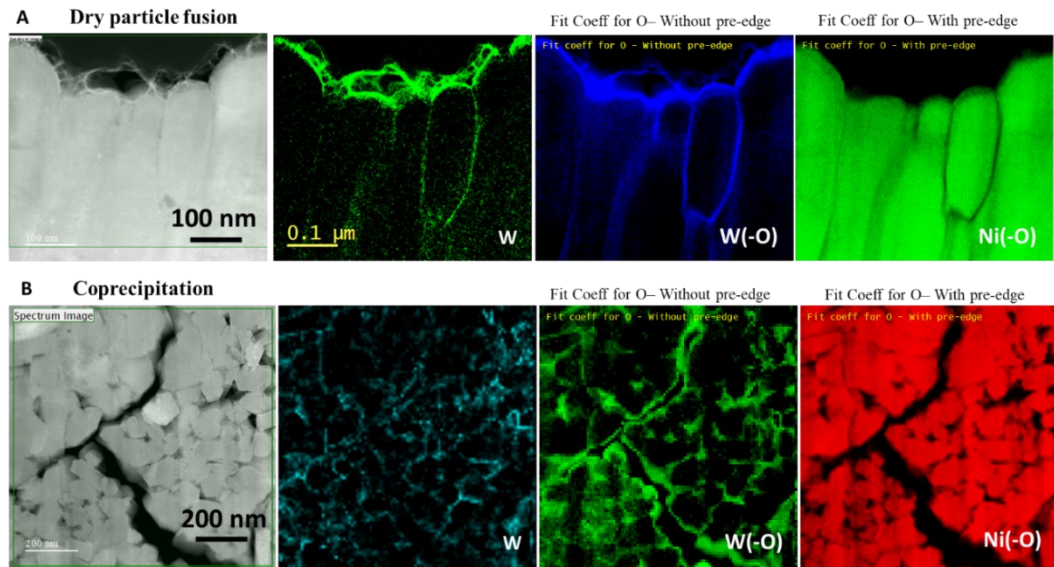
Figure 5.5. TEM image, EELS mapping of tungsten signal, MLLS fitting of oxygen without pre-edge spectra, MLLS fitting of oxygen with pre-edge spectra of (A) W1-LNO sample where the precursor was coated with WO$_3$ by dry particle fusion and (B) W1-LNO sample where the precursor was made by coprecipitation after cycling. The scale bar corresponding to each panel is shown in the left most panel.
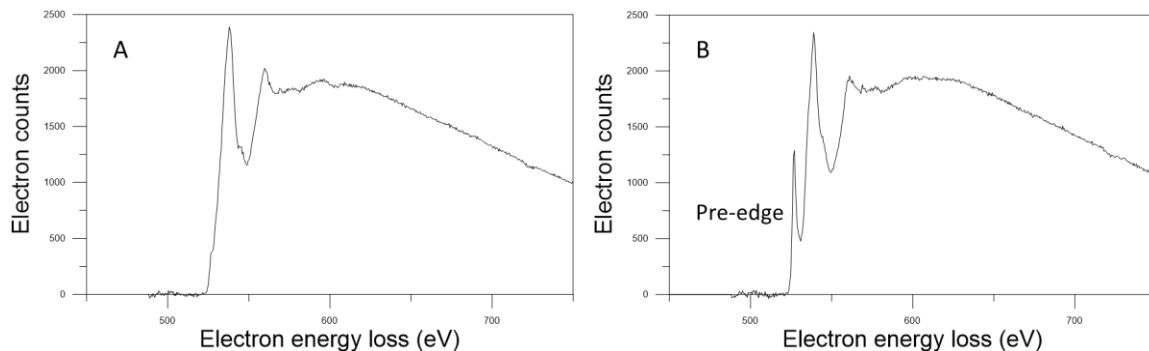
Figure 5.6. (A) EELS spectrum at the Oxygen K-edge obtained at grain boundaries where W is detected from the EELS maps; (B) EELS spectrum of O K-edge within the grains of LiNiO2. The spectra show differences in the oxygen bonding/coordination in the two different regions.

The scanning electron microscopy (SEM) images in Figure 5.7A show that the primary particles of LNO were relatively large and that the primary particles become smaller after adding W. ImageJ[116,117] was used to obtain the average primary particle area, and Figure 5.7C shows the average primary particle radius plotted versus the W-content calculated assuming the primary particle cross sections are circular.   Figure 5.7C shows quantitatively the same trend as the images in Figure 5.7A. To observe how temperature would influence particle growth, we synthesized LNO and W1-LNO at 700ºC, 750ºC, 800ºC and 900ºC. SEM images were taken to observe the primary particle growth versus temperature (Figure 5.7B) and ImageJ was used to quantify the primary particle radius of materials synthesized at different temperatures (Figure 5.7D). LNO has relatively large primary particles at 700ºC initially, and the primary particles grow larger with

temperature, becoming much larger at 900ºC, while adding W effectively suppressed primary particle growth. Primary particles of W1-LNO at 700ºC were small and remained small even though the synthesis temperature increased to 900ºC. SEM images (Figure 5.8) at lower magnifications showing morphologies of singular and multiple particles of the above-mentioned materials are included in supporting information. In our opinion, the surface nano-WO_3 on $Ni(OH)_2$ should react with LiOH or Li_2O to form $Li_xW_yO_z$ phases, which normally have melting points in the temperature range of 700-750ºC[118]. Many Li-W-O phases were reported, such as Li_2WO_4 (melting point [m.p.] 745ºC), $Li_2W_2O_7$ (m.p. 735ºC), $Li_2W_4O_{12}$,[119] $Li_2W_4O_{13}$ (m.p. 805ºC, 800ºC, or 750ºC),[118] and $Li_2W_5O_{15}$.[120] As a result, these $Li_xW_yO_z$ phases can easily wet the surfaces of the secondary grains during synthesis and then infuse along all the grain boundaries between the primary particles. We infer that it is primarily the $Li_xW_yO_z$ phase which wets the surfaces of the primary particle grains that behaves like a barrier to slow down Ni interdiffusion and therefore hinders the growth of the primary grains as temperature increases. Given the lack of detectable W substituting for Ni in LNO, we expect that W within the LNO lattice, if any, would not have a significant effect suppressing grain growth.
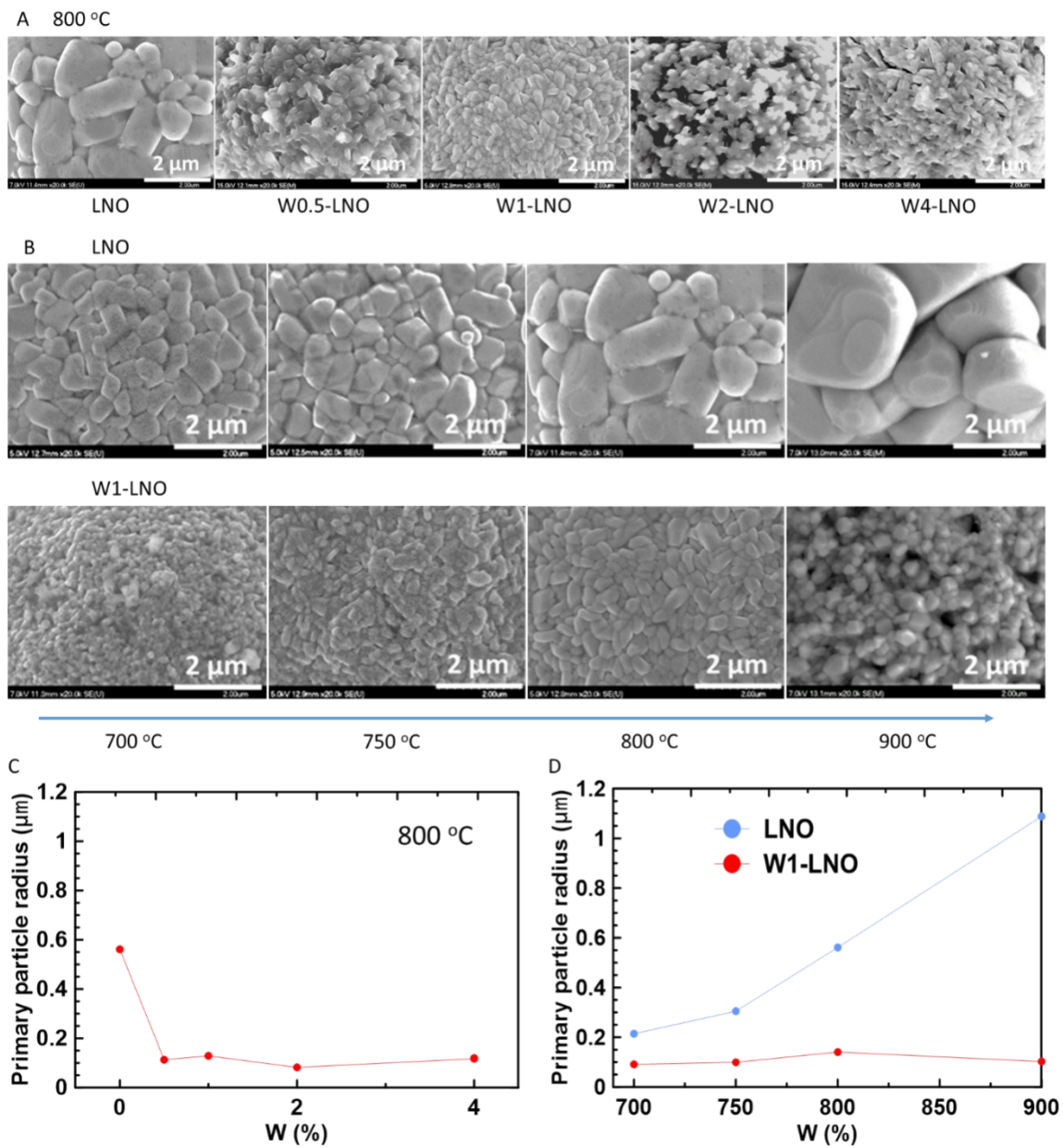
Figure 5.7. (A) SEM images of LNO, W0.5-LNO, W1-LNO, W2-LNO and W4-LNO synthesized at 800ºC; (B) SEM images of LNO and W1-LNO synthesized at 700ºC, 750ºC, 800 ºC and 900 ºC; (C) average primary particle radii of samples mentioned in (A); (D) average primary particle radii of samples mentioned in (B).
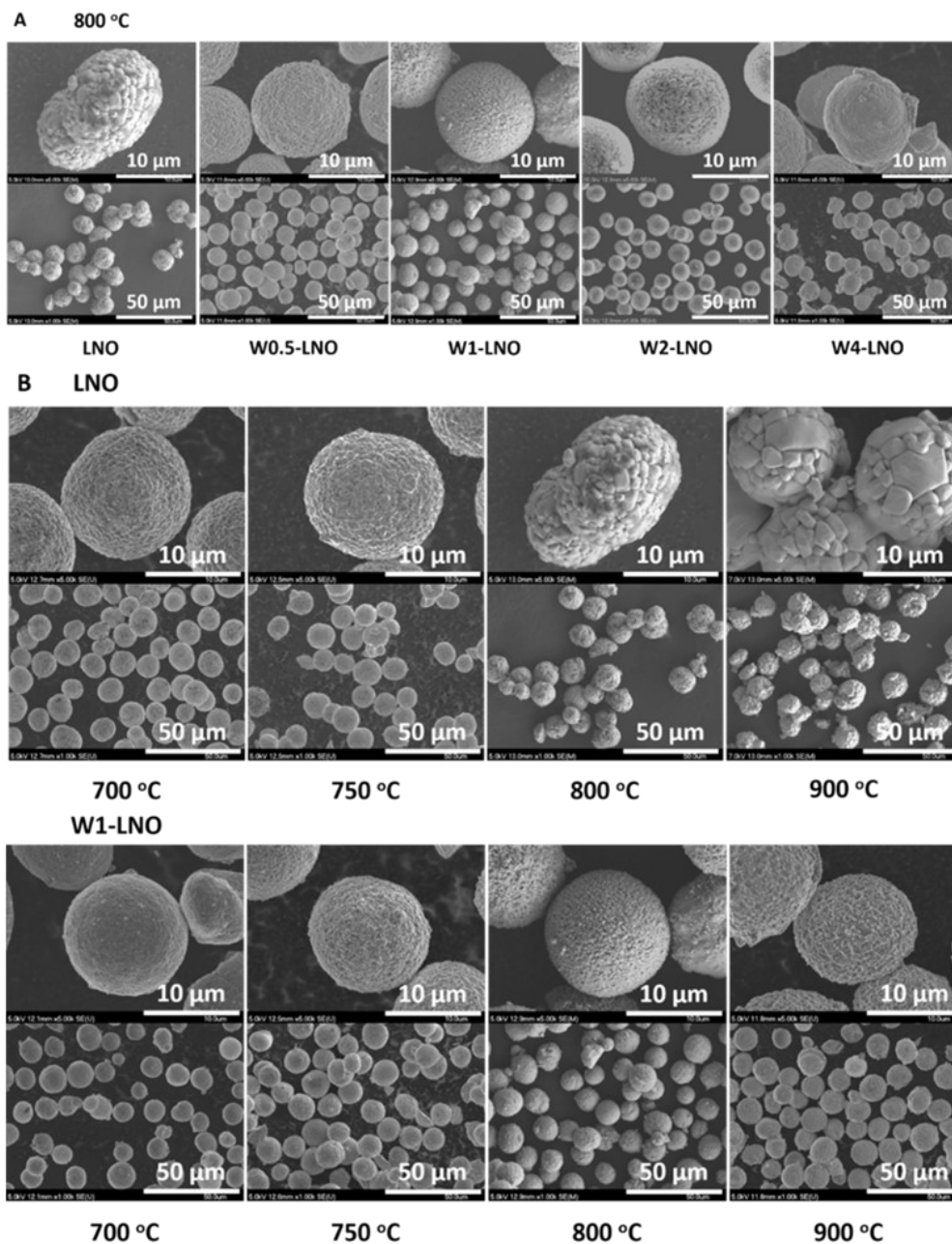
Figure 5.8. (A) SEM images at low magnifications (×5000 and ×1000) of LNO, W0.5-LNO, W1-LNO, W2-LNO and W4-LNO synthesized at 800ºC; (B) SEM images at low magnifications (×5000 and ×1000) of LNO and W1-LNO synthesized at 700ºC, 750ºC, 800 ºC and 900 ºC.

Figure 5.9A shows the discharge specific capacity versus cycle number for samples described above. Adding only 0.5mol% W greatly improved the specific capacity and capacity retention. and W1-LNO showed the best performance with both best specific capacity and best capacity retention. The peak below 3.6 V shown in the differential capacity curve (dQ/dV) in Figure 5.9B is normally referred as being in the kinetic hindrance (KH) region[37] and the peak intensity is very sensitive to the fraction of Ni atoms in the Li layer[121]. Therefore, the larger KH peak of W0.5-LNO and W1-LNO agrees with the refinements for %Ni_{Li} shown in Table 5.2. The intensity of the H3→H2 peak[37] in the dQ/dV vs V curve near 4.2 V drops with higher W fraction, suggesting the suppression of the H3→H2 phase transition[37,49], which agrees with a literature report[52]. The suppression is caused by the increased fraction of Ni atoms in the Li layer in the samples having more W [122,123].

Figure 5.9C shows the specific capacity versus cycle number of W1-LNO synthesized at 700°C, 750°C, 800°C and 850°C. W1-LNO made at 750°C and 800°C have almost overlapping data and behaved better than W1-LNO made at other temperatures. Figure 5.10 shows the XRD patterns of the above-mentioned materials with well-developed layered structure, and the XRD refinement data are included in Table 5.3. Figure 5.9D compares the dQ/dV vs. V curves of the 2nd, 54th and the 106th cycle of W1-LNO made at 800°C. There was a capacity recovery in the KH region and the H3→H2 peak

maintained its peak intensity and shape, indicating minimal degradation and good capacity retention of the material.
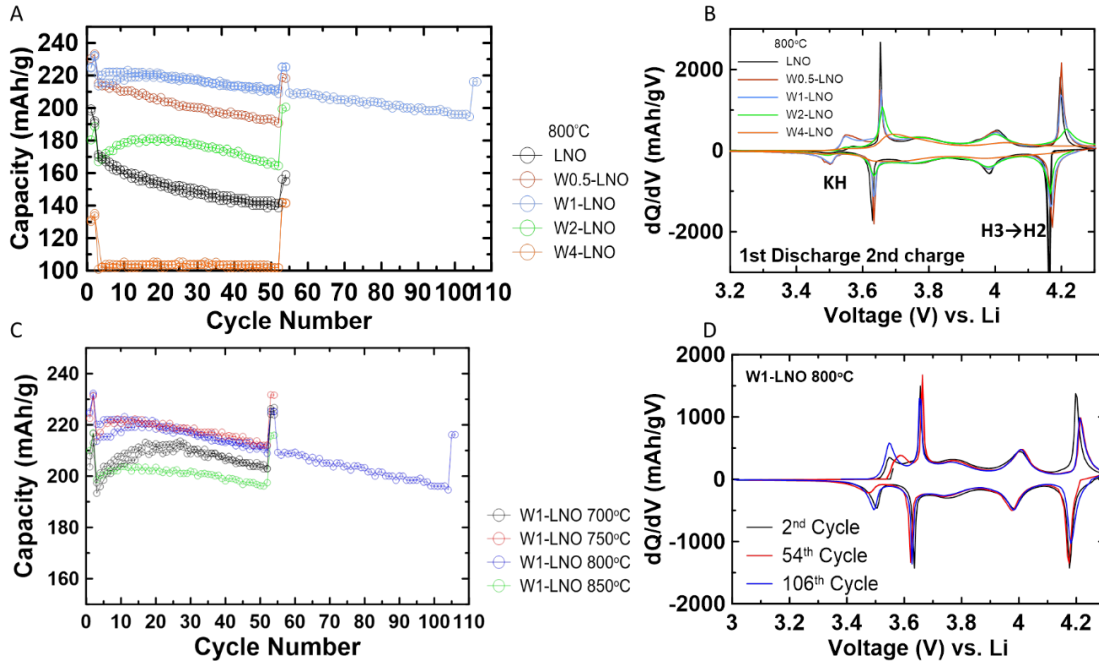
Figure 5.9. (A) Electrochemical cycling performance of LNO, W0.5-LNO, W1-LNO, W2-LNO and W4-LNO synthesized at 800ºC (2 cycles at C/20, 50 cycles at C/5, and 2 cycles at C/20); (B) dQ/dV vs. V curves of 1st discharge and 2nd charge process; (C) Electrochemical cycling performance of W1-LNO synthesized at 700ºC, 750ºC, 800ºC and 850ºC; (D) Comparison of 2nd cycle and the 54th cycle dQ/dV vs. V curves of W1-LNO synthesized at 750ºC.
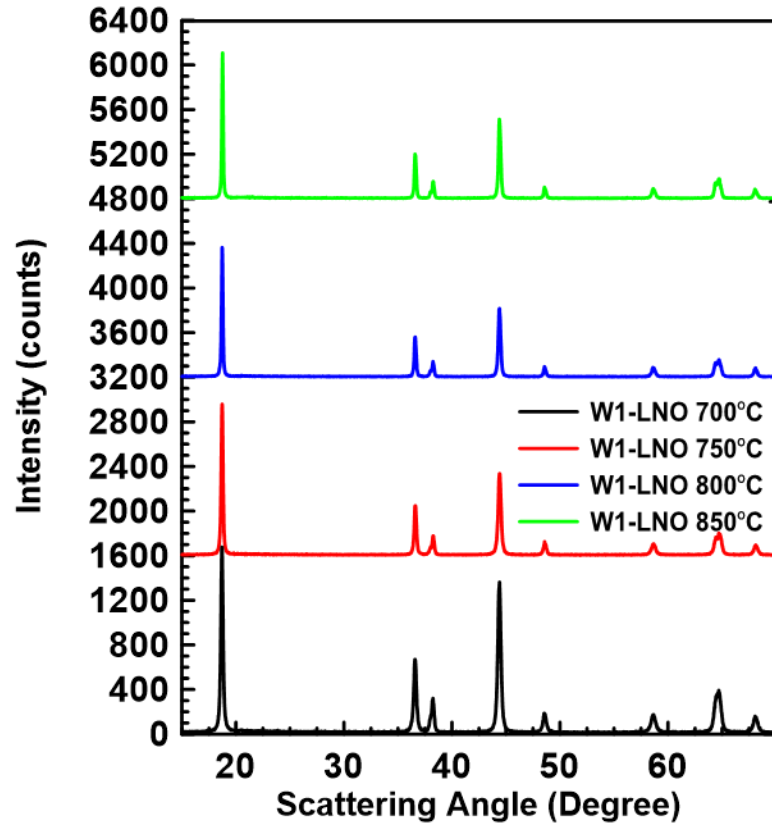
Figure 5.10. XRD patterns of W1-LNO synthesized at 700ºC, 750ºC, 800ºC and 850ºC.

Table 5.3. Rietveld refinement results for W1-LNO synthesized at 700ºC, 750ºC, 800ºC and 850ºC.

Heated at 800ºC	a (Å) (within ±0.0001 Å)	c (Å) (within ±0.001 Å)	Ni in Li layer % (within ±0.1 %)
W1-LNO 700 ºC	2.8776	14.1983	4.414
W1-LNO 750 ºC	2.8763	14.2006	1.736
W1-LNO 800 ºC	2.8783	14.2038	2.412
W1-LNO 850 ºC	2.8798	14.2058	3.046

We studied the propensity of various Ni-rich positive electrode materials to resist microcracking under the application of uniaxial pressure.[17] That work showed that the stronger polycrystals can maintain their secondary particle integrity under high stress and avoid microcracking during charge-discharge cycling. Crushing tests applying a pressure from zero up to 500 MPa using an Instron universal testing machine and an appropriate die were performed on LNO synthesized at 800ºC and W1-LNO synthesized at 750ºC. Data collected are shown in Figure 5.11A. The compression work measures the resistance of a material to be crushed which increases from 7.7 J/g for LNO to 15.1 J/g for W1-LNO, indicating that W1-LNO has greatly increased resistance to fracture. As shown in Figure 5.11B and C, LNO heavily fractured after the crushing test to a pressure of 500 MPa, while only a few particles of W1-LNO cracked after crushing, which clearly shows W1-LNO is more resistant to fracture. It is the infusion of the amorphous

$Li_xW_yO_z$ phases between the grain boundaries which coats the particle surface, hinders grain growth, improves secondary particle robustness, thus improves material cycling performance.
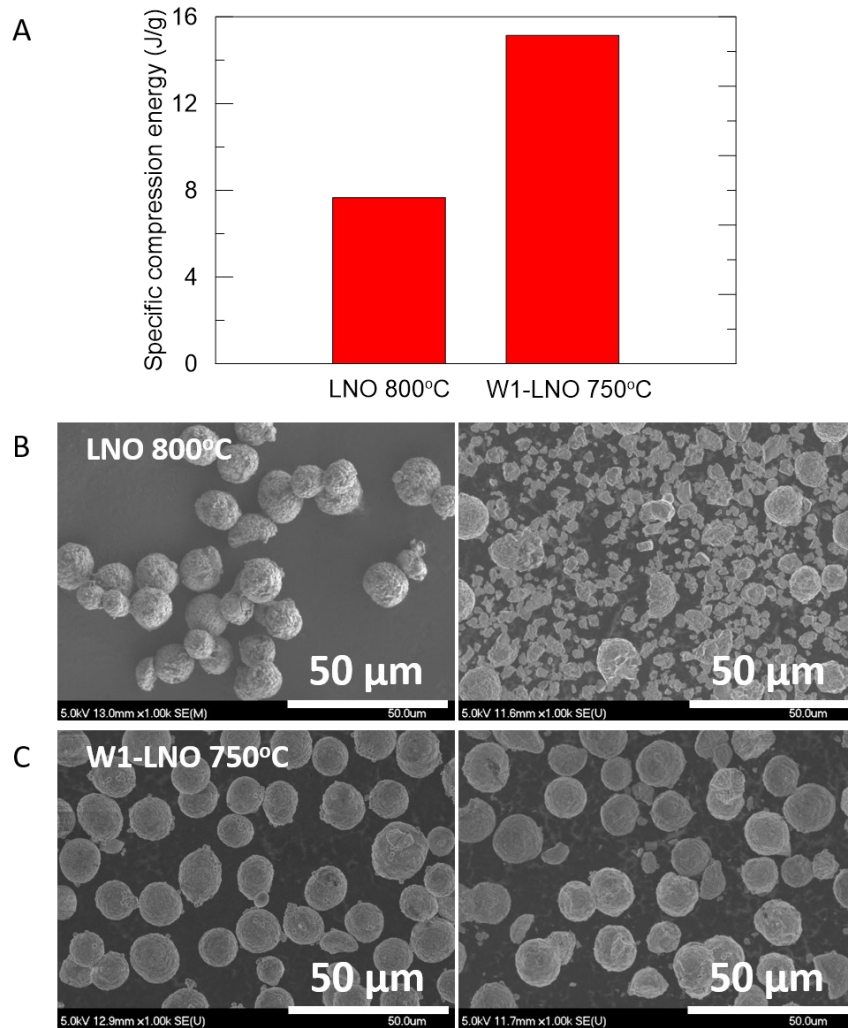
Figure 5.11 (A) Analysis of compression work by the crushing test using the Instron system (see reference [17]). The specific compression energy (J/g) of LNO synthesized at 800°C and W1-LNO synthesized at 750°C are shown; (B) SEM images of LNO 800°C and (C) W1-LNO 750°C before and after the crushing test.

5.3 Summary

This chapter clearly shows that W is not incorporated substitutionally for Ni or Li when incorporated as a dopant in LNO. Instead, XRD and EELS have conclusively shown that W is present in amorphous $Li_xW_yO_z$ phases that coat the surfaces of the secondary particles and all the grain boundaries of the primary particles. Given that the WO_3 was only coated on the surfaces of the $Ni(OH)_2$ precursor in the samples made by mechanofusion, finding W deep within the secondary particles means that the $Li_xW_yO_z$ phases wet the LNO surfaces well. This provides a coating on the primary and secondary particles which may aid in capacity retention. Additionally, the $Li_xW_yO_z$ phases hinder primary particle growth as temperature increases and appear to act as a "glue" to increase the resistance of the secondary particles to microcracking under applied stress and during charge-discharge cycling.

It is our hope that this chapter will aid in the understanding and commercialization of Ni-rich positive electrode materials for Li-ion cells.

Chapter 6 Impact of Tantalum Added to Ni-based Positive Electrode Materials for Lithium-ion Batteries

The addition of high valence elements like tungsten (W) and tantalum (Ta) have been reported to be particularly effective to improve the charge-discharge capacity retention of Ni-rich materials.[8–16,18] We reported that the addition of W into layered oxides has improved the charge-discharge capacity retention of cells made with W-containing materials and improved the mechanical strength of the cathode particles as measured by a crush test.[18] Electron energy loss spectroscopy (EELS) has shown that W was concentrated inside grain boundaries between primary particles as $Li_xW_yO_z$ phases. The $Li_xW_yO_z$ phases behave like a barrier to slow down ion diffusion during calcination which reduced the size of the primary particles in W-containing materials compared to materials without W. The smaller primary particles underwent smaller absolute volume expansion and shrinkage of primary particles which reduced the occurrence of microcracking in the electrode particles and improved capacity retention of the cathode materials. The $Li_xW_yO_z$ phases also acted as a "glue" to bind the primary particles together and keep them in contact during cycling.

$Li_xTa_yO_z$ phases have been reported to exist[124–126] and Ta_2O_5-Li_2O phase diagram has been investigated[127]. We expect that tantalum plays the same role as tungsten when added to $LiNiO_2$ in small amounts, suggesting that tantalum does not incorporate into the

crystal structure of $LiNiO_2$, but appears as $Li_xTa_yO_z$ phases within the grain boundaries instead.

In this chapter, we synthesized $LiNiO_2$ with 0, 0.5, 0.75, 1, and 2 mol % of added Ta lithiated at temperatures under 730°C, which will be denoted as LNO, Ta0.5-LNO, Ta0.75-LNO. Ta1-LNO, and Ta2-LNO. X-ray diffraction (XRD), scanning electron microscopy (SEM), Extended X-ray absorption fine structure (EXAFS) and long-term cycling tests were used to examine the physical and electrochemical properties of the above synthesized materials. These results were compared with $LiNiO_2$ synthesized with 1 or 2 mol% tungsten (W) denoted as W1-LNO and W2-LNO. These samples were heated with LiOH at 800°C.

This chapter was published by Journal of Power Sources.[127] Chenxi Geng contributed to the conceptualization, material synthesis, material characterizations, and electrochemical tests; Dylan Heino contributed to material synthesis, material characterizations, and electrochemical tests; Divya Rathore, Nafiseh Zaker and Nutthaphon Phattharasupakun contributed to the material charaterizations. Jeff Dahn contributed to the design of experiments, the interpretation of results and the editing of the manuscript.

6.1 Experimental Methods

A dry particle fusion method described carefully in chapter 3 was used for this chapter. Briefly, nanometer-sized Ta_2O_5 powder (< 100 nm, from Sigma-Aldrich) was coated on $Ni(OH)_2$ (15 micron diameter, from Zoomwe, China) by dry particle fusion to make

$(Ni(OH)_2)_{1-x} \cdot (Ta_2O_5)_x$ precursors (moles Ta/(moles Ni + moles Ta)=0, 0.005, 0.0075, 0.01, 0.02). Material loading weight, dry particle fusion spinning speed and duration are shown in Table 6.1.

Table 6.1. Summary of the precursors made by dry particle fusion in this chapter.

Description	Mole ratio of Ta (moles Ta/(moles Ni + moles Ta)	$Ni(OH)_2$ weight (g)	Ta_2O_5 weight (g)	Spinning speed (rpm)	Duration (min.)
$Ni(OH)_2$	0	50.0	0	0	0
$(Ni(OH)_2)_{0.995} \cdot (Ta_2O_5)_{0.0025}$	0.005	49.41	0.592	2400	60
$(Ni(OH)_2)_{0.9925} \cdot (Ta_2O_5)_{0.00375}$	0.0075	49.12	0.885	2400	60
$(Ni(OH)_2)_{0.99} \cdot (Ta_2O_5)_{0.005}$	0.01	48.82	1.175	2400	60
$(Ni(OH)_2)_{0.98} \cdot (Ta_2O_5)_{0.01}$	0.02	47.68	2.319	2400	60

The lithiation process was carried out as described in Chapter 2. The second step lithiation temperature for all the lithiated samples in this chapter was 730°C.

SEM, XRD, TEM, EXAFS, lithiation process and coin cell long-term cycling were performed as described in Chapter 2. Electrolyte with 1.2 M $LiPF_6$ in FEC:DMC (1:4 v/v) was used for the half coin cell long-term cycling tests as this electrolyte gives better long-term lithium metal cycling.

6.2 Results and Discussion

X-ray diffraction patterns were collected from 15º to 70º for the materials heated with LiOH·H$_2$O and all the materials demonstrated a well-developed layered structure as shown in Figure 6.1A. Figure 6.1B shows the expanded view of (018)/(110) peak. The clear splitting of the (018)/(110) peak indicates a well-developed crystallinity for LNO. After adding Ta, the splitting becomes less noticeable due to increased peak width and changed lattice constants. The increased peak width can be caused by a decrease in the size of the primary particles as will be evident in the SEM results in Figure 6.2. In the case of W-containing LNO, it has been shown that the presence of Li$_x$W$_y$O$_z$ phases in the grain boundaries limits the growth of the LNO primary particles and we believe Li$_x$Ta$_y$O$_z$ phases play the same role here[15,16]. The presence of amorphous Li$_x$Ta$_y$O$_z$ phases can be detected by the broad "hump" in the XRD pattern near 20-22 degrees as shown in Figure 6.1D which increases in size as the Ta content increases.

The intensity ratio of the (104) and (003) peaks in Figure 6.1C increases with the amount of Ta in the samples, which corresponds to the increasing Li/Ni mixing ratio of the samples according to the Rietveld refinement. Rietveld refinements were performed assuming an α-NaFeO$_2$ (space group R$\overline{3}$m) hexagonal layered structure in which Li occupies the 3a site, transition metals occupy the 3b site, and oxygen occupies the 6c site. The refinement results are shown in Table 6.2, which demonstrate that the Li/Ni mixing ratio increases with an increasing amount of Ta. This is caused by the fact that we did

not increase the amount of Li (Li/(Ni+Ta) = 1.02) in the samples as the Ta content increased. Thus, the $Li_xTa_yO_z$ phases "steal" some Li from the $LiNiO_2$ phase, leaving less Li than desired and creating Li deficient $Li_{1-x}Ni_{1+x}O_2$ materials[44] which inherently contain some Ni in the Li layer. The (003) peak broadened with increasing amounts of Ta as shown clearly in Figure 6.1C. The full width at a half maximum (FWHM) of a XRD peak is inversely proportional to the crystallite grain size[111,112], so the peak broadening indicates decreasing crystallite grain size with increasing Ta content. The broad "hump" in the XRD pattern near 20-22 degrees, the increasing Li/Ni mixing ratio and the smaller primary particles with increasing amounts of Ta amount follow the same trend as W-containing LNO. These observations suggest that Ta remains as amorphous $Li_xTa_yO_z$ phases in the grain boundaries instead of being incorporated into the LNO crystal structure. Recently Park et al. reported that Ta is also mainly aggregated in the grain boundaries as a second phase rather than doping into the primary particles in Ni-rich layered oxides, supporting our results. Readers can refer to the TEM results in their work that clearly show that Ta is aggregated in the grain boundaries.[128]
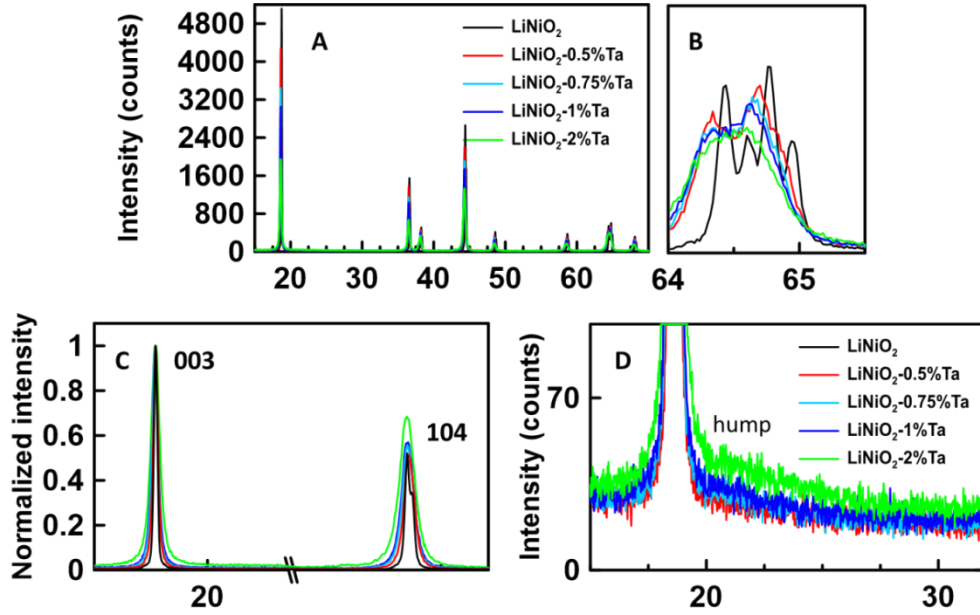
Figure 6.1. (A) XRD patterns of LNO, Ta0.5-LNO, Ta0.75-LNO, Ta1-LNO, and Ta2-LNO synthesized at 730ºC; (B) Expanded view of (018)/(110) peak; (C) (003) and (104) peaks with normalized intensity in order to show the change of (104)/(003) intensity ratio with Ta amount more clearly; (D) Expanded view of the "hump" region which indicates the existence of amorphous $Li_xTa_yO_z$ phases. The data in D has not been normalized.

Table 6.2. Rietveld refinement results of samples synthesized in this chapter.

	a (Å)	c (Å)	Ni in Li layer (%)
LNO (700ºC)	2.8761	14.1907	0.737
Ta0.5-LNO (730ºC)	2.8762	14.2013	1.850
Ta0.75-LNO (730ºC)	2.8773	14.2042	2.111
Ta1-LNO (730ºC)	2.8780	14.2048	3.128
Ta2-LNO (730ºC)	2.8804	14.2107	5.136
W1-LNO (800ºC)	2.8783	14.2038	2.412
W2-LNO (800ºC)	2.8804	14.2061	4.255

Figure 6.2A shows a comparison of the (104)/(003) intensity ratio between Ta1-LNO and W1-LNO. The intensity ratios of Ta1-LNO and W1-LNO are very similar indicating that their amounts of Li/Ni mixing are close as indicated in Table 6.2. The (104)/(003) intensity ratio of Ta1-LNO is slightly higher than that of W1-LNO suggesting larger Li/Ni mixing in Ta1-LNO, again in agreement with Table 6.2. The same trend is shown in Figure 6.2B that Ta2-LNO has higher Li/Ni mixing than W2-LNO, again in agreement with Table 6.2. Therefore, the same molar ratio of Ta compared to W introduces a bit more Li/Ni mixing, suggesting that $Li_xTa_yO_z$ "steals" more Li than $Li_xW_yO_z$.
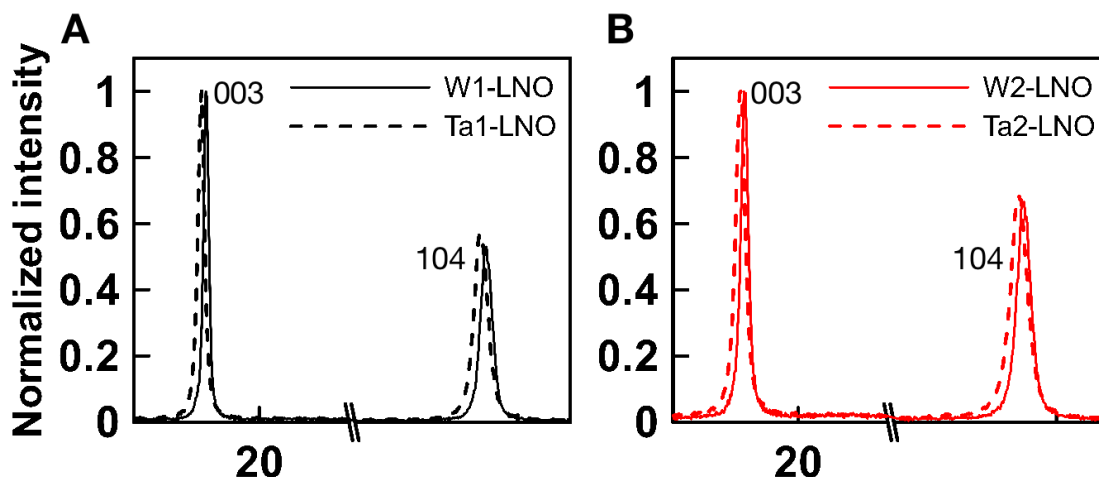
Figure 6.2. (003) and (104) peaks with normalized intensity in order to compare the (104)/(003) intensity ratio between (A) Ta1-LNO and W1-LNO; (B) Ta2-LNO and W2-LNO.

The Fourier transforms (FT) of the extended X-ray absorption fine structure (EXAFS) for the Ni K-edge of LNO, the W L3-edge of W2-LNO, and the Ta L3-edge of Ta2-LNO

shown in Figure 6.3 can help to determine the location of W and Ta in these materials. The FT-EXAFS curve of LNO shows 4 major peaks "I", "II", "III", "IV" from 0 to 6 Å, and these peaks represent signals from inner to outer shells surrounding Ni atoms. Dopants that have substituted for Ni in the crystal lattice of LNO will show 4 peaks in FT-EXAFS the same as LNO, since the dopants stay in the same local environment as Ni and are also surrounded by the same shells. Wang et al. reported the FT-EXAFS for Ni, Co, Mn K edges of NMC721, NMC712, NC73, and LNO. Mn and Co also show distinct 4 peaks just like Ni, and we know that Co and Mn are two known substituents for Ni in LNO[129]. However, both the FT-EXAFS curves of W and Ta do not resemble the data for Ni at all, suggesting that W and Ta are not substitutional dopants for Ni. Therefore, FT-EXAFS curves support that Ta plays the same role as W and stays in the grain boundaries as amorphous $Li_xTa_yO_z$ phases instead of substituting for Ni in the LNO crystal lattice.
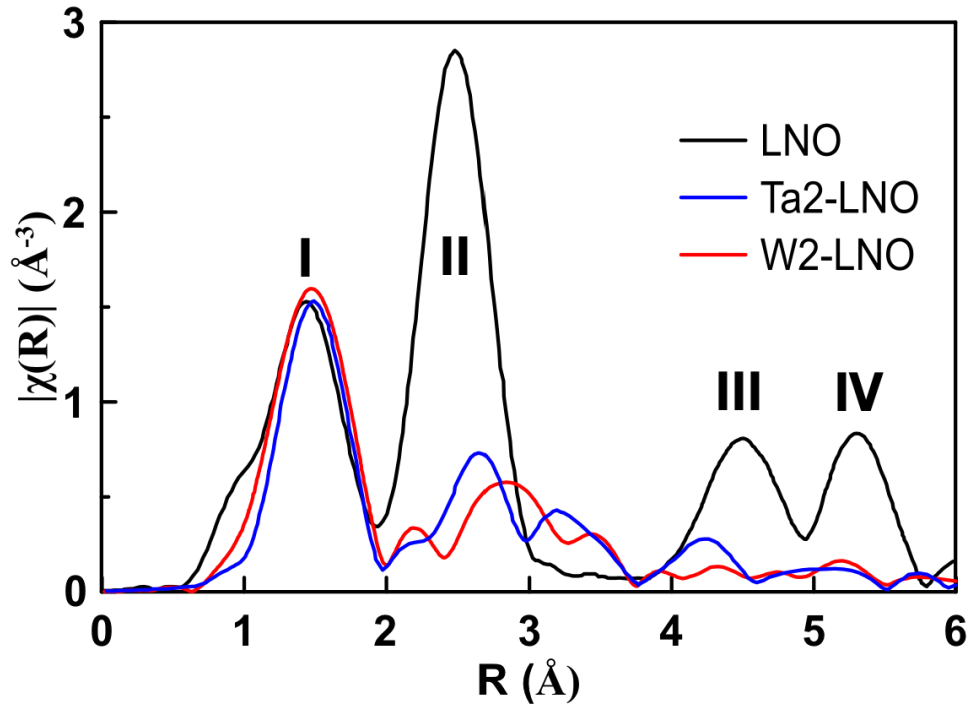
Figure 6.3. Fourier transform (FT) of the extended X-ray absorption fine structure for Ni

K-edge in LNO, W L3-edge in W2-LNO, and Ta L3-edge in Ta2-LNO, respectively.

Figure 6.4 shows the SEM images of the as-synthesized samples in this chapter. Compared to LNO, all the Ta-containing LNOs show smaller primary particle sizes, which corresponds to the broadening of (003), (104), (018) and (110) peaks as the amount of Ta increases in the samples.
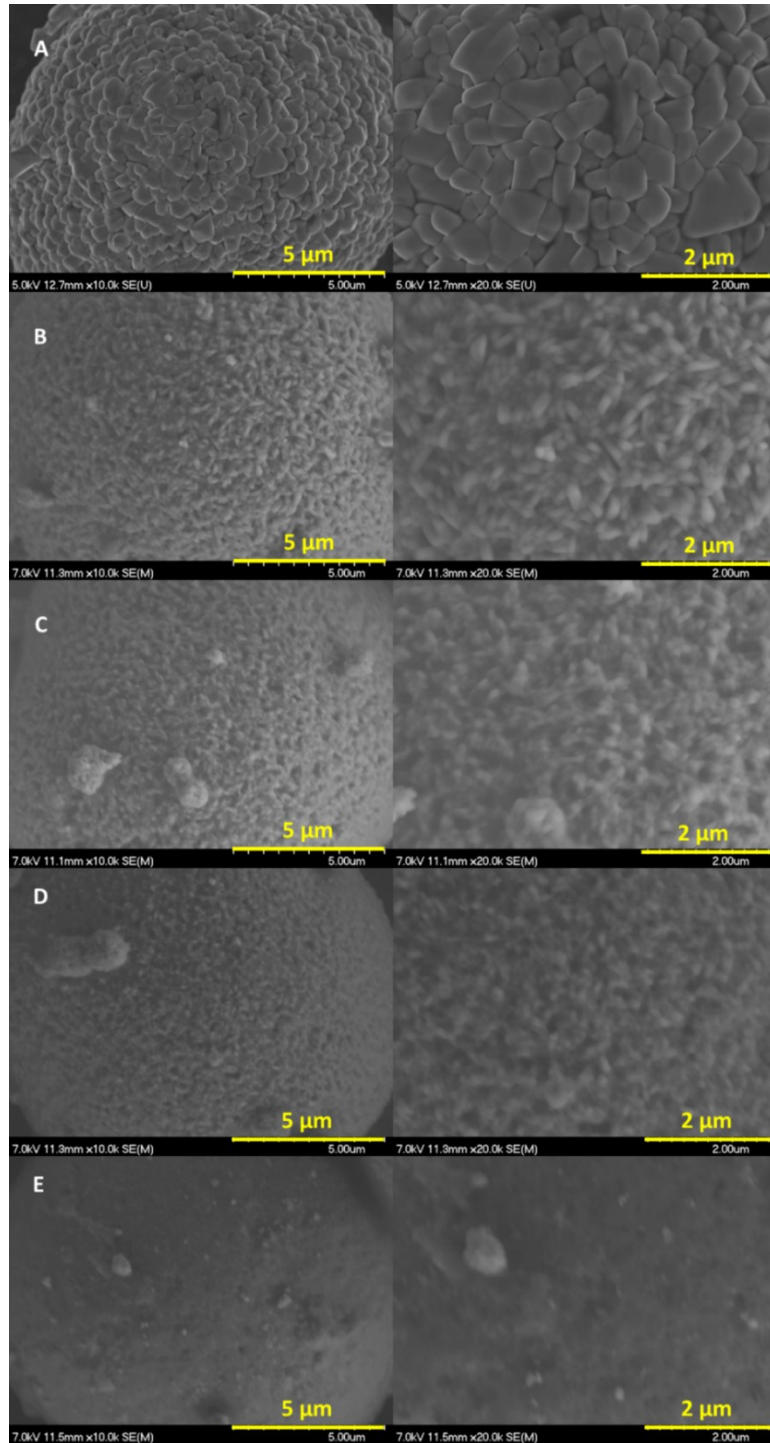
Figure 6.4. Scanning electron microscopy images of (A)LNO, (B)Ta0.5-LNO,

(C)Ta0.75-LNO, (D)Ta1-LNO, and (E)Ta2-LNO.

Figure 6.5A shows the discharge specific capacity versus cycle number for the samples described above. All the samples showed better capacity retention after adding Ta and Ta0.75-LNO showed the best performance in terms of both specific capacity and capacity retention. Ta0.75-LNO had a specific capacity of 209.1 mAh/g at the 21st cycle and 197.4 mAh/g at 80th cycle, which means a capacity retention of 94.4% over 60 cycles at C/5. Figure 6.5B shows the dQ/dV vs. V curves of the described samples and the dQ/dV peak intensities decreased with increasing amount of Ta in samples, which follows the expected trend when Ni/Li mixing increased in layered oxide materials.[44] Figure 6.5C and D show that the peak intensity at 4.2 V dropped dramatically at the 53rd cycle for LNO indicating impedance growth, while it remained almost the same for Ta0.75-LNO, highlighting the improved cycling stability of Ta0.75-LNO.
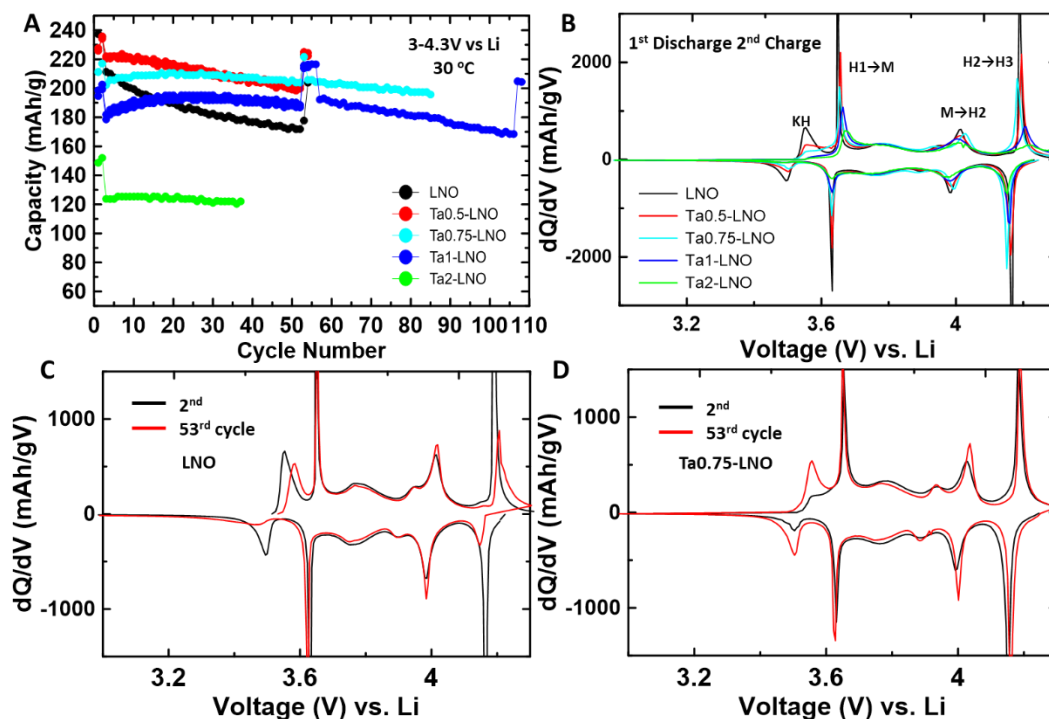
Figure 6.5. (A) Discharge specific capacity versus cycle number for LNO, Ta0.5-LNO, Ta0.75-LNO, Ta1-LNO, and Ta2-LNO – The testing was done between 4.3 and 3.0 V at 30°C. Cycles 1,2, 52 and 53 were made at C/20 while the others were made at C/5; (B) dQ/dV vs. V curves of 1st discharge and 2nd charge process; Comparison of 2nd cycle and the 53rd cycle dQ/dV vs. V curves of LNO (C) and Ta0.75-LNO (D).

Figure 6.6A compares the cycling performance between Ta0.75-LNO (best performance among Ta-doped samples in this chapter) and W1-LNO (best performance among W-doped samples reported previously in chapter 5[15]). Ta0.75-LNO has a lower initial specific capacity, but it has a better capacity retention than W1-LNO for the first 50 cycles, and the capacity fade rate becomes similar for the two samples after 50 cycles. Figure 6.6B shows that Ta0.75-LNO and W1-LNO have similar charge/discharge voltage

vs. specific capacity curves. Ta0.75-LNO delivered smaller capacity at the plateaus at 3.5V and 4.2V, consistent with its smaller specific capacity shown in Figure 6.6A. Overall, Ta0.75-LNO and W1-LNO have comparable capacity retention and specific capacity.
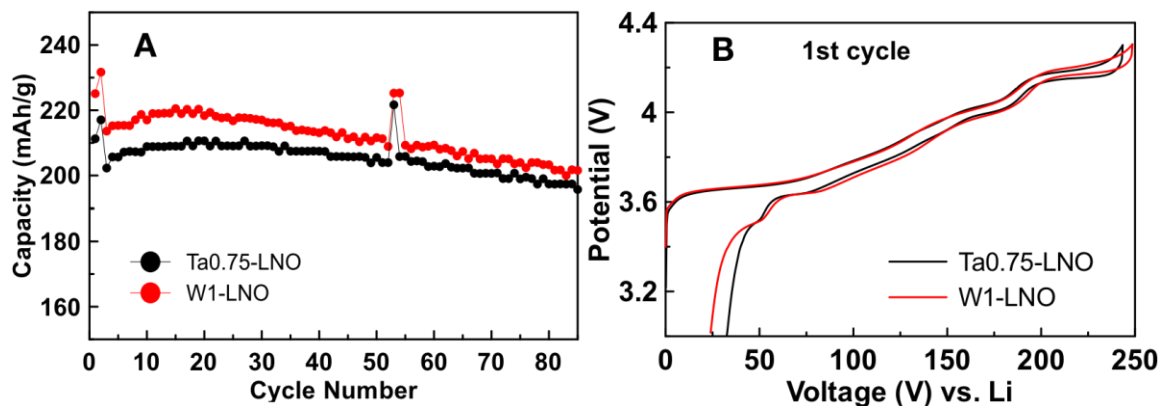
Figure 6.6. (A) Discharge specific capacity versus cycle number for Ta0.75-LNO and W1-LNO – The testing was done between 4.3 and 3.0 V at 30°C. Cycles 1,2, 52 and 53 were made at C/20 while the others were made at C/5; (B) V vs. Specific capacity curves of 1st charge and discharge process for Ta0.75-LNO and W1-LNO. The W1-LNO data are from Geng et al.[15] Reprinted with permission from Advanced Energy Materials.

Copyright 2022.

6.3 Summary

In this chapter, we synthesized tantalum-containing $LiNiO_2$ samples and studied the structural and electrochemical properties of the synthesized samples by XRD, SEM and long-term cycling tests. All Ta-containing LNOs showed well-developed layered structures and smaller crystalline sizes compared to pure LNO. Long-term cycling results showed that among all the samples, LNO with 0.75mol% Ta showed the best capacity retention of 94.4% for 60 cycles. We compared the XRD patterns of tantalum-containing samples with tungsten-containing samples, and the addition of the same molar ratio of tantalum introduced slightly higher Li/Ni mixing. We also compared the long-term charge/discharge cycling tests of Ta0.75-LNO and W1-LNO, the best performance sample in Ta-containing and W-containing samples respectively. The initial specific discharge capacity of Ta0.75-LNO was only slightly lower than that of W1-LNO, and both samples have excellent capacity retention despite their ultra-high Ni content. Fourier-transformed extended X-ray absorption fine structure curves show that the Ta atoms in Ta2-LNO and the W atoms in W1-LNO do not substitute for Ni in the LNO structure.

The effects of Ta additions to $LiNiO_2$ are thought to be analogous to those of W additions to $LiNiO_2$. That is, Ta is not incorporated within the crystal structure of $LiNiO_2$ but instead is thought to exist as an amorphous $Li_xTa_yO_z$ phase in the grain boundaries between the $LiNiO_2$ primary particles.[16,18] Like in the case of W, a hump near 20-22

degrees in the XRD pattern which increases with Ta content is present, indicating amorphous $Li_xTa_yO_z$ phases. Like in the case of W, adding Ta causes a reduction in the size of the $LiNiO_2$ primary particles again suggesting the $Li_xTa_yO_z$ phases in the grain boundaries limit particle growth. We have not expended the resources to do high resolution TEM on the Ta-containing samples, nor have we expended the effort to do mechanical strength measurements[18] but we are confident that Ta is incorporated in the same way as W in $LiNiO_2$.

Chapter 7 Conclusions and Future Work

7.1 Conclusions

The quest for cleaner and more sustainable energy solutions has intensified the demand for high-performance batteries. High-Ni layered oxide materials have gained significant attention and importance in the field of energy storage, particularly in rechargeable lithium-ion batteries. High-Ni layered oxide materials offer high specific capacity, enabling the development of lithium-ion batteries with superior energy density, supporting the transition to electric vehicles and renewable energy storage. However, high-Ni layered oxide materials come with the drawback of relatively rapid capacity fade, which limits their commercialization in industry. This thesis introduced a dry particle fusion instrument that can apply coatings on materials to improve their performance and some detailed studies on the mechanism of action of adding different high-valence elements (tungsten and tantalum) on $LiNiO_2$.

Chapters 1 and 2 gave an introduction on lithium-ion batteries and experimental techniques used in this thesis. Chapter 3 introduced a dry particle fusion instrument built at Dalhousie that can apply coatings by mechanical force to improve the performance of cathode materials. It was shown that this dry particle fusion instrument is able to apply coatings repeatably from run to run. In addition, the capacity retention of $Ni(OH)_2$ coated with nano-Al_2O_3 followed by lithiation was greatly improved compared to that of

$Ni(OH)_2$ without coatings followed by lithiation, demonstrating this dry particle fusion can successfully apply effective coatings to improve the performance of materials.

Chapter 4 further gave a detailed study on applying coatings of different ratios of nano-Al_2O_3 on $Ni(OH)_2$. Coatings were made successfully without breaking the core materials and capacity retentions were all improved for materials coated with different ratios of nano-Al_2O_3 compared to the material without coating.

Chapter 5 and 6 studied how tungsten and tantalum effectively improved capacity retention in $LiNiO_2$, respectively. Both tungsten- and tantalum-added $LiNiO_2$ were prepared by dry particle fusion, and followed by heating with a lithium source. The tungsten was shown for the first time to be incorporated in $Li_xW_yO_z$ amorphous phases between and on the surface of $LiNiO_2$ grains, suppressing the growth of primary particles, reducing the volume change of primary particles during charge and discharge, thus reducing the secondary particle cracking. In addition, the $Li_xW_yO_z$ phase possibly worked as a "glue" to bind the primary particles and improved the mechanical strength of the secondary particles. We believe that tantalum works similarly to tungsten.

To see if the W- and Ta-added LNO reported in this thesis gave a good cycling performance, Figure 7.1 compares the half coin cell cycling performance of the W- and Ta-added LNO (or ultra-high Ni layered oxide) reported in this thesis and in other publications.[52,130] Very limited amount of researches were published on W- and Ta-addition to pure LNO or ultra-high Ni layered oxide, the author chose the W1.5-LNO

reported by Ryu et al.[52] (the best cycling performance among all the W-added LNO with different W ratios in that publication) and Ta1-NC ($LiNi_{0.95}Co_{0.04}Ta_{0.01}O_2$) reported by Kim et al.[130] Both W1.5-LNO and Ta1-NC were cycled at a specific current of 90 mA g^{-1} (~C/2) between 2.7-4.3 V at 30 °C with an active material loading of 4-5 mg cm^{-2}. The W1-LNO and Ta0.75-LNO in this thesis were cycled at a specific current of 40 mA g^{-1} (~C/5) between 3.0-4.3 V at 30 °C with an active material loading of 10-12 mg cm^{-2}. Both W1-LNO and Ta0.75-LNO delivered a smaller specific capacity than W1.5-LNO and Ta1-NC, which is possibly due to a higher active material loading, but all of the materials had similar and excellent capacity retention as ultra-high Ni layered oxide materials, although W1-LNO had a slightly worse capacity retention, proving that the additions of high-valence W and Ta to LNO are beneficial to the cycle life of LNO.
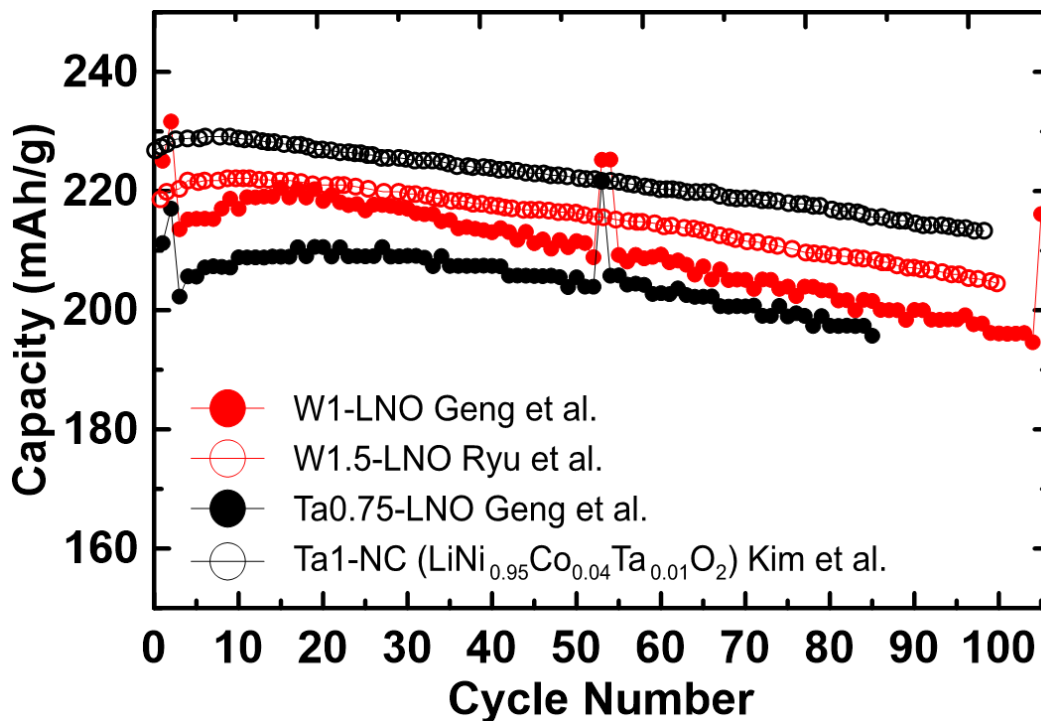
Figure 7.1 Comparison of charge-discharge performance of W1-LNO and Ta0.75-LNO

reported in this thesis with W- and Ta-added high Ni materials (W1.5-LNO and Ta1-NC)

reported by other authors[52,130]. Reprinted with permission from H. H. Ryu, G. T. Park, C.

S. Yoon, Y. K. Sun, *J Mater Chem A Mater* **2019**, *7*, 18580.[52] Copyright 2019 Royal

Society of Chemistry. Reprinted with permission from U. H. Kim, G. T. Park, B. K. Son,

G. W. Nam, J. Liu, L. Y. Kuo, P. Kaghazchi, C. S. Yoon, Y. K. Sun, *Nature Energy 2020*

5:11 **2020**, *5*, 860.[26] Copyright 2020 Nature.

Figure 7.2 summarizes the impurity region (19°-30°) of XRD patterns for pure LNO and LNO added with 5 mol% aluminum, 5 mol% magnesium, 4 mol% tungsten, and 4 mol% tantalum, which were shortened as Al5-LNO, Mg5-LNO, W4-LNO and Ta4-LNO respectively. The Al5-LNO was reported in Chapter 4, which is the sample lithiated $Ni(OH)_2$ with 3wt% Al_2O_3 (sample 3PFL) and will be used to represent sample 3PFL in the following text. The W4-LNO was reported in Chapter 5. The Mg5-LNO and Ta4-LNO were synthesized by the author following the same procedure discussed in Chapter 2 at a lithiation temperature of 700 °C and 730 °C, respectively. An amorphous phase was shown in the XRD patterns (19°-30°) for both W4-LNO and Ta4-LNO, while the Mg5-LNO and Al5-LNO didn't show a second phase in their XRD patterns, which is the evidence that W and Ta exist in a second phase instead of $LiNiO_2$ phase. We believe that the additions of high-valence elements, W, Ta, Nb, and Mo, etc., function in the same way that they stay in a Li-M-O second phase, (M =high valence elements W, Ta, Nb, and Mo, etc.) instead of being incorporated into the layered oxide structure, to improve the cycling performance of layered oxide materials.
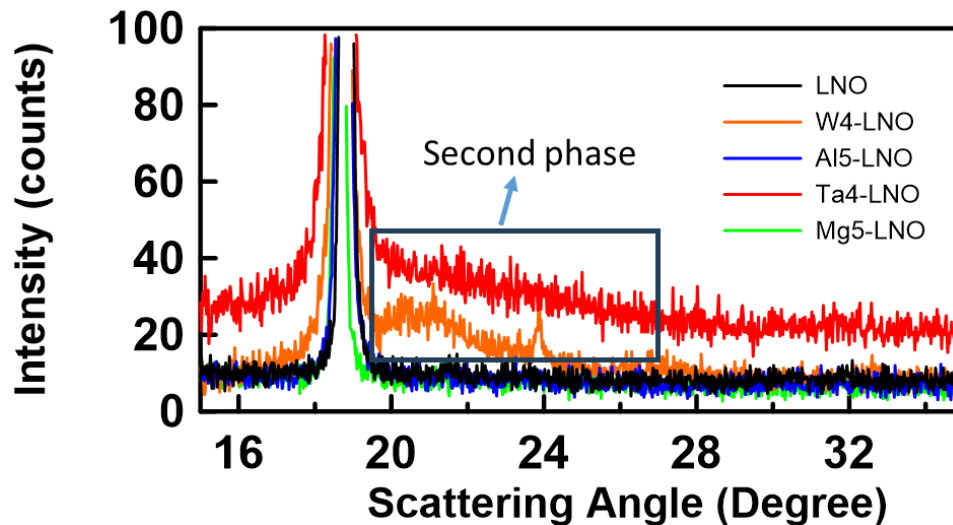
Figure 7.2 The impurity region (19°-30°) of XRD patterns for pure LNO and LNO added

with 5 mol% aluminum (Al5-LNO), 5 mol% magnesium (Mg5-LNO), 4 mol% tungsten

(W4-LNO), and 4 mol% tantalum (Ta4-LNO).

7.2 Future Work

7.2.1 Impact of Surface Smoothing

As introduced, one way to improve cycle life of positive electrode material is to hinder

the parasitic reactions happening between cathode surface and electrolyte. The larger

cathode surface area gives more parasitic reaction sites, and therefore the degradation of

positive electrode is faster. Chapter 3 shows that core particle surfaces become smooth

after dry particle fusion, which offers the possibility of reducing the cathode surface area

due to the smoothing of cathode particles by dry particle fusion. Zheng et al. have

reported that mechanofusion-processed NMC622 had significantly improved cycling

retention than the pristine one.[24]

The impact of surface smoothing by dry particle fusion on cathode materials is in need. Future study will involve SEM to observe the morphology of particles before and after dry particle fusion, XRD to observe the structure change, BET to test the difference in porosity before and after dry particle fusion, and electrochemical testing. Optimization of spinning speed and duration will also be involved.

7.2.2 Impact of Surface Coating

Inactive materials, e.g. Al_2O_3, SiO_2, are often used to apply a coating layer on the cathode particle surfaces, which avoids the direct contact of cathode surface and electrolyte. Electrochemically stable cathode materials, such as $LiFePO_4$ (LFP), are also reported to be helpful for improving capacity retention when coated on the core cathode particle surface. Zhong et al. reported that LFP coated NCM based 18650 full cells show excellent cycling stability with capacity retention of 91.65%, much higher than that of 70.65% of pristine NCM after 500 cycles at 1C. The obvious difference may be attributed to a reliable LFP coating layer, which can suppress the direct reaction between NCM and electrolyte, hence increases the cycling stability.[131] Carbon coating has gained much attention owing to its low cost, improved conductivity, stability, and secures electron transfer. Carbon-coated NCA displays a significantly higher capacity retention of 84% at 0.5C after 250 cycles, whereas pristine NCA retains 71%, besides, the carbon-coated material exhibited improved rate performance attributed to the better electronic conductivity of the carbon coating layer.[132]

More study is required to get effective coatings for positive or negative electrode materials by dry particle fusions. A suggested study will involve SEM and cross-sectional SEM to observe the morphology of particles and coating layers before and after dry particle fusion. Electrochemical testing will be involved to see if applying coatings of the above-mentioned materials can improve positive electrode material capacity retention, and find the optimized coating amount, spinning speed and duration for each coating material.

7.2.3 Is the addition of high valence elements absolutely necessary for layered oxide materials?

Figure 7.3 summarizes the charge-discharge specific capacity vs. cycle number of the best materials, Al5-LNO, W1-LNO, and Ta0.75-LNO, in Chapters 4, 5 and 6, respectively. Both W1-LNO and Ta0.75-LNO gave good capacity retentions, however, it is surprising to see the cycling performance of the Al5-LNO exactly overlap with W1-LNO. This observation indicates the possibility of getting Ni-based layered oxide materials with same capacity retention by substituting Ni with some common dopants, Al, Mg, Mn etc., instead of the addition of high valence elements, W, Ta, etc.

The addition of high valence elements is shown to be beneficial to Ni-based layered oxide by forming the Li-M-O phase to limit the primary particle growth and increase the mechanical strength of the secondary particle during cycling. It could be worth to do further exploration to see if high valence elements are removable from Ni-based layered

oxides. It is a possibility that the same performance can be achieved by tuning the ratio of well-known dopants and synthesizing conditions, lithiation temperature and duration, etc, without introducing high-valence elements. Study will also include different techniques to examine the physical and electrochemical properties of the synthesized samples.
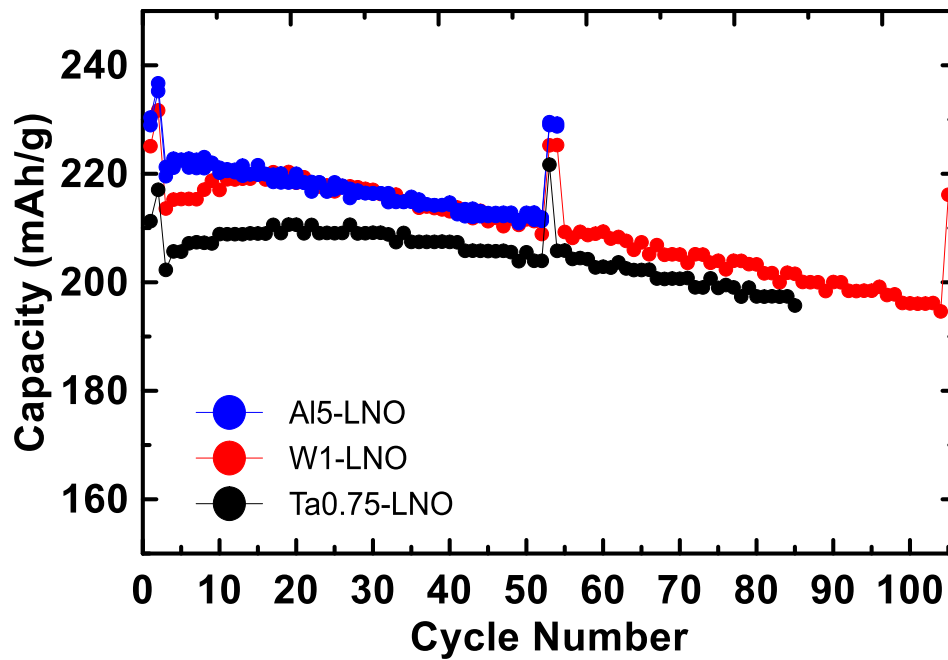
Figure 7.3 Comparison of Al5-LNO, W1-LNO, Ta0.75-LNO (the materials with best cycling performance in Chapter 3, 4 and 5, respectively).

References

[1] M. D. Radin, S. Hy, M. Sina, C. Fang, H. Liu, J. Vinckeviciute, M. Zhang, M. S. Whittingham, Y. S. Meng, A. Van der Ven, *Adv Energy Mater* **2017**, *7*, 1602888.

[2] V. Etacheri, R. Marom, R. Elazari, G. Salitra, D. Aurbach, *Energy Environ Sci* **2011**, *4*, 3243.

[3] Y. Lyu, X. Wu, K. Wang, Z. Feng, T. Cheng, Y. Liu, M. Wang, R. Chen, L. Xu, J. Zhou, Y. Lu, B. Guo, by B. John Goodenough, Y. Lyu, Z. Feng, T. Cheng, Y. Liu, R. Chen, J. Zhou, B. Guo, X. Wu, K. Wang, M. Wang, L. Xu, Y. Lu, *Adv Energy Mater* **2021**, *11*, 2000982.

[4] B. Dunn, H. Kamath, J. M. Tarascon, *Science (1979)* **2011**, *334*, 928.

[5] W. Yan, S. Yang, Y. Huang, Y. Yang, Guohui Yuan, *J Alloys Compd* **2020**, *819*, 153048.

[6] M. S. Whittingham, *Chem Rev* **2004**, *104*, 4271.

[7] H. J. Noh, S. Youn, C. S. Yoon, Y. K. Sun, *J Power Sources* **2013**, *233*, 121.

[8] X. Li, W. Ge, K. Zhang, G. Peng, Y. Fu, X. Ma, *Electrochim Acta* **2022**, *403*, 139653.

[9] S. Jamil, R. Yu, Q. Wang, M. Fasehullah, Y. Huang, Z. Yang, X. Yang, X. Wang, *J Power Sources* **2020**, *473*, 228597.

[10] B. Chu, S. Liu, L. You, D. Liu, T. Huang, Y. Li, A. Yu, *ACS Sustain Chem Eng* **2020**, *8*, 3082.

[11] H. Ryu, K. Park, D. R. Yoon, A. Aishova, C. S. Yoon, Y. K. Sun, *Adv Energy Mater* **2019**, *9*, 1902698.

[12] U. H. Kim, D. W. Jun, K. J. Park, Q. Zhang, P. Kaghazchi, D. Aurbach, D. T. Major, G. Goobes, M. Dixit, N. Leifer, C. M. Wang, P. Yan, D. Ahn, K. H. Kim, C. S. Yoon, Y. K. Sun, *Energy Environ Sci* **2018**, *11*, 1271.

[13] G. Shang, Y. Tang, Y. Lai, J. Wu, X. Yang, H. Li, C. Peng, J. Zheng, Z. Zhang, *J Power Sources* **2019**, *423*, 246.

[14] D. Rathore, M. Garayt, Y. Liu, C. Geng, M. Johnson, J. R. Dahn, C. Yang, *ACS Energy Lett* **2022**, *7*, 2189.

[15] C. Geng, D. Rathore, D. Heino, N. Zhang, I. Hamam, N. Zaker, G. A. Botton, R. Omessi, N. Phattharasupakun, T. Bond, C. Yang, J. R. Dahn, *Adv Energy Mater* **2022**, *12*, 2103067.

[16] D. Rathore, C. Geng, N. Zaker, I. Hamam, Y. Liu, P. Xiao, G. A. Botton, J. Dahn, C. Yang, *J Electrochem Soc* **2021**, *168*, 120514.

[17] I. Hamam, R. Omessi, D. Rathore, C. Geng, R. Cooke, K. Plucknett, D. P. Bishop, N. Zaker, G. A. Botton, C. Yang, J. R. Dahn, *Cell Rep Phys Sci* **2022**, *3*, 100714.

[18] I. Hamam, R. Omessi, D. Rathore, C. Geng, R. Cooke, K. Plucknett, D. P. Bishop, N. Zaker, G. A. Botton, C. Yang, J. R. Dahn, *Joule* **n.d.**

[19] L. A. Riley, S. Van Atta, A. S. Cavanagh, Y. Yan, S. M. George, P. Liu, A. C. Dillon, S. H. Lee, *J Power Sources* **2011**, *196*, 3317.

[20] Y. S. Jung, A. S. Cavanagh, A. C. Dillon, M. D. Groner, S. M. George, S.-H. Lee, *J Electrochem Soc* **2010**, *157*, A75.

[21] A. Zhou, Q. Liu, Y. Wang, W. Wang, X. Yao, W. Hu, L. Zhang, X. Yu, J. Li, H. Li, *J Mater Chem A Mater* **2017**, *5*, 24361.

[22] D. Pritzl, T. Teufl, A. T. S. Freiberg, B. Strehle, J. Sicklinger, H. Sommer, P. Hartmann, H. A. Gasteiger, *J Electrochem Soc* **2019**, *166*, A4056.

[23] L. Zheng, T. D. Hatchard, M. N. Obrovac, *MRS Commun* **2019**, *9*, 245.

[24] L. Zheng, C. Wei, M. D. L. Garayt, J. MacInnis, M. N. Obrovac, *J Electrochem Soc* **2019**, *166*, A2924.

[25] T. Hwang, J. K. Lee, J. Mun, W. Choi, *J Power Sources* **2016**, *322*, 40.

[26] J. B. Goodenough, K. S. Park, *J Am Chem Soc* **2013**, *135*, 1167.

[27] D. A. Winn, J. M. Shemilt, B. C. H. Steele, *Mater Res Bull* **1976**, *11*, 559.

[28] M. S. Whittingham, *Science (1979)* **1976**, *192*, 1126.

[29] Y. Zhang, T. T. Zuo, J. Popovic, K. Lim, Y. X. Yin, J. Maier, Y. G. Guo, *Materials Today* **2020**, *33*, 56.

[30] J. B. Goodenough, K. Mizushima, T. Takeda, *Jpn J Appl Phys* **1980**, *19*, 305.

[31] K. Mizushima, P. C. Jones, P. J. Wiseman, J. B. Goodenough, *Mater Res Bull* **1980**, *15*, 783.

[32] Z. Chen, J. R. Dahn, *Electrochim Acta* **2004**, *49*, 1079.

[33] A. Liu, J. Li, R. Shunmugasundaram, J. R. Dahn, *J Electrochem Soc* **2017**, *164*, A1655.

[34] Z. Li, H. Yi, H. Ren, J. Fang, Y. Du, W. Zhao, H. Chen, Q. Zhao, F. Pan, *Adv Funct Mater* **2023**, 2307913.

[35] C. Geng, A. Liu, J. R. Dahn, *Chemistry of Materials* **2020**, *32*.

[36] C. Geng, S. Trussler, M. Johnson, N. Zaker, B. Scott, G. Botton, J. R. Dahn, *J Electrochem Soc* **2020**, *167*, 110509.

[37] H. Li, N. Zhang, J. Li, J. R. Dahn, *J Electrochem Soc* **2018**, *165*, A2985.

[38] N. Nitta, F. Wu, J. T. Lee, G. Yushin, *Materials Today* **2015**, *18*, 252.

[39] B. A. Hunter, **2000**.

[40] B. D. Cullity, S.R. Stock, *Elements of X-Ray Diffraction*, Prentice-Hall, New York, **n.d.**

[41] A. Rougier, P. Gravereau, C. Delmas, *J Electrochem Soc* **1996**, *143*, 1168.

[42] J. P. Peres, C. Delmas, A. Rougier, M. Broussely, F. Perton, P. Biensan, P. Willmann, *Journal of Physics and Chemistry of Solids* **1996**, *57*, 1057.

[43] Y. Ren, R. Yamaguchi, T. Uchiyama, Y. Orikasa, T. Watanabe, K. Yamamoto, T. Matsunaga, Y. Nishiki, S. Mitsushima, Y. Uchimoto, *ChemElectroChem* **2021**, *8*, 70.

[44] N. Phattharasupakun, M. M. E. Cormier, E. Lyle, E. Zsoldos, A. Liu, C. Geng, Y. Liu, H. Li, M. Sawangphruk, J. R. Dahn, *J Electrochem Soc* **2021**, *168*, 090535.

[45] P. Kalyani, N. Kalaiselvi, *Sci Technol Adv Mater* **2005**, *6*, 689.

[46] C. S. Yoon, D. W. Jun, S. T. Myung, Y. K. Sun, *ACS Energy Lett* **2017**, *2*, 1150.

[47] H. Li, N. Zhang, J. Li, J. R. Dahn, *J Electrochem Soc* **2018**, *165*, A2985.

[48] H. Li, A. Liu, N. Zhang, Y. Wang, S. Yin, H. Wu, J. R. Dahn, *Chemistry of Materials* **2019**, *31*, 7574.

[49] H. Li, M. Cormier, N. Zhang, J. Inglis, J. Li, J. R. Dahn, *J Electrochem Soc* **2019**, *166*, A429.

[50] H. H. Sun, H.-H. Ryu, U.-H. Kim, J. A. Weeks, A. Heller, Y.-K. Sun, C. B. Mullins, *ACS Energy Lett* **2020**, 1136.

[51] W. Li, J. Zhang, Y. Zhou, W. Huang, X. Liu, Z. Li, M. Gao, Z. Chang, N. Li, J. Wang, S. Lu, X. Li, W. Wen, D. Zhu, Y. Lu, W. Zhuang, *ACS Appl Mater Interfaces* **2020**, *12*, 47513.

[52] H. H. Ryu, G. T. Park, C. S. Yoon, Y. K. Sun, *J Mater Chem A Mater* **2019**, *7*, 18580.

[53] D. Becker, M. Börner, R. Nölle, M. Diehl, S. Klein, U. Rodehorst, R. Schmuch, M. Winter, T. Placke, *ACS Appl Mater Interfaces* **2019**, *11*, 18404.

[54] J. Huang, H. Liu, T. Hu, Y. S. Meng, J. Luo, *J Power Sources* **2018**, *375*, 21.

[55] Y.-G. Zou, H. Mao, X.-H. Meng, Y.-H. Du, H. Sheng, X. Yu, J.-L. Shi, Y.-G. Guo, *Angewandte Chemie* **2021**, DOI 10.1002/ANGE.202111954.

[56] H. H. Sun, U. H. Kim, J. H. Park, S. W. Park, D. H. Seo, A. Heller, C. B. Mullins, C. S. Yoon, Y. K. Sun, *Nature Communications 2021 12:1* **2021**, *12*, 1.

[57] C. M. Choi, J. H. Park, Y. K. Sun, C. S. Yoon, *J Power Sources* **2021**, *513*, 230548.

[58] F. Lv, Y. Zhang, M. Wu, Y. Gu, *Appl Phys Lett* **2021**, *119*, 023903.

[59] L. J. Krause, L. D. Jensen, J. R. Dahn, *J Electrochem Soc* **2012**, *159*, A937.

[60] N. N. Sinha, A. J. Smith, J. C. Burns, G. Jain, K. W. Eberman, E. Scott, J. P. Gardner, J. R. Dahn, *J Electrochem Soc* **2011**, *158*, A1194.

[61] L. E. Downie, S. R. Hyatt, J. R. Dahn, *J Electrochem Soc* **2016**, *163*, A35.

[62] M. D. Radin, S. Hy, M. Sina, C. Fang, H. Liu, J. Vinckeviciute, M. Zhang, M. S. Whittingham, Y. S. Meng, A. Van der Ven, *Adv Energy Mater* **2017**, *7*.

[63] Z. Wang, X. Huang, L. Chen, *J Electrochem Soc* **2004**, *151*, A1641.

[64] S. Liu, Z. Liu, X. Shen, W. Li, Y. Gao, M. N. Banis, M. Li, K. Chen, L. Zhu, R. Yu, Z. Wang, X. Sun, G. Lu, Q. Kong, X. Bai, L. Chen, *Adv Energy Mater* **2018**, *8*, 1802105.

[65] M. Alonso, M. Satoh, K. Miyanami, *Powder Technol* **1989**, *59*, 45.

[66] W. Chen, R. N. Dave, R. Pfeffer, O. Walton, *Powder Technol* **2004**, *146*, 121.

[67] T. Kato, H. Ushijima, M. Katsumata, T. Hyodo, Y. Shimizu, M. Egashira, *Journal of the American Ceramic Society* **2004**, *87*, 60.

[68] F. Jay, V. Gauthier, S. Dubois, *Journal of the American Ceramic Society* **2006**, *89*, 3522.

[69] T. Yokoyama, K. Urayama, M. Naito, M. Kato, T. Yokoyama, *KONA Powder and Particle Journal* **1987**, *5*, 59.

[70] Y. Cao, T. D. Hatchard, R. A. Dunlap, M. N. Obrovac, *J Mater Chem A Mater* **2019**, *7*, 8335.

[71] A. Van Bomme, J. R. Dahn, *Chemistry of Materials* **2009**, *21*, 1500.

[72] C. Zhaorong, L. Gongan, Z. Yujuan, C. Jianguo, D. Yunchang, *J Power Sources* **1998**, *74*, 252.

[73] G. T. Park, H. H. Ryu, N. Y. Park, C. S. Yoon, Y. K. Sun, *J Power Sources* **2019**, *442*, 227242.

[74] F. Zhou, X. Zhao, A. Van Bommel, A. W. Rowe, J. R. Dahn, *Chemistry of Materials* **2010**, *22*, 1015.

[75] J. I. Goldstein, D. E. Newbury, P. Echlin, D. C. Joy, A. D. Romig, C. E. Lyman, C. Fiori, E. Lifshin, **1992**, DOI 10.1007/978-1-4613-0491-3.

[76] W. Zhou, Z. L. Wang, *Scanning Microscopy for Nanotechnology: Techniques and Applications* **2007**, 1.

[77] D. B. Williams, C. B. Carter, *Transmission Electron Microscopy: A Textbook for Materials Science* **2009**, 1

[78] "TEM: Bright field versus dark field - Chemistry LibreTexts," can be found under https://chem.libretexts.org/Courses/Franklin_and_Marshall_College/Introduction_to_Materials_Characterization__CHM_412_Collaborative_Text/Electron_and_Probe_Microscopy/TEM%3A_Bright_field_versus_dark_field**.**

[79] M. Newville, *Rev Mineral Geochem* **2014**, *78*, 33.

[80] D. C. Koningsberger, B. L. Mojet, G. E. Van Dorssen, D. E. Ramaker, *Top Catal* **2000**, *10*, 143.

[81] V. Murray, D. S. Hall, J. R. Dahn, *J Electrochem Soc* **2019**, *166*, A329.

[82] H. H. Sun, H.-H. Ryu, U.-H. Kim, J. A. Weeks, A. Heller, Y.-K. Sun, C. B. Mullins, *ACS Energy Lett* **2020**, *5*, 1136.

[83] S. H. Lee, G. J. Park, S. J. Sim, B. S. Jin, H. S. Kim, *J Alloys Compd* **2019**, *791*, 193.

[84] X. Qu, Z. Yu, D. Ruan, A. Dou, M. Su, Y. Zhou, Y. Liu, D. Chu, *ACS Sustain Chem Eng* **2020**, *8*, 5819.

[85] J. Z. Kong, C. Ren, G. A. Tai, X. Zhang, A. D. Li, D. Wu, H. Li, F. Zhou, *J Power Sources* **2014**, *266*, 433.

[86] W. Cho, S. M. Kim, J. H. Song, T. Yim, S. G. Woo, K. W. Lee, J. S. Kim, Y. J. Kim, *J Power Sources* **2015**, *282*, 45.

[87] N. Phattharasupakun, J. Wutthiprom, S. Duangdangchote, S. Sarawutanukul, C. Tomon, F. Duriyasart, S. Tubtimkuna, C. Aphirakaramwong, M. Sawangphruk, *Energy Storage Mater* **2021**, *36*, 485.

[88] N. N. Greenwood, T. C. Gibb, *Mössbauer Spectroscopy*, Springer Netherlands, Dordrecht, **1971**.

[89] S. T. Myung, F. Maglia, K. J. Park, C. S. Yoon, P. Lamp, S. J. Kim, Y. K. Sun, *ACS Energy Lett* **2017**, *2*, 196.

[90] A. Aishova, G. Park, C. S. Yoon, Y. Sun, *Adv Energy Mater* **2020**, *10*, 1903179.

[91] A. Liu, N. Zhang, J. Li, T. Casagrande, C. Butcher, J. Martinez, A. Korinek, G. Botton, J. R. Dahn, *J Electrochem Soc* **2018**, *165*, A2781.

[92] A. Liu, J. Dahn, *ChemEngineering* **2019**, *3*, 38.

[93] John. Emsley, *The Elements*, Clarendon Press, **1995**.

[94] L. Niu, Z. Li, Y. Xu, J. Sun, W. Hong, X. Liu, J. Wang, S. Yang, *ACS Appl Mater Interfaces* **2013**, *5*, 8044.

[95] H. Farsi, S. A. Hosseini, *Journal of Solid State Electrochemistry* **2013**, *17*, 2079.

[96] F. Zhou, X. Zhao, C. Goodbrake, J. Jiang, J. R. Dahn, *J Electrochem Soc* **2009**, *156*, A796.

[97]   Y. K. Yoon, C. W. Park, H. Y. Ahn, D. H. Kim, Y. S. Lee, J. Kim, *Journal of Physics and Chemistry of Solids* **2007**, *68*, 780.

[98]   J. Wang, B. Qiu, H. Cao, Y. Xia, Z. Liu, *J Power Sources* **2012**, *218*, 128.

[99]   M. Alonso, M. Satoh, K. Miyanami, *Powder Technol* **1989**, *59*, 45.

[100] T. Ohzuku, *J Electrochem Soc* **1993**, *140*, 1862.

[101] W. Li, J. N. Reimers, J. R. Dahn, *Solid State Ion* **1993**, *67*, 123.

[102] J. Li, J. Harlow, N. Stakheiko, N. Zhang, J. Paulsen, J. Dahn, *J Electrochem Soc* **2018**, *165*, A2682.

[103] A. Liu, N. Zhang, H. Li, J. Inglis, Y. Wang, S. Yin, H. Wu, J. R. Dahn, *J Electrochem Soc* **2019**, *166*, A4025.

[104] M. Dalkilic, A. Schmidt, T. D. Schladt, al -, A. Tamura, S. Takai, T. Yabutsuka, *J Electrochem Soc* **2023**, *170*, 070502.

[105] T. Ohzuku, T. Yanagawa, M. Kouguchi, A. Ueda, *J Power Sources* **1997**, *68*, 131.

[106] S. Madhavi, G. V. Subba Rao, B. V. R. Chowdari, S. F. Y. Li, *J Power Sources* **2001**, *93*, 156.

[107] Z. Lu, D. D. MacNeil, J. R. Dahn, *Electrochemical and Solid-State Letters* **2001**, *4*, A191.

[108] M. Yoshio, H. Noguchi, J. ichi Itoh, M. Okada, T. Mouri, *J Power Sources* **2000**, *90*, 176.

[109] T. Ohzuku, Y. Makimura, *Chem Lett* **2001**, *30*, 642.

[110] Z. Liu, A. Yu, J. Y. Lee, *J Power Sources* **1999**, *81–82*, 416.

[111] G. K. Williamson, W. H. Hall, *Acta Metallurgica* **1953**, *1*, 22.

[112] S. A. Speakman, *MIT Center for Materials Science and Engineering* **2014**, 3.

[113] C. Suryanarayana, M. G. Norton, in *X-Ray Diffraction*, Springer, **1998**, pp. 207–221.

[114] R. D. Shannon, *Acta Cryst* **1976**, *32*, 751.

[115] D. Rathore, C. Geng, N. Zaker, I. Hamam, Y. Liu, P. Xiao, G. Botton, J. R. Dahn, C. Yang, *J Electrochem Soc* **2021**.

[116] T. J. Collins, *Biotechniques* **2007**, *43*, S25.

[117] T. Ferreira, W. Rasband, *ImageJ/Fiji* **2012**, *1*, 155.

[118] P. Tabero, A. Frackowiak, *J Therm Anal Calorim* **2017**, *130*, 311.

[119] S. Hsu, *Masters Theses* **1949**.

[120] M. E. Straumanis, S. S. Hsu, *J Am Chem Soc* **1950**, *72*, 4027.

[121] M. M. Cormier, N. Phattharasupakun, E. Lyle, E. Zsoldos, A. Liu, C. Geng, Y. Liu, H. Li, M. Sawangphruk, J. R. Dahn, *J Electrochem Soc* **2021**.

[122] C. Pouillerie, E. Suard, C. Delmas, *J Solid State Chem* **2001**, *158*, 187.

[123] H. Arai, S. Okada, H. Ohtsuka, M. Ichimura, J. Yamaki, *Solid State Ion* **1995**, *80*, 261.

[124] M. V. Jacob, J. G. Hartnett, J. Mazierska, J. Krupka, M. E. Tobar, *IEEE Region 10 Annual International Conference, Proceedings/TENCON* **2003**, *4*, 1362.

[125] F. Gitmans, Z. Sitar, P. Günter, *Vacuum* **1995**, *46*, 939.

[126] S. Kim, V. Gopalan, K. Kitamura, Y. Furukawa, *J Appl Phys* **2001**, *90*, 2949.

[127] J. A. Allemann, Y. Xia, R. E. Morriss, A. P. Wilkinson, H. Eckert, J. S. Speck, C. G. Levi, F. F. Lange, S. Anderson, *J Mater Res* **1996**, *11*, 2376.

[128] N. Y. Park, G. Cho, S. Bin Kim, Y. K. Sun, *Adv Energy Mater* **2023**, *13*, 2204291.

[129] D. Wang, C. Xin, M. Zhang, J. Bai, J. Zheng, R. Kou, J. Y. Peter Ko, A. Huq, G. Zhong, C. J. Sun, Y. Yang, Z. Chen, Y. Xiao, K. Amine, F. Pan, F. Wang, *Chemistry of Materials* **2019**, *31*, 2731.

[130] U. H. Kim, G. T. Park, B. K. Son, G. W. Nam, J. Liu, L. Y. Kuo, P. Kaghazchi, C. S. Yoon, Y. K. Sun, *Nature Energy 2020 5:11* **2020**, *5*, 860.

[131] Z. Zhong, L. Chen, C. Zhu, W. Ren, L. Kong, Y. Wan, *J Power Sources* **2020**, *464*, 228235.

[132] S. Vadivel, N. Phattharasupakun, J. Wutthiprom, S. Duangdangchote, M. Sawangphruk, *ACS Appl Mater Interfaces* **2019**, *11*, 30719.

Appendix

Copyright permissions

| Instructor Name | Chenxi Geng | Expected Presentation Date | 2023-12-30 |

ADDITIONAL DETAILS

| The Requesting Person / Organization to Appear on the License | Chenxi Geng | | |

REQUESTED CONTENT DETAILS

Title, Description or Numeric Reference of the Portion(s)	Figure 5	Title of the Article / Chapter the Portion Is From	XAFS spectroscopy; fundamental principles and data analysis
Editor of Portion(s)	D.C., Koningsberger; B.L., Mojet; G.E., van Dorssen; D.E., Ramaker	Author of Portion(s)	D.C., Koningsberger; B.L., Mojet; G.E., van Dorssen; D.E., Ramaker
Volume / Edition	10	Publication Date of Portion	2000-05-01
Page or Page Range of Portion	143-155		

Springer Nature BV Terms and Conditions

Total Items: 1

Subtotal: 0.00 CAD

Order Total: 0.00 CAD

Order Confirmation

This is not an invoice. Please go to manage account to access your order history and invoices.

CUSTOMER INFORMATION

Payment by invoice: You can cancel your order until the invoice is generated by contacting customer service.

📑 Billing Address

Chenxi Geng
6310 Coburg Rd
Halifax, NS B3H 4J5
Canada

+1 (782) 234-5896
chenxiulm@gmail.com

📍 Customer Location

Chenxi Geng
6310 Coburg Rd
Halifax, NS B3H 4J5
Canada

📑 PO Number (optional)

N/A

💳 Payment options

Invoice

PENDING ORDER CONFIRMATION

Confirmation Number: Pending

Order Date: 17-Jan-2024

1. Journal of materials chemistry. A, Materials for energy and sustainability

0.00 CAD

Article: Suppressing Detrimental Phase Transitions via Tungsten Doping of LiNiO2 Cathode for Next-Generation Lithium-Ion Batteries

Order License ID	Pending	Publisher	Royal Society of Chemistry
ISSN	2050-7488		
Type of Use	Republish in a thesis/dissertation	Portion	Chart/graph/table/figure

LICENSED CONTENT

Publication Title	Journal of materials chemistry. A, Materials for energy and sustainability	Rightsholder	Royal Society of Chemistry
		Publication Type	Journal
Article Title	Suppressing Detrimental Phase Transitions via Tungsten Doping of LiNiO2 Cathode for Next-Generation Lithium-Ion Batteries	Start Page	18580
		End Page	18588
		Issue	31
		Volume	7
Author/Editor	Royal Society of Chemistry (Great Britain)		

164

Date	01/01/2012		
Language	English		
Country	United Kingdom of Great Britain and Northern Ireland		

REQUEST DETAILS

Portion Type	Chart/graph/table/figure	Distribution	Worldwide
Number of Charts / Graphs / Tables / Figures Requested	1	Translation	Original language of publication
Format (select all that apply)	Print, Electronic	Copies for the Disabled?	No
Who Will Republish the Content?	Not-for-profit entity	Minor Editing Privileges?	No
		Incidental Promotional Use?	No
Duration of Use	Life of current edition	Currency	CAD
Lifetime Unit Quantity	Up to 750,000		
Rights Requested	Main product		

NEW WORK DETAILS

Title	Study of High-Ni Positive Electrode Materials for Li-ion Batteries	Institution Name	Dalhousie University
		Expected Presentation Date	2025-02-18
Instructor Name	Chenxi Geng		

ADDITIONAL DETAILS

Order Reference Number	N/A	The Requesting Person / Organization to Appear on the License	Chenxi Geng

REQUESTED CONTENT DETAILS

Title, Description or Numeric Reference of the Portion(s)	Figure 3	Title of the Article / Chapter the Portion Is From	Suppressing Detrimental Phase Transitions via Tungsten Doping of LiNiO2 Cathode for Next-Generation Lithium-Ion Batteries
Editor of Portion(s)	Ryu, Hoon-Hee; Park, Geon-Tae; Yoon, Chong Seung; Sun, Yang-Kook		
Volume / Edition	7	Author of Portion(s)	Ryu, Hoon-Hee; Park, Geon-Tae; Yoon, Chong Seung; Sun, Yang-Kook
Page or Page Range of Portion	18580-18588		
		Issue, if Republishing an Article From a Serial	31
		Publication Date of Portion	2019-01-01

Total Items: 1

Total Due: 0.00 CAD

Would you like a high resolution image with your order?	no
Will you be translating?	no
Circulation/distribution	50000 or greater
Author of this Springer Nature content	no
Title of new work	Study of High Nickel Cathode Materials for Lithium-ion Batteries
Institution name	Dalhousie University
Expected presentation date	Feb 2025
Portions	Figure 5
Requestor Location	Chenxi Geng 6310 Coburg Rd Halifax, NS B3H 4J5 Canada Attn: Chenxi Geng
Total	0.00 USD

This Agreement between Chenxi Geng ("You") and Elsevier ("Elsevier") consists of your license details and the terms and conditions provided by Elsevier and Copyright Clearance Center.

License Number	5713471251711
License date	Jan 21, 2024
Licensed Content Publisher	Elsevier
Licensed Content Publication	Journal of Power Sources
Licensed Content Title	Comparison of the structural and electrochemical properties of layered Li[Ni x Co y Mn z]O2 (x = 1/3, 0.5, 0.6, 0.7, 0.8 and 0.85) cathode material for lithium-ion batteries
Licensed Content Author	Hyung-Joo Noh,Sungjune Youn,Chong Seung Yoon,Yang-Kook Sun
Licensed Content Date	Jul 1, 2013
Licensed Content Volume	233
Licensed Content Issue	n/a
Licensed Content Pages	10
Start Page	121

End Page	130
Type of Use	reuse in a thesis/dissertation
Portion	figures/tables/illustrations
Number of figures/tables/illustrations	1
Format	both print and electronic
Are you the author of this Elsevier article?	No
Will you be translating?	No
Title of new work	Study of High-Nickel Positive Electrode Materials for Lithium-ion Batteries
Institution name	Dalhousie University
Expected presentation date	Feb 2025
Portions	Figure 11
Requestor Location	Chenxi Geng 6310 Coburg Rd Halifax, NS B3H 4J5 Canada Attn: Chenxi Geng
Publisher Tax ID	GB 494 6272 12
Total	0.00 USD

ELSEVIER LICENSE
TERMS AND CONDITIONS

Jan 21, 2024

This Agreement between Chenxi Geng ("You") and Elsevier ("Elsevier") consists of your license details and the terms and conditions provided by Elsevier and Copyright Clearance Center.

License Number	5713490827329
License date	Jan 21, 2024
Licensed Content Publisher	Elsevier
Licensed Content Publication	Electrochimica Acta
Licensed Content Title	Methods to obtain excellent capacity retention in LiCoO2 cycled to 4.5 V
Licensed Content Author	Zhaohui Chen,J.R. Dahn
Licensed Content Date	Mar 15, 2004
Licensed Content Volume	49
Licensed Content Issue	7
Licensed Content Pages	12
Start Page	1079
End Page	1090

Type of Use	reuse in a thesis/dissertation
Portion	figures/tables/illustrations
Number of figures/tables/illustrations	1
Format	both print and electronic
Are you the author of this Elsevier article?	No
Will you be translating?	No
Title of new work	Study of High-Nickel Positive Electrode Materials for Lithium-ion Batteries
Institution name	Dalhousie University
Expected presentation date	Feb 2025
Portions	Figure 9
Requestor Location	Chenxi Geng 6310 Coburg Rd Halifax, NS B3H 4J5 Canada Attn: Chenxi Geng
Publisher Tax ID	GB 494 6272 12
Total	0.00 USD

Requestor type	University/Academic
Format	Print and electronic
Portion	Figure/table
Number of figures/tables	1
Will you be translating?	No
Title of new work	Study of High-Nickel Positive Electrode Materials for Lithium-ion Batteries
Institution name	Dalhousie University
Expected presentation date	Feb 2025
Portions	Figure 6
Requestor Location	Chenxi Geng 6310 Coburg Rd Halifax, NS B3H 4J5 Canada Attn: Chenxi Geng
Publisher Tax ID	EU826007151
Total	0.00 USD

JOHN WILEY AND SONS LICENSE
TERMS AND CONDITIONS

Apr 11, 2024

This Agreement between Chenxi Geng ("You") and John Wiley and Sons ("John Wiley
and Sons") consists of your license details and the terms and conditions provided by John
Wiley and Sons and Copyright Clearance Center.

License Number	5766020840327
License date	Apr 11, 2024
Licensed Content Publisher	John Wiley and Sons
Licensed Content Publication	Advanced Energy Materials
Licensed Content Title	Mechanism of Action of the Tungsten Dopant in LiNiO2 Positive Electrode Materials
Licensed Content Author	J. R. Dahn, Chongyin Yang, Toby Bond, et al
Licensed Content Date	Dec 31, 2021
Licensed Content Volume	12
Licensed Content Issue	6
Licensed Content Pages	8
Type of use	Dissertation/Thesis
Requestor type	Author of this Wiley article

Format	Print and electronic
Portion	Full article
Will you be translating?	No
Title of new work	Study of High-Nickel Positive Electrode Materials for Lithium-ion Batteries
Institution name	Dalhousie University
Expected presentation date	Feb 2025
Requestor Location	Chenxi Geng 6310 Coburg Rd Halifax, NS B3H 4J5 Canada Attn: Chenxi Geng
Publisher Tax ID	EU826007151
Total	0.00 USD

Terms and Conditions

Impact of Aluminum Added to Ni-Based Positive Electrode Materials by Dry Particle Fusion

ACS Publications
Most Trusted. Most Cited. Most Read.

Author: Chenxi Geng, Aaron Liu, Jeff R. Dahn

Publication: Chemistry of Materials

Publisher: American Chemical Society

Date: Jul 1, 2020

Copyright © 2020, American Chemical Society

PERMISSION/LICENSE IS GRANTED FOR YOUR ORDER AT NO CHARGE

This type of permission/license, instead of the standard Terms and Conditions, is sent to you because no fee is being charged for your order. Please note the following:

BACK

CLOSE WINDOW

ACSPublications
Most Trusted. Most Cited. Most Read.

The Li-Ion Rechargeable Battery: A Perspective

Author: John B. Goodenough, Kyu-Sung Park

Publication: Journal of the American Chemical Society

Publisher: American Chemical Society

Date: Jan 1, 2013

Copyright © 2013, American Chemical Society

PERMISSION/LICENSE IS GRANTED FOR YOUR ORDER AT NO CHARGE

This type of permission/license, instead of the standard Terms and Conditions, is sent to you because no fee is being charged for your order. Please note the following:

- Permission is granted for your request in both print and electronic formats, and translations.
- If figures and/or tables were requested, they may be adapted or used in part.
- Please print this page for your records and send a copy of it to your publisher/graduate school.
- Appropriate credit for the requested material should be given as follows: "Reprinted (adapted) with permission from {COMPLETE REFERENCE CITATION}. Copyright {YEAR} American Chemical Society." Insert appropriate information in place of the capitalized words.
- One-time permission is granted only for the use specified in your RightsLink request. No additional uses are granted (such as derivative works or other editions). For any uses, please submit a new request.

If credit is given to another source for the material you requested from RightsLink, permission must be obtained from that source.

BACK

CLOSE WINDOW

ACSPublications
Most Trusted. Most Cited. Most Read.

An Unavoidable Challenge for Ni-Rich Positive Electrode Materials for Lithium-Ion Batteries

Author: Hongyang Li, Aaron Liu, Ning Zhang, et al

Publication: Chemistry of Materials

Publisher: American Chemical Society

Date: Sep 1, 2019

Copyright © 2019, American Chemical Society

PERMISSION/LICENSE IS GRANTED FOR YOUR ORDER AT NO CHARGE

This type of permission/license, instead of the standard Terms and Conditions, is sent to you because no fee is being charged for your order. Please note the following:

- Permission is granted for your request in both print and electronic formats, and translations.
- If figures and/or tables were requested, they may be adapted or used in part.
- Please print this page for your records and send a copy of it to your publisher/graduate school.
- Appropriate credit for the requested material should be given as follows: "Reprinted (adapted) with permission from {COMPLETE REFERENCE CITATION}. Copyright {YEAR} American Chemical Society." Insert appropriate information in place of the capitalized words.
- One-time permission is granted only for the use specified in your RightsLink request. No additional uses are granted (such as derivative works or other editions). For any uses, please submit a new request.

If credit is given to another source for the material you requested from RightsLink, permission must be obtained from that source.

BACK

CLOSE WINDOW